2016

Transient CFD analysis of autorotation using hybrid LES and adaptive mesh morphing techniques

Patricia Coronado Domenge
University of Central Florida

TRANSIENT CFD ANALYSIS OF AUTOROTATION
USING HYBRID LES AND ADAPTIVE MESH MORPHING TECHNIQUES

by

PATRICIA XIMENA CORONADO DOMENGE
B.S. Aerospace Engineering, University of Miami, 2007
B.S. Mechanical Engineering, University of Miami, 2007
M.S. Mechanical Engineering, University of Miami, 2009

A dissertation submitted in partial fulfilment of the requirements
for the degree of Doctor of Philosophy
in the Department of Mechanical and Aerospace Engineering
in the College of Engineering and Computer Science
at the University of Central Florida
Orlando, Florida

Spring Term
2016

Major Professor: Tuhin Das

ABSTRACT

Large-Eddy Simulation (LES) based turbulence modeling is a developing area of research in Fluid-Structure Interaction (FSI). There is considerable scope for further scientific research in this field and this dissertation aims to extend it to the study of flow-induced motion. The emphasis of this work is on autorotation, an important category of flow-induced motion that is commonly seen in energy applications such as wind turbines and in aviation applications such as the autogyro. In contrast to existing works on FSI that typically assume prescribed motion of structures in a flow field, this research develops LES based FSI studies for large-scale flow-induced motions as seen in autorotation. The uniqueness of the formulation and modeling approach lies in the development of a numerically stable computational scheme that incorporates a moving and morphing mesh structure. The method is first demonstrated for the autorotation of a square flat plate and then extended to a rotor structure similar to that of a helicopter.

In order to simulate an autorotating square flat plate, a coupled Computational Fluid Dynamics (CFD) - Rigid Body Dynamics (RBD) model is proposed, employing the delayed-detached-eddy simulation (DDES) and the Smagorinsky turbulence models to resolve subgrid-scale stresses (SGS). The plate is allowed to spin freely about its center of mass. Computational results are compared to experimental measurements and Reynolds Average Navier-Stokes (RANS) simulations found in the literature. When compared to RANS, the results from the LES models provide better predictions of the pressure coefficient. Moreover, LES accurately captures the transient behavior of the plate, and close correspondence is found between the predicted and measured moment coefficients. The qualitative prediction of vortex structures and the quantitative computation of pressure coefficients are in good agreement with experimental results. Hybrid models, such as improved Delayed-Detached-Eddy Simulation (iDDES), are shown to provide very similar results to those of pure LES. Therefore hybrid models are found to be a good alternative to use for the simulation of FSI in autorotation, saving valuable computational time . The iDDES method combines both

RANS and LES, dividing the flow domain into LES far away from a solid wall and RANS near a solid wall, overcoming the computational costs of pure LES.

Encouraging results from this effort prompted the extension to a realistic scenario, namely the autorotation of a flapping-blade rotor in a prevailing wind field. A coupled CFD - Multi Body Dynamics (MBD) model is developed to study the complex FSI of an autorotating 3-blade rotor, similar to that of a helicopter, employing the iDDES turbulence model. In addition to the rotor being allowed to spin freely about its axis, each of the individual blades is free to rotate about hinges at the root. This adds degrees of freedom to the kinematics of the rotor and necessitates localized mesh morphing around the blades to capture the FSI with accuracy. The model is validated against experimental data and shows excellent agreement. The experimental apparatus consists of a flapping blade rotor and a fixture used to mount it at different angles of incidence with respect to the wind field. The rotor is instrumented with a DC motor that is operated in generator mode. The setup is dual-purpose, providing speed measurement using the motor's back-emf and regenerative braking by varying the current draw. Overall, the presented research can help obtain accurate values of aerodynamic parameters at a high spatial resolution that would be otherwise difficult to acquire in experiments. Ultimately this approach can be a cost effective means of aerodynamic modeling in applications involving large scale FSI.

To Aida

ACKNOWLEDGMENTS

The completion of this research would not have been possible without the help and support of my family, friends, and colleagues, and thus I would like to offer them my deepest gratitude.

First, I would like to thank Professor Tuhin K. Das, my advisor during the second half of my Ph.D. study, for his guidance and support throughout my study at the University of Central Florida.

I would like to thank the professors in my dissertation committee for their examination of my Ph.D research.

The Department of Mechanical and Aerospace Engineering is acknowledged for providing financial support through graduate teaching and research assistantships.

Special thanks go to tuma, tupa, Maygen, OFGenie, and M&M. All provided invaluable support and guidance throughout this six year journey, which helped me stay motivated during both successful and unsuccessful times.

TABLE OF CONTENTS

LIST OF FIGURES

x

CHAPTER 1: INTRODUCTION

The term autorotation was first introduced by Riabouchinsky in 1935, [54], and was later defined, [61], as the continued rotation of an object lacking an external power source due to a stream of air. Accurate prediction of the fluid and rigid body dynamics of autorotation is known to be very challenging because of the complex unsteady flow dynamics, often involving fluid-structure interaction (FSI), turbulent flow and flow separation, and most importantly the strong coupling of the two-way interaction between the fluid and solid. As a result, accurate unsteady and non-dissipative turbulence modelling is critical when resolving the aerodynamic non-linearity of autorotation. Many industrial applications, such as wing flutter and bridge oscillations, experience strong FSI effects, which can cause catastrophic failure, especially when materials susceptible to fatigue are involved, [3]. Further research is required to develop current state of the art FSI methods, in specific the turbulent and rigid body motion interaction, before optimization, coupled with Computational Fluid Dynamics (CFD), can be used in the design of successive industrial applications. Most specifically, in applications that require large scale FSI such as wind turbines and rotorcraft.

1.1   Background

The uninterrupted rotation of a solid body without the use of external power is defined as autorotation, [61]. Autorotation of a rotor at high inclination angles with respect to the free stream flow is generated by the complex FSI between the free stream velocity and the solid blades, often involving turbulent flow and flow separation. Therefore accurate prediction of the fluid and rigid body dynamics of autorotation is very challenging given the difficulty in modelling the strong coupling of the two-way interaction between the fluid and solid. The angular rate of autorotation is then dependent on the polar moment of inertia of the rotor blade system, the Reynolds number of

the free stream air, the drag of the blade sections, and the inclination of the rotor disk with respect to the air flow direction. In contrast to the way a helicopter generates vertical thrust by accelerating air in a downward direction, in autorotation the blades autorotate due to the resulting torque from the aerodynamic forces resulting from placing the rotor inclined to a wind field, [71], as seen in Fig. 1.1(a). In addition, the aerodynamic forces create a thrust force which can be significant based on the incidence angle and the wind speed.

(a) Side view   (b) Disk of rotation plane view
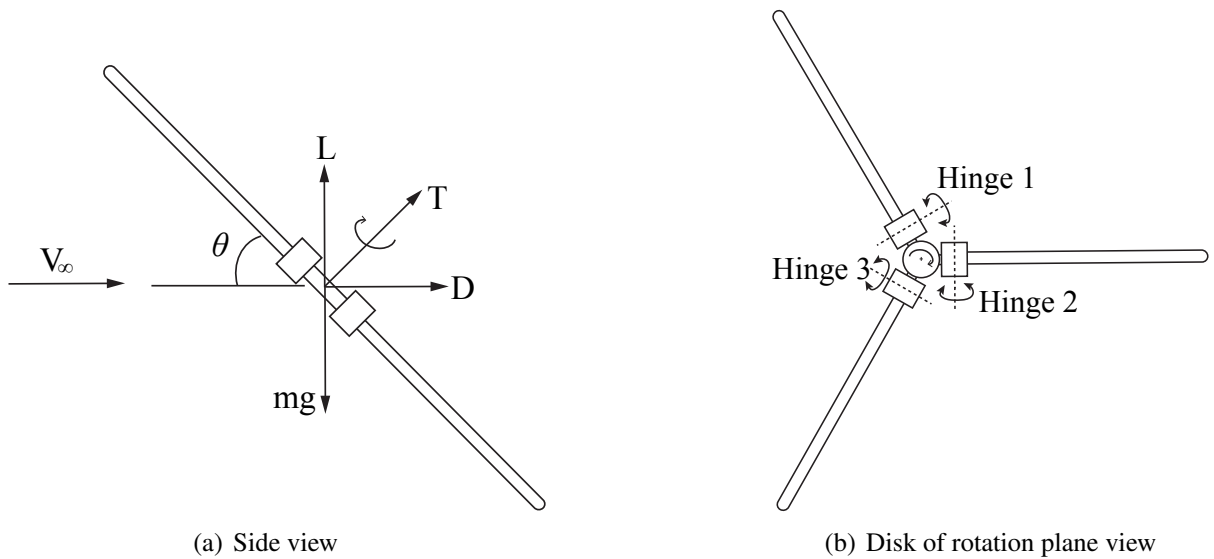
Figure 1.1: Schematic diagram of autogyro as seen from the (a) side view and (b) the disk of rotation plane view

The theory of autorotation can be traced back to 1926 to a study on the autogyro by Glauert, [23]. An autogyro is a multi-blade rotor type aircraft, in addition to the blades being free to spin about their common axis, each individual blade is free to rotate about a hinge at its root independently from the others, as seen in Fig. 1.1(b). The first static analytical autorotation models [22, 23, 45, 79] use a blade element momentum approach to model the aerodynamic forces. The limitation of these models is that they are static models and, therefore, lack predictive accuracy in transient simulations. To resolve this, and improve the predictive accuracy, the development of high fidelity computational models is needed. Previous work on autorotation has been done in the study of free falling objects [35, 50], wings [61], and most recently in tree seeds [38, 40, 71], and

2

flat plates [1, 11, 27, 34]. Figure 1.2 provides a schematic diagram of a blade under autorotation, [39]. The figure shows two regions of the blade where accelerating and decelerating torques are generated due to its interaction with the wind field. The accelerating torque is generated in the region where the driving force is larger than the effect of drag. Similarly, the decelerating torque is generated in the region where the opposite is true. The former is generated in the inner portions of the blade, while the latter is generated in the outer portion of the blade. This is shown through the force diagrams given in Fig. 1.2.
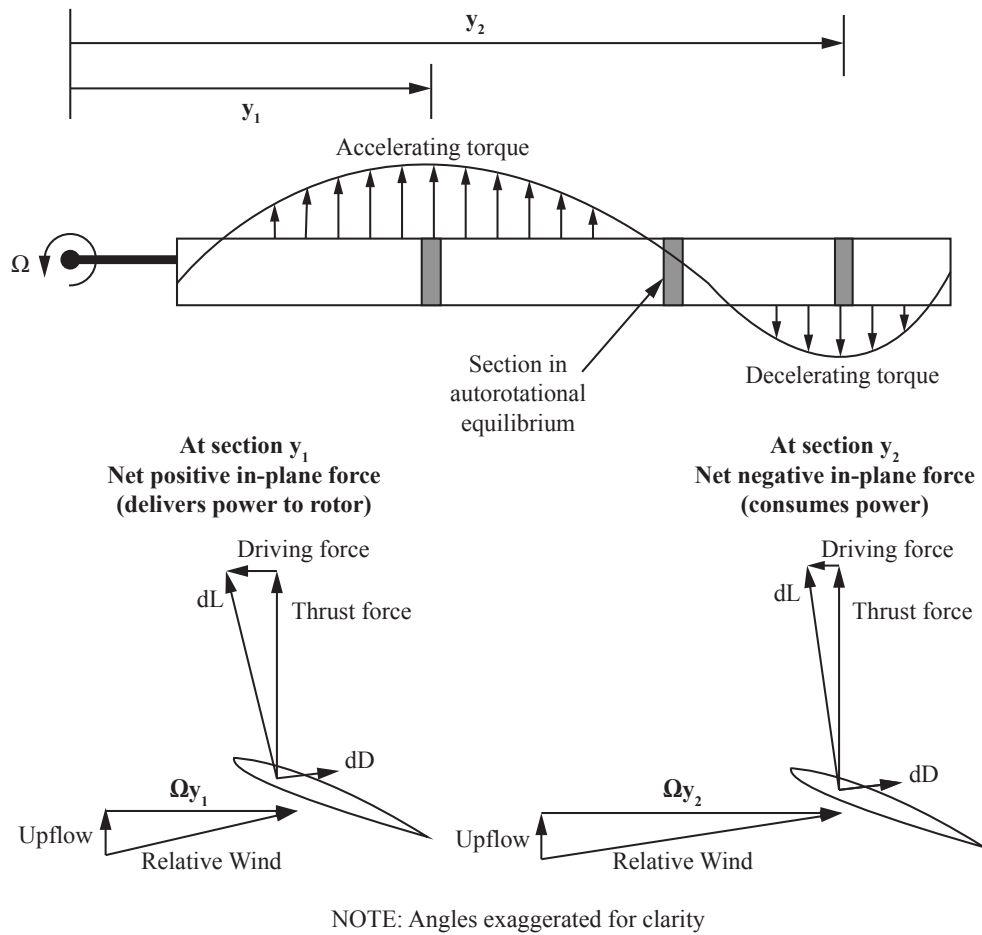
Figure 1.2: Forces acting on the blades, conditions for autorotation, [39]

The goal of this dissertation is to build a high resolution computational model of autorotation to capture the FSI interaction and aerodynamic forces with good accuracy. At present, Reynolds average Navier-Stokes (RANS) equations based models are widely used for low run times when simulating turbulence, although they lack precision in accurately predicting flow separation given its time averaging of fluctuations and modeling of the Reynolds stress tensor. As a result, RANS models make it hard to preserve the vortex characteristics involved leaving a flow field void of incoherent structures. In contrast, large-eddy simulation (LES) models have proven to be a good alternative to RANS models as they preserve the characteristics of the vortex as shown by Eisenback and Friedrich, [16], and most recently the Smagorinsky model with Van Driest damping has been implemented by Im et al., [30], achieving good agreement with experimental observations. Given their success and advantages over RANS, LES and hybrid LES are implemented as the turbulence models for the computational models introduced in this dissertation.

Recently, LES has been successfully implemented in the study of turbo-machinery as published by Li et al., [42], Tyacke et al. [70], and Watson et al,. [77]. LES has also been successful when used in particle tracking [14], compressible flow [46], combustion [32, 43, 72] and now in autorotation [11]. However, as shown by Breuer et al., [8], and Feymark, [20], there is still the need for further LES investigation in the area of FSI, especially in autorotation without a prescribed set rotation. A great deal of the work in FSI is conducted using hybrid models, combining both RANS and LES methods, as presented by Wang [76], Wang et al. [75], and Shinde et al. [58]. The work on this dissertation aims to provide new contributions to LES in the developing field of autorotation, a subfield of FSI.

LES models are not only promising, but also they perform better than RANS models, and overcome several of the RANS model disadvantages. In LES, the governing equations are spatially filtered on the scale of the numerical grid. The large energy containing scales are resolved numerically, and the small scale eddies, which are generally more homogeneous and universal, are modeled. The large eddies are strongly affected by the flow field geometry boundaries,

4

therefore the direct computation of the large eddies by LES is more accurate than modeling the large eddies by RANS. This in turn helps to better simulate flow separation, an important factor in autorotation. Separated vortices create large pressure gradients on the surface of origin, which is the driving force of this autorotation, i.e., in laminar flow the autorotation is not sustained. The effect of the unresolved small scales of motion in LES is typically modeled by a subgrid-scale (SGS) model[13, 21, 44, 52, 60] or by the inherent dissipation in the numerical schemes[4, 5, 6, 25, 37, 57]. Because the statistics of the small scale turbulence are more isotropic and universal, a general physical model for small scale eddies is more plausible.

For certain applications and complex flows that require solving for the wall boundary layer, the CPU resource needed by LES is close to that of the Direct Numerical Simulation (DNS). As a result, pure LES might not be rigorously implemented for another 3 decades in engineering applications, [65], and several hybrid RANS and LES models have been developed to overcome the intensive CPU requirements for LES, with runtimes between those of RANS and LES. One of these models was introduced by Spalart et al. in 1997 called detached-eddy simulation (DES), [65], which divides a flow domain into a LES region far away from a solid wall and a RANS region near a solid wall. Previous work for turbulence simulations for airfoils, cylinders and forbodies using DES have shown encouraging results as seen in work done by Travin et al. [69], Spalart [62], Hansen and Forsythe [26], Viswanathan et al. [73], and Subbareddy and Candler [66].

The original DES model suffers from the downside that the transition from RANS to LES may not be grid independent and as a result Spalart suggested a modification to his original model in 2006, [64], called delayed-detached-eddy simulation (DDES). In order for the transition to be independent from grid spacing, Spalart used a blending function to limit the DES length scale similar to the one used by Menter and Kuntz, [49], for the Shear Stress Transport (SST) model. The DDES model has shown excellent agreement with experimental data as well as a significant improvement from DES in work done by Wang and Zha [74], Coronado Domenge et al. [12] and Im et al. [30].

5

For turbulence modeling, additional adjustments for the DDES model, improved DDES (iD-DES), are then outlined by Travin et al., [68], concerning the definition of the LES length scale and the Wall-Modelled Large-Eddy Simulation (WMLES) helping to resolve the turbulence definition near solid walls. For a more comprehensive review of the LES and hybrid models mentioned in this dissertation the reader is directed to the review paper by Argyropoulos and Markatos, [2].

For FSI simulations, a good turbulence model is not enough, as the governing equations of the fluid flow and the structure have to be solved simultaneously, given that in nature this interaction occurs at the same time. Therefore, a good coupled CFD - rigid body dynamics (RBD) model is needed to capture the interaction between the fluid and the body without any time lag. Previous work has been done using loosely coupled models where there is a time difference between the information exchanged from the flow to the structural solver and vice versa [9, 24, 36]. This lag is due to the need for a convergence on the individual solvers before the exchange of information. More recently, fully coupled models, in which the governing equations for the flow and the structure are solved together, have been developed to study engine fans and compressors [29] and autorotating plates [11, 27].

A fully coupled FSI simulation requires the solver to calculate the forces in the fluid and then applying them to the solid structure, computing the movement and deformation of the body. In other words, the fluid forces affect the solid body which in turn deforms and affect the fluid flow in the next time step. Therefore, an important requirement for the simulation of FSI is mesh deformation, as the computational mesh is regenerated every time step to match the motion of the structure. As a result, it is crucial that the coupled CFD model involves an adaptive mesh morphing technique that does not cause any numerical problems due to poor mesh quality deformations. Autorotation involves large rotations and therefore introduces large displacements which can bring about significant convergence and stability problems. In order to overcome large deformations of the grid cells of the mesh, an advance mesh deforming technique that allows the mesh cells to break up and slide, instead of morphing, is used in this research.

In this dissertation, the flow around an autorotating flat plate is simulated, using several LES models, which was analyzed experimentally by Martinez-Vazquez et al., [47], and previously simulated using RANS models by Hargreaves et al., [27]. A coupled CFD - multi body dynamics (MBD) model is then introduced to study the flow around an autorotating 3-blade rotor and validated against experimental data.

1.2   Objectives

The objective of this research is to develop a high fidelity fully coupled CFD-MBD model for the study of large scale FSI and to investigate the flow of the autorotation of a 3-blade rotor. In order to achieve this objective, the following tasks are accomplished in this work:

1. Development of a fully coupled single body CFD model using LES and LES/RANS hybrid turbulence to study the autorotation of a square flat plate

2. Validation of the CFD - RBD model against experimental results and RANS simulations found in literature of an autorotating plate

3. Development of a fully coupled multi-body CFD model using LES/RANS hybrid turbulence to study the autorotation of a 3-blade rotor

4. Implementation of an experimental setup for an autogyro experiment to produce results to use for the validation of the CFD - MBD model

5. Validation of the CFD - MBD model against experimental results generated by the autogyro experiment

1.3 Outline of the Dissertation

This Chapter provided an introduction, literature review and the objectives of the work discussed in this dissertation. Chapter 2 presents the fluid flow governing equations that are solved with the use of CFD and turbulence model applications. The equations describing the rigid body motion responsible for the motion of the mesh are then described in Chapter 3 for both a single and multi-body model. Chapter 4 describes the simulations performed and presents a comparison of results with experimental data to validate the high fidelity FSI models introduced. Further results are then discussed in Chapter 5 for the autorotating square flat plate and the autorotating 3-blade rotor studied in this work. Finally, Chapter 6 presents a summary of the findings as well as the completed objectives, future research work and a list of publications.

CHAPTER 2: FLUID FLOW GOVERNING EQUATIONS

The fluid flow governing equations are the basic conservation equations of mass, momentum, and energy from which the 3D general Navier-Stokes equations are derived. These equations are derived using a Eulerian type control volume approach.

2.1   Conservation of Mass

The conservation of mass equations in differential form is given by:

$$\frac{\partial \rho}{\partial t} + \nabla \cdot (\rho \mathbf{V}) = 0 \tag{2.1}$$

where ρ is the fluid density, t is the time, and $\mathbf{V}$ is the flow velocity vector:

$$\mathbf{V} = u\mathbf{i} + v\mathbf{j} + w\mathbf{k} \tag{2.2}$$

For incompressible or steady flow, Equation 2.1 is reduced to $\nabla \cdot \rho \mathbf{V} = \mathbf{0}$.

2.2   Momentum Equation

The momentum equation is derived from Newton's second law and is defined in differential form as:

$$\rho \frac{D\mathbf{V}}{Dt} = \rho \mathbf{f} + \nabla \cdot \sigma \tag{2.3}$$

where $\mathbf{f}$ is the body force and σ is the stress tensor defined by:

$$\sigma = -p\delta_{ij} + \tau_{ij} = -p\delta_{ij} + \mu \left[\frac{\partial u_i}{\partial x_j} + \frac{\partial u_j}{\partial x_i} - \frac{2}{3} \frac{\partial u_k}{\partial x_k} \delta_{ij} \right] \tag{2.4}$$

here p is the static pressure, δ_{ij} is the Kronecker's delta function:

$$\delta_{ij} = \begin{cases} 1 & \text{when } i = j \\ 0 & \text{when } i \neq j \end{cases}$$

and μ is the molecular viscosity modeled by Sutherland's law:

$$\frac{\mu}{\mu_\infty} = \left(\frac{T}{T_\infty} \right)^{1.5} \frac{T + 110K}{T + T_\infty} \tag{2.5}$$

where T is the static temperature and μ_∞ and T_∞ are conditions at a reference point.

2.3   Energy Equation

The energy equation is derived from the 1st law of thermodynamics and is defined in differential form by:

$$\frac{D\rho e}{Dt} = -\nabla \cdot \mathbf{q} + \rho \mathbf{f} \cdot \mathbf{V} + \nabla \cdot (\sigma \cdot \mathbf{V}) \tag{2.6}$$

where e is the total energy per unit mass:

$$e = c_v T + \frac{1}{2} \left(u^2 + v^2 + w^2 \right) \tag{2.7}$$

where c_v is the constant volume specific heat coefficient and $\mathbf{q}$ is the conductive hear flux vector:

$$\mathbf{q} = q_x\mathbf{i} + q_y\mathbf{j} + q_z\mathbf{k} \tag{2.8}$$

and by Fourier's law:

$$\mathbf{q} = -k\nabla T \tag{2.9}$$

where k is the thermal conductivity.

Substituting the definition of a substantial derivative,

$$\frac{D}{Dt} = \frac{\partial}{\partial t} + \mu_k \frac{\partial}{\partial x_k} \tag{2.10}$$

into Equations 2.3 and 2.6, the fluid flow governing equations, following the Einstein convention, can be rewritten as follows:

$$\frac{\partial \rho}{\partial t} + \frac{\partial \rho u_k}{\partial x_k} = 0 \tag{2.11}$$

$$\frac{\partial \rho u_i}{\partial t} + \frac{\partial \rho u_i u_k}{\partial x_k} = -\frac{\partial p}{\partial x_i} + \frac{\partial \tau_{ik}}{\partial x_k} \tag{2.12}$$

$$\frac{\partial \rho e}{\partial t} + \frac{\partial (\rho e + p) u_k}{\partial x_k} = \frac{\partial (\tau_{ik} u_i + q_k)}{\partial x_k} \tag{2.13}$$

11

where ρe is defined as:

$$\rho e = \frac{p}{\gamma - 1} + \frac{1}{2}\rho \left(u^2 + v^2 + w^2 \right) \tag{2.14}$$

In order to solve Equations 2.11, 2.12 and 2.13, they need to be supplemented with the equation of state for an ideal gas:

$$p = \rho R T \tag{2.15}$$

where R is the gas constant and γ is the specific heat ratio of the fluid.

2.4   Spatially Filtered 3D Navier-Stokes Equations

Equations 2.11 - 2.14 are the Navier-Stokes (NS) equations and for turbulent flows can be solved using direct numerical simulation (DNS). However, such solution is limited to very simple geometries and low Reynolds numbers as DNS requires the grid size to be on the same order of magnitude as the spatial and temporal length scales. In order to resolve all the scales of turbulence the time steps size needs to be close to $Re^{3/4}$ and the number of grid points equal to $Re^{9/4}$ [51]. Calculations of this magnitude become unfeasible and computationally too expensive, therefore the Navie-Stokes equations are reformulated using a spatial averaging approach, and the turbulent effects are resolved using turbulence models. By using spatial filtering, the small scale high frequency components of the motion of the fluid are eliminated perserving the large scale tubulent motion[17].

The governing equations for the flow field computation in a rotating frame are the second order nonlinear partial differential spatially filtered 3D general Navier-Stokes equations in generalized

12

coordinates and can be written as follows:

$$\frac{\partial \mathbf{Q}'}{\partial t} + \frac{\partial \mathbf{E}'}{\partial \xi} + \frac{\partial \mathbf{F}'}{\partial \eta} + \frac{\partial \mathbf{G}'}{\partial \zeta} = \frac{1}{\mathrm{Re}} \left(\frac{\partial \mathbf{E}'_{\mathbf{v}}}{\partial \xi} + \frac{\partial \mathbf{F}'_{\mathbf{v}}}{\partial \eta} + \frac{\partial \mathbf{G}'_{\mathbf{v}}}{\partial \zeta} \right) + \mathbf{S}'_{\mathbf{R}} \qquad (2.16)$$

where Re is the Reynolds number defined as:

$$Re = \frac{\rho_\infty u_\infty L}{\mu_\infty} \qquad (2.17)$$

where ρ_∞ is the reference density, u_∞ is the reference velocity, L is the reference length, and μ_∞ is the reference viscosity.

From Equation 2.16, the generalized variable vector $\mathbf{Q}'$, the generalized inviscid flux vectors $\mathbf{E}'$, $\mathbf{F}'$, and $\mathbf{G}'$, the generalized viscous fluxes $\mathbf{E}'_{\mathbf{v}}$, $\mathbf{F}'_{\mathbf{v}}$, and $\mathbf{G}'_{\mathbf{v}}$, and the generalized rotation source term $\mathbf{S}'_{\mathbf{R}}$ are given by:

$$\mathbf{Q}' = \frac{\mathbf{Q}}{J} \qquad (2.18)$$

$$\mathbf{E}' = \frac{1}{J}(\xi_t \mathbf{Q} + \xi_x \mathbf{E} + \xi_y \mathbf{F} + \xi_z \mathbf{G}) \qquad (2.19)$$

$$\mathbf{F}' = \frac{1}{J}(\eta_t \mathbf{Q} + \eta_x \mathbf{E} + \eta_y \mathbf{F} + \eta_z \mathbf{G}) \qquad (2.20)$$

$$\mathbf{G}' = \frac{1}{J}(\zeta_t \mathbf{Q} + \zeta_x \mathbf{E} + \zeta_y \mathbf{F} + \zeta_z \mathbf{G}) \qquad (2.21)$$

13

$$\mathbf{E'_v} = \frac{1}{J}(\xi_x\mathbf{E_v} + \xi_y\mathbf{F_v} + \xi_z\mathbf{G_v}) \tag{2.22}$$

$$\mathbf{F'_v} = \frac{1}{J}(\eta_x\mathbf{E_v} + \eta_y\mathbf{F_v} + \eta_z\mathbf{G_v}) \tag{2.23}$$

$$\mathbf{G'_v} = \frac{1}{J}(\zeta_x\mathbf{E_v} + \zeta_y\mathbf{F_v} + \zeta_z\mathbf{G_v}) \tag{2.24}$$

$$\mathbf{S'_R} = \frac{S_R}{J} \tag{2.25}$$

where J is the transformation Jacobian. This transforms the governing equations from the physical space (x, y, z) to the computational domain (ξ, η, ζ), generating an equally spaced rectangular grid system for numerical accuracy and simpler implementation.

The Navier-Stokes equations noted in Equation 2.16 are normalized by a characteristic length and reference parameters given that for CFD this is useful to bring the numerical round-off error to its minimum, the normalization procedure is found in detail in[28].

The variable vector $\mathbf{Q}$, and inviscid flux vectors $\mathbf{E}$, $\mathbf{F}$, and $\mathbf{G}$ from the above equations are defined as:

$$\mathbf{Q} = \begin{pmatrix} \bar{\rho} \\ \bar{\rho}\tilde{u} \\ \bar{\rho}\tilde{v} \\ \bar{\rho}\tilde{w} \\ \bar{\rho}\tilde{e} \end{pmatrix}, \mathbf{E} = \begin{pmatrix} \bar{\rho}\tilde{u} \\ \bar{\rho}\tilde{u}^2 + \bar{p} \\ \bar{\rho}\tilde{u}\tilde{v} \\ \bar{\rho}\tilde{u}\tilde{w} \\ (\bar{\rho}\tilde{e} + \bar{p})\tilde{u} \end{pmatrix}, \mathbf{F} = \begin{pmatrix} \bar{\rho}\tilde{v} \\ \bar{\rho}\tilde{v}\tilde{u} \\ \bar{\rho}\tilde{v}^2 + \bar{p} \\ \bar{\rho}\tilde{v}\tilde{w} \\ (\bar{\rho}\tilde{e} + \bar{p})\tilde{v} \end{pmatrix}, \mathbf{G} = \begin{pmatrix} \bar{\rho}\tilde{w} \\ \bar{\rho}\tilde{w}\tilde{u} \\ \bar{\rho}\tilde{w}\tilde{v} \\ \bar{\rho}\tilde{w}^2 + \bar{p} \\ (\bar{\rho}\tilde{e} + \bar{p})\tilde{w} \end{pmatrix}$$

where ρ is the density, u, v, w are the Cartesian velocity components in x, y, z directions, p is the static pressure, and e is the total energy per unit mass. The overbar denotes a regular filtered variable, and the tilde is used to denote the Favre filtered variable [18]. For an arbitrary function $u(x_i, t)$, the filtered variable $\bar{u}(x_i, t)$ is given by:

$$\bar{u}(x_i, t) = \int_D G(x_i - \xi_i, \Delta) u(\xi_i, t) d\xi_i \tag{2.26}$$

where G is the filter function and Δ is the filter width associated with the size of the mesh. The Favre filtered variable $\tilde{u}(x_i, t)$ is then defined as:

$$\tilde{u}(x_i, t) = \frac{\overline{\rho u}}{\bar{\rho}} \tag{2.27}$$

where $\bar{\rho}$ is the filtered density.

The viscous flux vectors $\mathbf{E_v}$, $\mathbf{F_v}$, and $\mathbf{G_v}$ are defined by:

$$\mathbf{E_v} = \begin{pmatrix} 0 \\ \bar{\tau}_{xx} + \sigma_{xx} \\ \bar{\tau}_{xy} + \sigma_{xy} \\ \bar{\tau}_{xz} + \sigma_{xz} \\ Q_x \end{pmatrix}, \mathbf{F_v} = \begin{pmatrix} 0 \\ \bar{\tau}_{yx} + \sigma_{yx} \\ \bar{\tau}_{yy} + \sigma_{yy} \\ \bar{\tau}_{yz} + \sigma_{yz} \\ Q_y \end{pmatrix}, \mathbf{G_v} = \begin{pmatrix} 0 \\ \bar{\tau}_{zx} + \sigma_{zx} \\ \bar{\tau}_{zy} + \sigma_{zy} \\ \bar{\tau}_{zz} + \sigma_{zz} \\ Q_z \end{pmatrix}$$

where $\bar{\tau}_{ij}$ is the molecular stress tensor, σ_{ij} is the sub-grid scale stress tensor, and Q_i is the energy flux.

The molecular viscous stress tensor $\bar{\tau}$ is calculated using the following equation:

$$\bar{\tau}_{ij} = \frac{2}{3}\tilde{\mu}\frac{\partial \tilde{u}_k}{\partial x_k}\delta_{ij} + \mu(\frac{\partial \tilde{u}_i}{\partial x_j} + \frac{\partial \tilde{u}_j}{\partial x_i}), \qquad i, j = 1, 2, 3 \tag{2.28}$$

15

where the molecular viscosity $\tilde{\mu} = \tilde{\mu}(\tilde{T})$ is determined by Sutherland law as described by Equation 2.5. Equation 2.28 is in tensor notation and the subscript 1, 2, 3 represent the coordinates, x, y, z using the Einstein summation convention.

The sub-grid scale stress tensor σ due to the filtering process is defined as:

$$\sigma_{ij} = -\bar{\rho}(\widetilde{u_i u_j} - \tilde{u}_i \tilde{u}_j) \tag{2.29}$$

The energy flux Q is expressed as:

$$Q_i = \tilde{u}_j(\bar{\tau}_{ij} + \sigma_{ij}) - \bar{q}_i + \Phi_i \tag{2.30}$$

where Φ is the sub-scale heat flux and $\bar{q}_i$ is the molecular heat flux and are defined as follows:

$$\Phi_i = -C_p\bar{\rho}(\widetilde{u_i T} - \tilde{u}_i \tilde{T}) \tag{2.31}$$

$$\bar{q}_i = -\frac{c_p \tilde{\mu}}{Pr}\frac{\partial \tilde{T}}{\partial x_i} \tag{2.32}$$

where c_p is the constant pressure specific heat coefficient and Pr is the Prandtl number.

And the inviscid fluxes $\mathbf{E}'$, $\mathbf{F}'$, and $\mathbf{G}'$ in generalized coordinate system are expressed as:

$$
\mathbf{E}' = \begin{bmatrix} \bar{\rho}U \\ \bar{\rho}\tilde{u}U + l_x\bar{p} \\ \bar{\rho}\tilde{v}U + l_y\bar{p} \\ \bar{\rho}\tilde{w}U + l_z\bar{p} \\ (\bar{\rho}\tilde{e} + \bar{p})U - l_t\bar{p} \end{bmatrix}, \quad
\mathbf{F}' = \begin{bmatrix} \bar{\rho}V \\ \bar{\rho}\tilde{u}V + m_x\bar{p} \\ \bar{\rho}\tilde{v}V + m_y\bar{p} \\ \bar{\rho}\tilde{w}V + m_z\bar{p} \\ (\bar{\rho}\tilde{e} + \bar{p})V - m_t\bar{p} \end{bmatrix}, \quad
\mathbf{G}' = \begin{bmatrix} \bar{\rho}W \\ \bar{\rho}\tilde{u}W + n_x\bar{p} \\ \bar{\rho}\tilde{v}W + n_y\bar{p} \\ \bar{\rho}\tilde{w}W + n_z\bar{p} \\ (\bar{\rho}\tilde{e} + \bar{p})W - n_t\bar{p} \end{bmatrix}
$$

where U, V and W are the contravariant velocities in ξ, η and ζ directions and are defined by:

$$
\begin{aligned}
U &= l_t + \mathbf{l} \cdot \mathbf{V} = l_t + l_x \tilde{u} + l_y \tilde{v} + l_z \tilde{w} \\
V &= m_t + \mathbf{m} \cdot \mathbf{V} = m_t + m_x \tilde{u} + m_y \tilde{v} + m_z \tilde{w} \\
W &= n_t + \mathbf{n} \cdot \mathbf{V} = n_t + n_x \tilde{u} + n_y \tilde{v} + n_z \tilde{w}
\end{aligned}
\tag{2.33}
$$

where l_t, m_t, and n_t are the grid moving velocities and are defined as follows:

$$
l_t = \frac{\xi_t}{J}, \; m_t = \frac{\eta_t}{J}, \; n_t = \frac{\zeta_t}{J}
\tag{2.34}
$$

and where $\mathbf{l}$, $\mathbf{m}$, $\mathbf{n}$ are the normal vectors on the ξ, η, ζ surfaces with their magnitudes equal to the elemental surface area and pointing in the directions of increasing ξ, η, ζ, defined in generalized parameters as:

$$
\mathbf{l} = \frac{\nabla \xi}{J}, \; \mathbf{m} = \frac{\nabla \eta}{J}, \; \mathbf{n} = \frac{\nabla \zeta}{J}
\tag{2.35}
$$

l_t, m_t, and n_t are equal to zero when the grid is stationary.

The Favre averaged Navier-Stokes equations can then be written as follows:

$$
\frac{\partial \bar{\rho}}{\partial t} + \frac{\partial \bar{\rho} \tilde{u}_j}{\partial x_j} = 0
\tag{2.36}
$$

$$
\frac{\partial \bar{\rho} \tilde{u}_i}{\partial t} + \frac{\partial \bar{\rho} \tilde{u}_i \tilde{u}_k}{\partial x_k} = -\frac{\partial \bar{p}}{\partial x_i} + \frac{\partial \hat{\tau}_{ik}}{\partial x_k}
\tag{2.37}
$$

$$\frac{\partial \bar{\rho}\tilde{e}}{\partial t} + \frac{\partial \left(\bar{\rho}\tilde{e} + \bar{p} \right) \tilde{u}_k}{\partial x_k} = \frac{\partial \left(\tilde{u}_j \hat{\tau}_{ik} + \hat{q}_k \right)}{\partial x_k} \tag{2.38}$$

where $\hat{\tau}_{ik}$ is the total shear stress and $\hat{q}_k$ is the total heat flux in turbulent flows and are given by:

$$\hat{\tau}_{ik} = (\mu + \mu_t) \left[\left(\frac{\partial u_i}{\partial x_k} + \frac{\partial u_k}{\partial x_i} \right) - \frac{2}{3} \delta_{ik} \frac{\partial u_j}{\partial x_j} \right] \tag{2.39}$$

$$\hat{q}_k = -c_p \left(\frac{\mu}{Pr} + \frac{\mu_t}{Pr_t} \right) \frac{\partial T}{\partial x_k} \tag{2.40}$$

where μ_t is the turbulence viscosity and it is determined by the turbulence model being employed and Pr_t is the Prandtl turbulent number equal to 0.9.

The first term in Equation 2.38 can be further expanded as follows:

$$\bar{\rho}\tilde{e} = \frac{\bar{p}}{(\gamma - 1)} + \frac{1}{2}\bar{\rho}(\tilde{u}^2 + \tilde{v}^2 + \tilde{w}^2) + \rho k \tag{2.41}$$

where γ is the ratio of specific heats and ρk is the sub-scale kinetic energy per unit volume given by:

$$\rho k = \frac{1}{2}\bar{\rho}(\widetilde{u_i u_i} - \tilde{u}_i \tilde{u}_i) = -\frac{1}{2}\sigma_{ii} \tag{2.42}$$

For simplicity, all of the tilde and overbar in the equations above will be dropped for the rest of this dissertation.

18

2.5   Detached-Eddy-Simulation

DES is a hybrid turbulence model which involves both the RANS model and the LES model. This is done by applying the RANS model near a solid wall, and the LES model everywhere else away from a solid wall. The Navier-Stokes equations on the preceding section are the generalized equations and in order to be solved need the closure of the sub-grid scale stresses and heat flux terms. This closure can then be based on the DES model suggested by Spalart et al.[65] as described next.

First the sub-grid scale (SGS) stresses σ_{ij} is redefined from Equation 2.29 for the DES turbulence model as follows:

$$\sigma_{ij} = \mu_{DES}\left(\frac{\partial \tilde{u}_i}{\partial x_j} + \frac{\partial \tilde{u}_j}{\partial x_i} - \frac{2}{3}\frac{\partial \tilde{u}_k}{\partial x_k}\delta_{ij}\right) - \frac{2}{3}\rho k \delta_{ij} \qquad i, j = 1, 2, 3 \tag{2.43}$$

The turbulence heat flux Φ_i, from Equation 2.31, is computed as:

$$\Phi_i = C_p \frac{\mu_{DES}}{Pr_t}\frac{\partial \tilde{T}}{\partial x_i} \tag{2.44}$$

where μ_{DES} is the turbulence viscosity defined by the DES turbulence model as presented below:

$$\mu_{DES} = \rho \nu_t = \rho \tilde{\nu} f_{v1} \tag{2.45}$$

The ν_t from Equation 2.45 is the turbulence eddy viscosity and $\tilde{\nu}$ is a working variable which is

19

determined by the Spalart-Allmaras (SA) model [26, 63, 65, 73] from the following equation:

$$\frac{D\tilde{\nu}}{Dt} = c_{b1}\tilde{S}\tilde{\nu}\left(1 - f_{t2}\right) - \left[c_{w1}f_w - \frac{c_{b1}}{k^2}f_{t2}\right]\left[\frac{\tilde{\nu}}{d}\right]^2 + \frac{1}{\sigma}\left[\nabla \cdot \left(\left(\nu + \tilde{\nu}\right)\nabla\tilde{\nu}\right) + c_{b2}(\nabla\tilde{\nu})^2\right] + f_{t1}\left(\Delta q\right)^2 \quad (2.46)$$

Equation 2.46 is the eddy viscosity equation and can be rewritten in a generalized coordinate system as presented below:

$$\frac{\partial \frac{1}{J}\rho\tilde{\nu}}{\partial t} + \frac{\partial \rho\tilde{\nu}U}{\partial \xi} + \frac{\partial \rho\tilde{\nu}V}{\partial \eta} + \frac{\partial \rho\tilde{\nu}W}{\partial \zeta} = \frac{1}{Re}\left(\frac{\partial \frac{\rho}{\sigma}\left(\nu + \tilde{\nu}\right)\left(\mathbf{l} \cdot \nabla\tilde{\nu}\right)}{\partial \xi}\right.$$

$$\left. \cdot + \frac{\partial \frac{\rho}{\sigma}\left(\nu + \tilde{\nu}\right)\left(\mathbf{m} \cdot \nabla\tilde{\nu}\right)}{\partial \eta} + \frac{\partial \frac{\rho}{\sigma}\left(\nu + \tilde{\nu}\right)\left(\mathbf{n} \cdot \nabla\tilde{\nu}\right)}{\partial \zeta} + \frac{1}{J}S_\nu\right) \quad (2.47)$$

where

$$S_\nu = \rho C_{b1}\left(1 - f_{t2}\right)\tilde{S}\tilde{\nu} + \frac{1}{Re}\left[-\rho\left(C_{w1}f_w - \frac{C_{b1}}{\kappa^2}f_{t2}\right)\left(\frac{\tilde{\nu}}{d}\right)^2\right.$$
$$\left. + \frac{\rho}{\sigma}C_{b2}\left(\nabla\tilde{\nu}\right)^2 - \frac{1}{\sigma}\left(\nu + \tilde{\nu}\right)\nabla\tilde{\nu} \cdot \nabla\rho\right] + Re\left[\rho f_{t1}\left(\Delta q\right)^2\right] \quad (2.48)$$

According to the SA one equation model, the closure coefficients for the eddy viscosity equation above are set as follows:

$$C_{b1} = 0.1355, \ C_{b2} = 0.622, \ \sigma = \frac{2}{3},$$
$$C_{w1} = \frac{c_{b1}}{k^2} + (1 + c_{b2})/\sigma, \ C_{w2} = 0.3, \ C_{w3} = 2.0,$$
$$\kappa = 0.41, \ C_{v1} = 7.1, \ C_{t1} = 1.0, \ C_{t2} = 2.0, \ C_{t3} = 1.1, \ C_{t4} = 2.0$$

For turbulent flow, the NS Equations 2.16 are solved together with Equation 2.47 when using the SA one-equation turbulence model.

The eddy viscosity ν_t and the scalar term $\tilde{S}$ in Equation 2.46 are computed from:

$$\nu_t = \tilde{\nu} f_{v1} \qquad f_{v1} = \frac{\chi^3}{\chi^3 + c_{v1}^3} \qquad \chi = \frac{\tilde{\nu}}{\nu} \tag{2.49}$$

$$\tilde{S} = S + \frac{\tilde{\nu}}{k^2 d^2} f_{v2}, \qquad f_{v2} = 1 - \frac{\chi}{1 + \chi f_{v1}} \tag{2.50}$$

where ν is the molecular viscosity and S is the magnitude of the vorticity defined as:

$$S = \sqrt{2\omega_{ij}\omega_{ij}} \tag{2.51}$$

where ω_{ij} is the fluid particle angular velocity given by:

$$\omega_{ij} = \frac{1}{2}\left(\frac{\partial u_i}{\partial x_j} - \frac{\partial u_j}{\partial x_i}\right) \tag{2.52}$$

The functions f_w, f_{t2}, and the trip function f_{t1} are defined as follows:

$$f_w = g\left(\frac{1 + c_{w3}^6}{g^6 + c_{w3}^6}\right)^{1/6}, \qquad g = r + c_{w2}(r^6 - r), \qquad r = \frac{\tilde{\nu}}{\tilde{S}k^2 d^2} \tag{2.53}$$

$$f_{t2} = C_{t3}exp\left(-C_{t4}\chi^2\right) \tag{2.54}$$

$$f_{t1} = C_{t1}g_t exp\left[-C_{t2}\frac{\omega_t^2}{\Delta U^2}\left(d^2 + g_t^2 d_t^2\right)\right], \quad g_t = min\left(0.1, \frac{\Delta q}{\omega_t \Delta x_t}\right) \tag{2.55}$$

where k is the Karmann constant, ω_t is the vorticity of the wall at the wall boundary layer trip location, d is the distance to the closest wall, d_t is the distance of the trip location to the field point, Δq is the difference of the velocities between the trip location and the field point, and Δx_t is the grid spacing along the wall at the trip location. The subscript t indicates that the variable is referring to the trip location. The trip location is where the flow transition smoothly from laminar flow to turbulent and should not be located outside the boundary layer.

In order to apply the DES model, the SA model coefficients c_{t1} and c_{t3} are set to zero to assume a fully turbulent boundary layer, as in most problems the exact location of the trip point is not known. The distance to the nearest wall d is redefined and replaced by $\tilde{d}$ as follows:

$$\tilde{d} = min(d, C_{DES}\Delta) \tag{2.56}$$

where C_{DES} is a constant and Δ is the grid cell's largest spacing in all directions.

When the boundary later is close to the walls, then $\tilde{d} = d$ and the turbulence is simulated using the SA model [63], a RANS model. When away from the boundary layer, then the distance to the nearest wall is defined by $\tilde{d} = C_{DES}\Delta$. Eventually, when the production and destruction terms of the model are balanced, the length scale $\tilde{d}$ will have a Smagorinsky[60]-like eddy viscosity and the turbulence will then be simulated by the LES model. The coefficient $C_{DES} = 0.65$ is used as set in the homogeneous turbulence[59]. The Pr_t number takes the value of 0.9 within the boundary layer for RANS mode and 0.5 away from the wall for LES mode.

The generalized eddy viscosity Equation 2.47 coupled with the filtered Navier-Stokes Equations 2.16 with the DES turbulence closure can be written in a conservative form in the generalized

coordinate system (ξ, η, ζ) as follows:

$$\frac{\partial Q}{\partial t} + \frac{\partial \mathbf{E}}{\partial \xi} + \frac{\partial \mathbf{F}}{\partial \eta} + \frac{\partial \mathbf{G}}{\partial \zeta} = \frac{1}{Re}\left(\frac{\partial \mathbf{R}}{\partial \xi} + \frac{\partial \mathbf{S}}{\partial \eta} + \frac{\partial \mathbf{T}}{\partial \zeta} + D\right) \tag{2.57}$$

where,

$$Q = \frac{1}{J}\begin{bmatrix} \rho \\ \rho u \\ \rho v \\ \rho w \\ \rho e \\ \rho \tilde{\nu} \end{bmatrix} \tag{2.58}$$

$$\mathbf{E} = \begin{bmatrix} \rho U \\ \rho u U + l_x p \\ \rho v U + l_y p \\ \rho w U + l_z p \\ (\rho e + p) U - l_t p \\ \rho \tilde{\nu} U \end{bmatrix}, \mathbf{F} = \begin{bmatrix} \rho V \\ \rho u V + m_x p \\ \rho v V + m_y p \\ \rho w V + m_z p \\ (\rho e + p) V - m_t p \\ \rho \tilde{\nu} V \end{bmatrix}, \mathbf{G} = \begin{bmatrix} \rho W \\ \rho u W + n_x p \\ \rho v W + n_y p \\ \rho w W + n_z p \\ (\rho e + p) W - n_t p \\ \rho \tilde{\nu} W \end{bmatrix} \tag{2.59}$$

$$
\mathbf{R} = \begin{bmatrix} 0 \\ l_k \tau_{xk} \\ l_k \tau_{yk} \\ l_k \tau_{zk} \\ l_k \beta_k \\ \frac{\rho}{\sigma} (\nu + \tilde{\nu}) (\mathbf{l} \cdot \nabla \tilde{\nu}) \end{bmatrix} , \; \mathbf{S} = \begin{bmatrix} 0 \\ m_k \tau_{xk} \\ m_k \tau_{yk} \\ m_k \tau_{zk} \\ m_k \beta_k \\ \frac{\rho}{\sigma} (\nu + \tilde{\nu}) (\mathbf{m} \cdot \nabla \tilde{\nu}) \end{bmatrix} , \; \mathbf{T} = \begin{bmatrix} 0 \\ n_k \tau_{xk} \\ n_k \tau_{yk} \\ n_k \tau_{zk} \\ n_k \beta_k \\ \frac{\rho}{\sigma} (\nu + \tilde{\nu}) (\mathbf{n} \cdot \nabla \tilde{\nu}) \end{bmatrix}
$$

$$
\tag{2.60}
$$

$$
D = \frac{1}{J} \begin{bmatrix} 0 \\ 0 \\ 0 \\ 0 \\ 0 \\ S_\nu \end{bmatrix} \tag{2.61}
$$

where U, V, W are defined the same way is as in Equation 2.33 and β_k is computed as:

$$
\beta_k = u_i \tau_{ki} - q_k \tag{2.62}
$$

Finally, the shear-stress τ_{ik} and total heat flux q_k in generalized coordinates for the DES turbulence models are defined as:

$$
\tau_{ik} = (\mu + \mu_{DES} Re) \left[\left(\frac{\partial u_i}{\partial x_k} + \frac{\partial u_k}{\partial x_i} \right) - \frac{2}{3} \delta_{ik} \frac{\partial u_j}{\partial x_j} \right] \tag{2.63}
$$

$$q_k = -\frac{1}{(\gamma - 1) M_\infty^2} \left(\frac{\mu}{Pr} + \frac{\mu_{DES} Re}{Pr_t} \right) \frac{\partial T}{\partial x_k} \tag{2.64}$$

2.6 Delayed-Detached-Eddy Simulation

The DDES formulation introduced by Spalart et al.[64], based on the SA one equation turbulence model [63], suggests some modifications to his previous DES model [65], presented in section 2.5, given that in wide boundary layers and shallow separation regions the DES simulation can present erroneous behavior. This may occur when the thickness of the boundary layer is greater than the grid spacing parallel to the wall, making the transition from RANS to LES earlier. With the new modified DDES, the RANS model is retained longer for thick boundary layers independent of the grid spacing. The DES model is adjusted as follows.

The SGS stresses formulation from the SA definition is modified by redefining the non-dimensional parameter r from Equation 2.53 to:

$$r_d = \frac{\nu_t + \nu}{(U_{i,j} U_{i,j})^{0.5} k^2 d^2} \tag{2.65}$$

where $U_{i,j}$ are the velocity gradients, and the subscript d refers to delayed for DDES. This parameter is modified in this form so it can be applied to any eddy-viscous model.

The redefined dimensionless parameter r_d is applied in the following function:

$$f_d = 1 - tanh([8r_d]^3) \tag{2.66}$$

The coefficients 8 and 3 from Equation 2.66 are acquired from DDES flat plate boundary layer tests[64] by matching the solution to the RANS results. Using the new function f_d, the DES

distance to the nearest wall $\tilde{d}$ from Equation 2.56 can be modified and be redefined for DDES as follows:

$$\tilde{d} = d - f_d max(0, d - C_{DES}\Delta) \tag{2.67}$$

where $\tilde{d}$ is filtered and Δ is the largest spacing of the grid cell in all the directions. DDES then behaves as a RANS model when near a wall such that within the boundary layer, $\tilde{d} = d$, and as an LES model away from the walls such that away from the boundary layer $\tilde{d} = d - f_d (d - C_{DES}\Delta)$.

The modification in how the distance to the nearest wall $\tilde{d}$ is defined reduces the grey transition area between RANS and LES. The qualitative change of the new $\tilde{d}$ is very significant, depending now on the eddy-viscosity field. The DDES model can now refuse the transition to LES if not ready, when the function f_d, using the value of r_d, indicates that the point still lies within the boundary layer. The opposite also occurs; when there is massive separation indicated by f_d, the change from RANS to LES takes place in the simulation.

Further improvement to the definition of the transition from RANS to LES is made in the improved Delayed Detached Eddy Simulation (iDDES) turbulence model. The main adjustments made to the iDDES model from its predecesor DDES are outlined by Travin et al. [68] including the definition of the LES scale and the Wall-Modelled Large-Eddy Simulation (WMLES) which resolve the turbulence definition near the solid walls. The f_d function introduced for DDES is redefined as follows:

$$f_{hyb} = max \left\{ (1 - f_d) , f_{step} \right\} \tag{2.68}$$

where f_d is the delay function of DDES as given by Equation 2.66 and f_{step} is given by:

$$f_{step} = min\left(2\exp\left(-9\alpha^2\right), 1.0\right) \tag{2.69}$$

where

$$\alpha = \frac{0.25 - d_w}{h_{max}} \tag{2.70}$$

The new function f_{step} introduced by iDDES is only active when the model operates in WMLES, making a quick transition from RANS to LES inside the boundary layer. This transition is allowed to happen as long as the wall distance is within the range of $0.5h_{max} < d_w < h_{max}$ where h_{max} is the maximum local grid spacing.

2.7 Large Eddy Simulation

The LES Smagorinsky model performs spatial filtering of the velocity fluctuations to decompose them into large scales, which are numerically resolved, and small scales, which are modeled. The Smagorinsky-Lilly model with Van Driest damping [60] models the SGS by employing an eddy viscosity approach. In this approach it is hypothesized that a turbulent eddy viscosity exists at the small scales and that the stresses are in equilibrium at the interface between the large and small scales. The eddy viscosity $\tilde{\mu}_t$ is defined as:

$$\tilde{\mu}_t = \bar{\rho}C_s^2 l^2 \sqrt{2S_{ij}S_{ij}} \tag{2.71}$$

where C_s is the Smagorinsky constant, S_{ij} is the rate-of strain tensor given by:

$$S_{ij} = \frac{\left(\frac{\partial u_i}{\partial x_j} + \frac{\partial u_j}{\partial x_i}\right)}{2} \tag{2.72}$$

and l is the model length scale given by:

$$l = (\Delta)^{1/3}\sqrt{(1 - \exp(-y^+/26))^3} \tag{2.73}$$

where Δ is the volume of the cell.

Typical variations of the Smagorinsky model involve modifications to the SGS length scale expression (l) and the filter method used. Although in this approach the cube root of the cell volume is used to filter the scales, Gaussian filtering can be performed based on the strain rate or velocity fluctuations in flow. Additionally, other LES models seek to improve upon the definition of the model constant C_s. In the Smagorinsky-Lilly model this value is held constant and typically equal to 0.1. In the dynamic Smagorinsky method [21], later studied by [56] for complex geometries, the model constant is computed dynamically and allowed to change in time and space. In this work, a dynamic choric Smagorinsky model is employed with the following definition for the Smagorinsky model constant:

$$C_s = \frac{<K*m>}{<m*m>} \tag{2.74}$$

where the angled brackets represent averaging over the whole domain, valid in homogeneous turbulence, K is defined as:

$$K = \frac{1}{2}(\widetilde{u_i u_j} - \tilde{u}_i\tilde{u}_j), \tag{2.75}$$

and m as:

$$m = \Delta^2(4||\tilde{D}||^2 - ||\widetilde{D}||^2).$$ (2.76)

$\tilde{D}$ is modeled as the deviatoric component of the symmetric gradient of the velocity field, i.e., $\tilde{D} = dev(\text{symm}(\nabla U))$. The dynamic Smagorinsky constant ranges from 0 to 1. The constant grows near the boundary region towards unity and is zero in regions where velocity gradients are small [67]. This model assumes homogeneous turbulence at the SGS scales, although non-homogeneous models do exist in the literature [41].

2.8   Implementation of Governing Equations in OpenFOAM

The computational models introduced in this dissertation for the study of autorotation are implemented and examined using OpenFOAM [33], an open source object-oriented CFD code written in C++, with LES and hybrid LES turbulence modeling. This code is chosen given its ability to run in Message Parsing Interface (MPI) for parallel computing, facilitation of model implementation due to its object-oriented nature, and its large library of turbulence models. OpenFOAM stands for Open source Field Operation And Manipulation.

For unsteady flows, the Navier-Stokes governing equations described in this Chapter are solved in OpenFOAM with the use of the Pressure Implicit Split Operator (PISO) algorithm introduced by Issa [31]. The PISO algorithm is a pressure-velocity coupled iterative method.

CHAPTER 3: INCORPORATING RIGID BODY DYNAMICS THROUGH MESH MORPHING

3.1   Incorporating Rigid Body Dynamics - Application to Autorotating Square Flat Plate

In this section, a method to incorporate the rigid body dynamics (RBD) of a single rigid body into the CFD computations is summarized. The specific rigid body of interest is a square flat plate, rotating in the presence of a flow field. A schematic diagram of the setup will be given later in this section. The reason to pursue modeling this system is because it presents a simple form of autorotation for which experimental and simulation data are available in the literature to validate against. More details on the experiment and model validation will be discussed in Section 4.1. First, the approach for incorporating the RBD is described. The RBD model implemented into OpenFOAM is adopted from the symplectic splitting method described by Dullweber et al.[15]. This method can be viewed as constructing the numerical solution of the dynamics by stringing together a sequence of exact solutions of partial *Hamiltonians*. The parts of the Hamiltonian *H* are the kinetic and potential parts. The method is suitable for reducing computational errors, especially for simulations run over longer time-periods. Once implemented, this simplectic model calculates the solid body's angular velocity in response to the instantaneous fluid forces, which in turn defines the mesh motion. This generates the two-way coupling between the solid body and fluid flow around it.

Given the large possible degrees of freedom of a rigid body that is free to rotate and translate, the best approach to solve complex problems of this nature, such as autorotation, is to use the aforementioned Hamiltonian-based symplectic structure. The Hamiltonian of a system is its total

energy and is given by the following equation:

$$H\left(\mathbf{p}, \boldsymbol{\pi}, \mathbf{q}, \mathbf{Q}\right) = T\left(\mathbf{p}, \boldsymbol{\pi}\right) + V\left(\mathbf{q}, \mathbf{Q}\right) \tag{3.1}$$

where $\mathbf{p}$ is the linear momentum vector, $\boldsymbol{\pi}$ is the angular momentum vector, $\mathbf{q}$ is the position of the center of mass vector, $\mathbf{Q}$ is the 3×3 orientation matrix, and T and V are the kinetic and potential energies of the rigid body. The orientation matrix $\mathbf{Q}$ is constrained such that it is always a rotation matrix, this is done by setting $\mathbf{Q}^T\mathbf{Q} = 1$. The kinetic energy can further be divided into translational kinetic energy and rotational energy such that:

$$T\left(\mathbf{p}, \boldsymbol{\pi}\right) = T^{rot}\left(\boldsymbol{\pi}\right) + T^{trans}\left(\mathbf{p}\right) \tag{3.2}$$

where T^{trans} is defined as:

$$T^{trans}\left(\mathbf{p}\right) = \frac{\mathbf{p}^2}{2m} \tag{3.3}$$

where m is the total mass of the rigid body.

The calculation of the T^{rot} term is more complicated to compute and therefore is approximated using a time-reversible splitting symplectic method as described by McLachlan[48] and Reich[53], preserving the total linear and angular momentum. Here, in every time-step, the orientation dynamics of the rigid body is integrated by a sequence of planar rotations. The differential equations of motion for the kinetic energy term in the Hamiltonian equation are given by:

$$\frac{d}{dt}\mathbf{q} = \frac{\mathbf{p}}{m}$$

$$\frac{d}{dt}\mathbf{p} = 0$$

$$\frac{d}{dt}\mathbf{Q} = \mathbf{Q} \operatorname{skew}\left(\mathbf{I}^{-1}\boldsymbol{\pi}\right)$$

$$\frac{d}{dt}\boldsymbol{\pi} = \boldsymbol{\pi} \times \left(\mathbf{I}^{-1}\boldsymbol{\pi}\right) \tag{3.4}$$

where $\mathbf{I}$ is the moment of inertia tensor and the skew of a vector $\mathbf{a}$ is given by:

$$\operatorname{skew}(\mathbf{a}) = \begin{pmatrix} 0 & -a_3 & a_2 \\ a_3 & 0 & -a_1 \\ -a_2 & a_1 & 0 \end{pmatrix} \tag{3.5}$$

In this work, the coupled CFD-RBD model is implemented for an autorotating square flat plate. Assuming the rigid body rotates about its principal axes, the moment of inertia tensor $\mathbf{I}$ becomes a diagonal matrix. The principal moments of inertia for a plate are given by:

$$I_{xx} = \frac{1}{12}M\left(b^2 + c^2\right) \qquad I_{yy} = \frac{1}{12}M\left(a^2 + c^2\right) \qquad I_{zz} = \frac{1}{12}M\left(b^2 + a^2\right) \tag{3.6}$$

where M is the total mass and a, b, and c are the dimensions of the plate in x, y and z directions respectively. The simplicity of a diagonal inertia tensor helps to calculate the rotational motion of

32

the rigid body with a series of elementary functions described by:

$$\mathscr{R}\left(\Delta t\right) = \mathscr{R}_x\left(\frac{1}{2}\Delta t\right)\mathscr{R}_y\left(\frac{1}{2}\Delta t\right)\mathscr{R}_z\left(\Delta t\right)\mathscr{R}_y\left(\frac{1}{2}\Delta t\right)\mathscr{R}_x\left(\frac{1}{2}\Delta t\right) \tag{3.7}$$

where the elementary functions, $\mathscr{R}_x$, $\mathscr{R}_x$, and $\mathscr{R}_x$, are responsible for updating the angular momentum and the orientation matrix at each time step while preserving the total angular momentum of the rigid body. They are defined as:

$$\mathscr{R}_x = \begin{cases} \mathbf{Q}\left(t\right) = \mathbf{Q}_0\mathbf{R}_x\left(\theta\right)^T \\ \boldsymbol{\pi}\left(t\right) = \mathbf{R}_x\left(\theta\right)\boldsymbol{\pi}_0 \end{cases}, \qquad \mathscr{R}_y = \begin{cases} \mathbf{Q}\left(t\right) = \mathbf{Q}_0\mathbf{R}_y\left(\theta\right)^T \\ \boldsymbol{\pi}\left(t\right) = \mathbf{R}_y\left(\theta\right)\boldsymbol{\pi}_0 \end{cases}$$

$$\mathscr{R}_z = \begin{cases} \mathbf{Q}\left(t\right) = \mathbf{Q}_0\mathbf{R}_z\left(\theta\right)^T \\ \boldsymbol{\pi}\left(t\right) = \mathbf{R}_z\left(\theta\right)\boldsymbol{\pi}_0 \end{cases} \tag{3.8}$$

where the subscript 0 indicates that the property is the same throughout the rotation sequence and $\mathbf{R}_x\left(\theta\right)$, $\mathbf{R}_y\left(\theta\right)$, and $\mathbf{R}_z\left(\theta\right)$ are the rotation matrices about an angle θ in the x, y, and z-axis, respectively. The angle θ is defined as:

$$\theta = \frac{t\pi_i}{I_i} \tag{3.9}$$

The differential equations of motion for the potential energy term in the Hamiltonian equation are:

$$\frac{d}{dt}\mathbf{q} = 0$$

$$\frac{d}{dt}\mathbf{p} = -\frac{\partial V}{\partial \mathbf{q}}$$

$$\frac{d}{dt}\mathbf{Q} = 0$$

$$\frac{d}{dt}\boldsymbol{\pi} = -\mathrm{curl}\left(\mathbf{Q}^T\frac{\partial V}{\partial \mathbf{Q}}\right) \tag{3.10}$$

where the curl is the mapping of the 3×3 matrix into a vector in a $\mathbf{R^3}$ space. These equations for the potential energy term, in contrast to the kinetic energy, are easier to solve given that the position vector and rotation matrices are constant for potential energy. The equations presented above are implemented into OpenFOAM, [78], with the use of septernions and quaternions. In this CFD code, the motion of a rigid body in a 3D space is described by a septernion. The septernion consists of 7 elements describing a body's translation by the use of a vector and a body's rotation by the use of a quaternion.

The implementation of the rigid body motion coupled with the CFD code is presented next. The CFD code with an adequate turbulence model calculates the forces and torques on the rigid body which then are used to calculate the angular momentum $\boldsymbol{\pi}$ and the linear momentum $\mathbf{p}$ from one time step to the next by using the following equations:

$$\boldsymbol{\pi}^{n+1/2} = \boldsymbol{\pi}^n + \frac{1}{2}\Delta t \boldsymbol{\tau}^n \tag{3.11}$$

$$\mathbf{p}^{n+1/2} = \mathbf{p}^n + \frac{1}{2}\Delta t \mathbf{f}^n \tag{3.12}$$

where τ^n is the torque vector and $\mathbf{f^n}$ is the force vector at time t^n. Then using the newly calculated linear momentum $\mathbf{p}^{n+1/2}$ from Equation 3.12, the center of mass location is updated for the next time step simulation as follows:

$$\mathbf{q}^{n+1} = \mathbf{q}^n + \Delta t \mathbf{p}^{n+1/2} m \tag{3.13}$$

The vector in the septernion is responsible for this calculation and only the translation of the rigid body is taken into consideration and communicated to the mesh. The next step is to update the orientation matrix which is responsible for the rotation of the rigid body, this occurs in the quaternion part of the septernion. The orientation matrices $\mathbf{Q}$ as well as the angular momentum π get updated by the use of function $\mathscr{R}$ from Equation 3.7. The series of consecutive rotations for the calculation of $\mathscr{R}$ are presented below:

$$\mathbf{R_1} = \mathbf{R_x}\left(\frac{1}{2}\Delta t\frac{\pi_1}{I_1}\right), \qquad \mathbf{R_2} = \mathbf{R_y}\left(\frac{1}{2}\Delta t\frac{\pi_2}{I_2}\right)$$

$$\mathbf{R_3} = \mathbf{R_z}\left(\Delta t\frac{\pi_3}{I_3}\right), \qquad \mathbf{R_4} = \mathbf{R_y}\left(\frac{1}{2}\Delta t\frac{\pi_2}{I_2}\right)$$

$$\mathbf{R_5} = \mathbf{R_x}\left(\frac{1}{2}\Delta t\frac{\pi_1}{I_1}\right) \tag{3.14}$$

where the subscripts $1, 2, 3$ are the (x, y, z) components of each vector quantity, π_i is the angular momentum, I_i are the elements of the diagonal of the inertia tensor of the rigid body, and the

rotations by an angle ϕ around the x, y, and x axes are given by the following equations:

$$\mathbf{R}_x(\phi) = \begin{pmatrix} 1 & 0 & 0 \\ 0 & \cos\phi & -\sin\phi \\ 0 & \sin\phi & \cos\phi \end{pmatrix} \tag{3.15}$$

$$\mathbf{R}_y(\phi) = \begin{pmatrix} \cos\phi & 0 & \sin\phi \\ 0 & 1 & 0 \\ -\sin\phi & 0 & \cos\phi \end{pmatrix} \tag{3.16}$$

$$\mathbf{R}_z(\phi) = \begin{pmatrix} \cos\phi & -\sin\phi & 0 \\ \sin\phi & \cos\phi & 0 \\ 0 & 0 & 1 \end{pmatrix} \tag{3.17}$$

These 5 rotations according to the function $\mathscr{R}$ are applied at every time step to update the angular momentum $\boldsymbol{\pi}$ and orientation matrix $\mathbf{Q}$ of the rigid body, and subsequently the mesh updates to its new position.

With the mesh translated and rotated to its new position, and with the position and orientation matrix updated, the CFD code can calculate again the forces and torques and propagate the momentum the rest of the half step as:

$$\boldsymbol{\pi}^{n+1} = \boldsymbol{\pi}^{n+1/2} + \frac{1}{2}\Delta t \boldsymbol{\tau}^{n+1} \tag{3.18}$$

$$\mathbf{p}^{n+1} = \mathbf{p}^{n+1/2} + \frac{1}{2}\Delta t \mathbf{f}^{n+1} \tag{3.19}$$

In every time step, the Equations 3.11-3.19 presented above get calculated by using the forces gathered from the turbulence model simulation, making of this a coupled CFD-RBD model.

The method presented above lets a body move freely in all 6 degrees of freedom (DOF), therefore constraints and restraints are introduced into the coupled CFD-RBD model to control the DOF and motion range of the rigid body motion. Equation 3.20 below shows the translational and rotational constraint tensors for the full 6 DOF.

$$\text{Translational constraint tensor} = \begin{pmatrix} 1 & 0 & 0 & 0 & 1 & 0 & 0 & 0 & 1 \end{pmatrix}$$

$$\text{Rotational constraint tensor} = \begin{pmatrix} 1 & 0 & 0 & 0 & 1 & 0 & 0 & 0 & 1 \end{pmatrix} \tag{3.20}$$

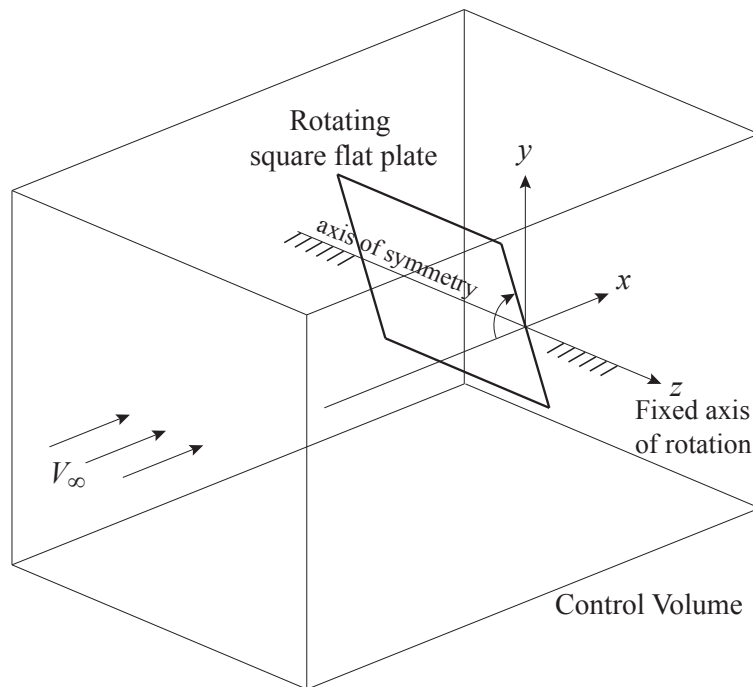A schematic diagram of the autorotating square flat plate is shown is Fig. 3.1.

Figure 3.1: Schematic diagram of an autorotating square flat plate

For this system, a restraint is implemented in the form of a bearing damper to take into account the friction present by adding a bearing friction torque to the already present aerodynamic torques. This is later described in more detail in Section 4.1.2. Additionally, two constraints are introduced to limit the motion of the plate. The first one is a fixed point constraint, not allowing for any translational motion, and the second one is an axis constraint, only allowing for rotation about the z-axis. These two constraints simplify the the model into a 1-DOF case, only allowing the flat plate to rotate, without any form of translation, about its principal z-axis. Equation 3.21 presents the new translational and rotational constraints for the 1-DOF case, only allowing it to rotate about the z-axis.

$$\text{Translational constraint tensor} = \begin{pmatrix} 0 & 0 & 0 & 0 & 0 & 0 & 0 & 0 & 0 \end{pmatrix}$$

$$\text{Rotational constraint tensor} = \begin{pmatrix} 0 & 0 & 0 & 0 & 0 & 0 & 0 & 0 & 1 \end{pmatrix} \tag{3.21}$$

Once a geometrically valid mesh is carefully constructed, the first step in the implementation of the CFD-RBD model into OpenFOAM is to divide the mesh into the sections that are allowed to morph and those that are not. This is done by assigning a value between 1 and 0, where 0 means the mesh is completely stationary and 1 means the mesh is allows to morph the most. By doing this, the model knows which cells to apply the equations of motion described above.

For the autorotating square flat plate case, described in more detail in Section 4.1.2 of this dissertation, Fig. 3.2 shows the moving mesh motion regions for a single rigid body, where the dark blue area represents the stationary mesh and the inside light blue area represents the section of the mesh that is allowed to rotate. By setting the whole moving area of the mesh to the same value, the mesh section rotates all together without any deformation, therefore it is important that the interface between the moving and the stationary mesh sections is allowed to slide and does

not remain attached to each other. This way the mesh cells remain stable without introducing any numerical errors into the calculation. OpenFOAM uses Arbitrary Mesh Interface (AMI), [19], between the sliding boundaries of the mesh to communicate the information at the interfaces. The sliding interface between the stationary outer region and the rotating inner region of the flat plate case is seen in Fig. 3.3.
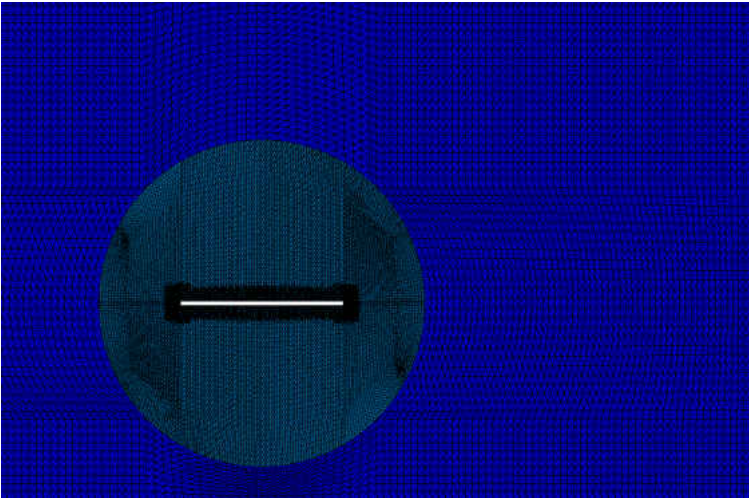

Figure 3.2: Moving mesh motion regions for the autorotating flat plate
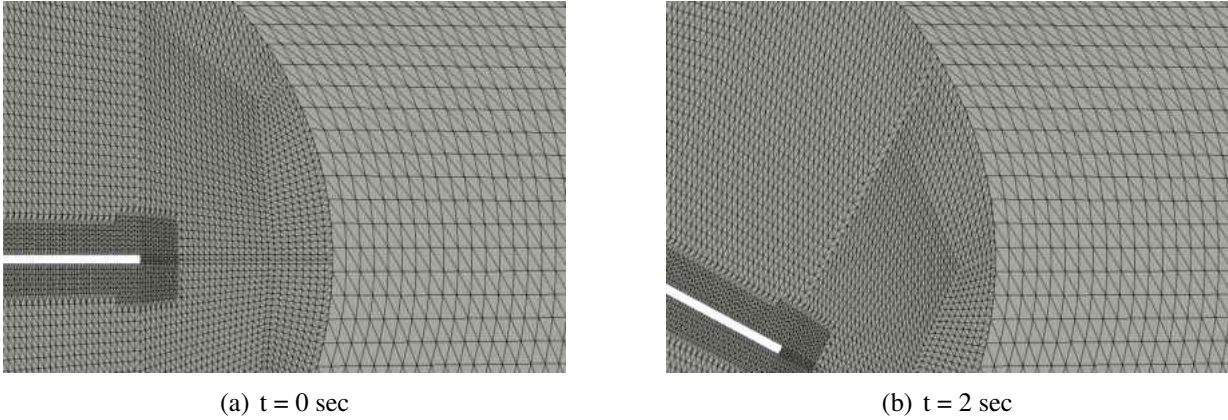

(a) t = 0 sec

(b) t = 2 sec

Figure 3.3: Sliding interface between stationary and rotating mesh regions for autorotating plate

3.2 Incorporating Multi-body Dynamics into Mesh Motion: Application to 3-Blade Rotor

The symplectic splitting method described in Section 3.1 was applied to capture the dynamics of one rigid body, namely the autorotating flat plate. In this section, its application is extended to multi-body dynamics (MBD). Specific application is to a 3-blade rotor where each blade is allowed to flap about a hinge that connects it to the hub of the rotor. The setup is shown in Fig. 1.1. This 3-blade rotor system has more complicated fluid structure interactions. However, the system it is more closely representative of a typical rotor than the autorotating flat plate. Furthermore, as part of this work, experimental data could be acquire from lab experiments with a similar rotor. The details of this experimental set-up will be given in Section 4.2.1.

The same method of Section 3.1 is utilized for the MBD model, but instead of being applied to just one rigid body it is applied for several bodies at the same time. As a result, the set of Equations 3.11-3.19 gets employed more than once in every time step. For the particular case of the autorotating 3-blade rotor, this set of equations gets executed four times, once for each of the individual blades and once for the whole rotor structure containing the hub. The importance of this multi-body model is that the forces calculated by the CFD code for each of the individual blades contribute to the total forces that in turn are responsible for the motion of the complete structure. In other words, in every time step the coupled CFD and rigid body model calculates the forces on each of the solid bodies, calculates the motions, and the mesh transforms under the prescribed constraints and limits.

In this model, for each solid body new linear momentum vectors $\mathbf{p_i}$, angular momentum vectors $\boldsymbol{\pi}_i$, center of mass position vectors $\mathbf{q_i}$, and 3×3 orientation matrices $\mathbf{Q_i}$, where $i = 1, 2, 3, 4$, are introduced. Each body is then able to move independently from each other, and at the same time contribute to the motion of the complete structure such that the linear and angular momentum for

the whole system are calculated by:

$$\mathbf{p} = \sum_{n=1}^{i} \mathbf{p}_i, \qquad \boldsymbol{\pi} = \sum_{n=1}^{i} \boldsymbol{\pi}_i \qquad (3.22)$$

where i is the number of solid bodies present in the simulation.

In this work, the coupled CFD-MBD model of Section 3.1 is implemented for an autorotating 3-blade rotor. For the individual blades, the dynamical equations for flapping are implemented in a similar manner as for the rotating flat plate discussed in Section 3.1. Each blade is assumed to be a thin rectangular flat plate. For incorporating the spinning motion, the rotor is approximated as a thin disk, with the following moment of inertias:

$$I_{xx} = I_{zz} = \frac{1}{2}MR^2 \qquad I_{yy} = \frac{1}{4}MR^2 \qquad (3.23)$$

where R is the radius of gyration and M is the effective mass. Similar to the CFD-RBD model, restraints and constraints are implemented into the model to dictate the motion of the rotor structure. To keep the blades and hub rotating about their principal y-axis without any translational motion, a fixed point constraint is implemented. Equation 3.24 below shows the translational and rotational constraint tensors for the multi-body 3-DOF case, allowing the rotor structure to rotate about the x, y and z axes.

$$\text{Translational constraint tensor} = \begin{pmatrix} 0 & 0 & 0 & 0 & 0 & 0 & 0 & 0 & 0 \end{pmatrix}$$

$$\text{Rotational constraint tensor} = \begin{pmatrix} 1 & 0 & 0 & 0 & 1 & 0 & 0 & 0 & 1 \end{pmatrix} \qquad (3.24)$$

Given that the rotational constraint tensor for the rotor allows for rotation about the 3 axes, further limitations have to be implemented for the multi-body mesh motion. For the rotor, the whole structure is allowed to rotate at the same angular velocity about its principal y-axis, while each blade is allowed to rotate about its local x-axis at the hinge joint that connects it to the hub. Therefore the motion has to be constraint such that each blade does not rotate independently about its local y-axis, otherwise the blades will rotate at a different pace than the hub, creating large mesh deformations, incorrect dynamical behavior and an unstable numerical simulation.

The x and z components of the angular momentum vector, π, for the whole 3-blade rotor system is set to zero, forcing motion only about the global y-axis. Simultaneously, the y component of the angular momentum vectors, π_1, π_2, and π_3, for each blade is set to zero, forcing them to just flap independently from each but not rotate about their y-axes. Equation 3.25 shows the constraints applied to each of the four angular momentum vectors present in the rotor simulation.

$$\text{For} \quad \boldsymbol{\pi} : \qquad \pi_1 = 0 \qquad \qquad \pi_3 = 0$$

$$\text{For} \quad \boldsymbol{\pi}_1, \ \boldsymbol{\pi}_2, \ \text{and} \ \boldsymbol{\pi}_3 : \qquad \pi_2 = 0 \tag{3.25}$$

Furthermore, in order to limit the range of flapping angles of the blades, a constraint is introduced such that each blade is not allowed to rotate past a prescribed angle. This not only avoids large morphing of the mesh cells that can lead to numerical instability, but also keeps the rotation within the range of motion that the hinges permit.

Once the MBD model is implemented in OpenFOAM, the first step before simulating the model is to designate the regions of the mesh that will undergo any kind of transformation, the same way that it was done for the CFD-RBD model. The main difference from the single-body model is that now several moving-mesh regions are introduced, each with their own constraints. Given that

depending on the motion of the multi-body system the moving-mesh regions might overlap each other, it is important that the motion is employed in a way that will not sacrifice the quality of the cells of the mesh as this might in turn make the CFD code numerically unstable and the solution will not converge.

The 3-blade autorotating rotor freely rotates about its principal axis, and each individual blade is allowed to flap independently from each other, making of this model a multi-body coupled CFD-RBD simulation. Figure 3.4(a) shows the internal region of the mesh (light blue) that is allowed to rotate and the outer domain (dark blue) of the mesh that is stationary. Figures 3.4(b)-(d) show the regions that the mesh is allowed to morph for capturing the flapping dyamics of each blade.

(a)   (b) Blade 1

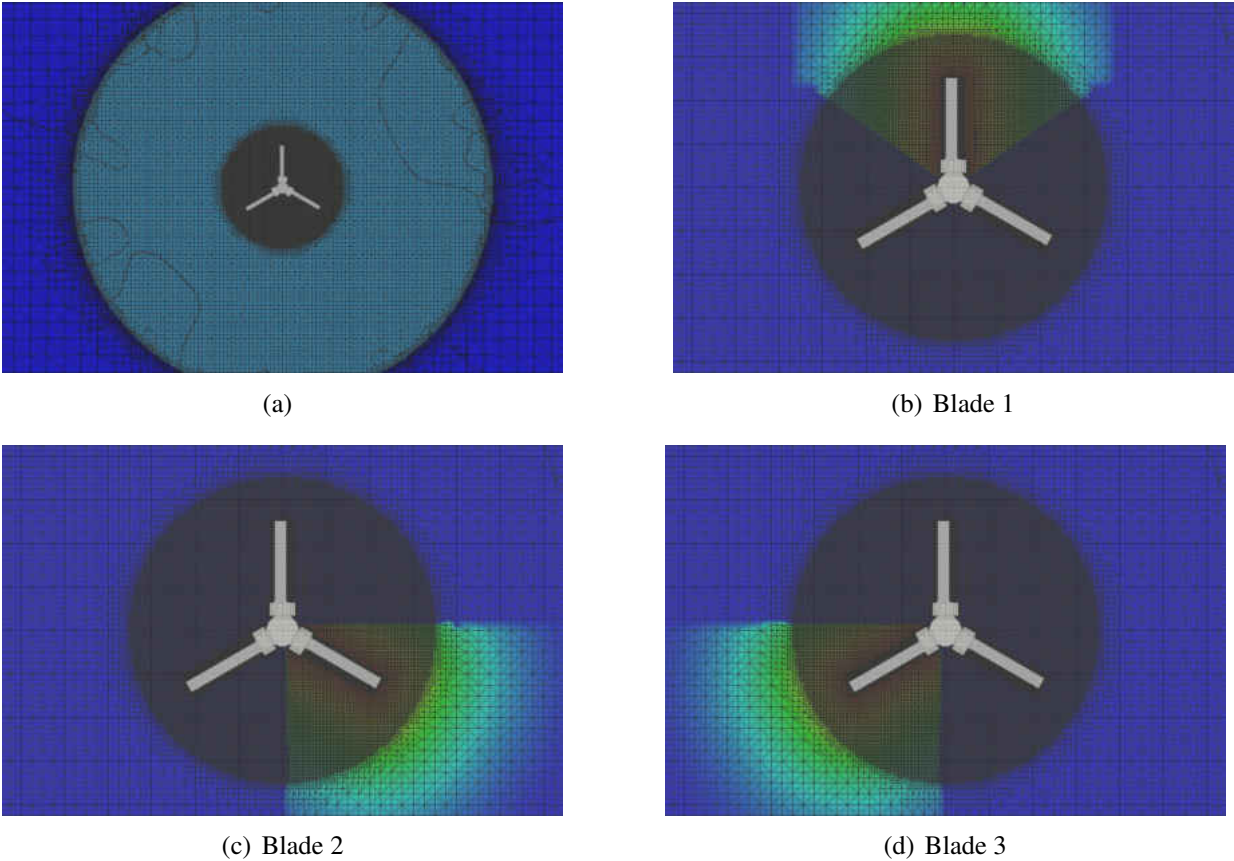(c) Blade 2   (d) Blade 3

Figure 3.4: Moving mesh motion regions for a problem with multiple bodies

The sliding interface between the stationary outer region and the rotating inner region, where

43

each blade is allowed to flap independently from each other, is seen in Fig. 3.5. Figure 3.6 shows a single blade as it rotates and translates, demonstrating the morphing ability of the individual cells within the moving regions of the mesh.
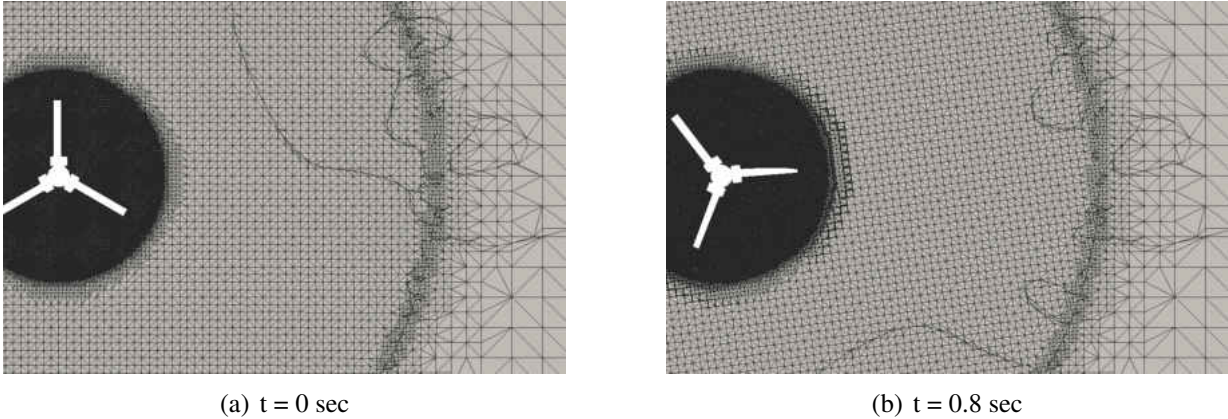

(a) t = 0 sec

(b) t = 0.8 sec

Figure 3.5: Sliding interface between stationary and rotating mesh regions for autorotating 3-blade rotor
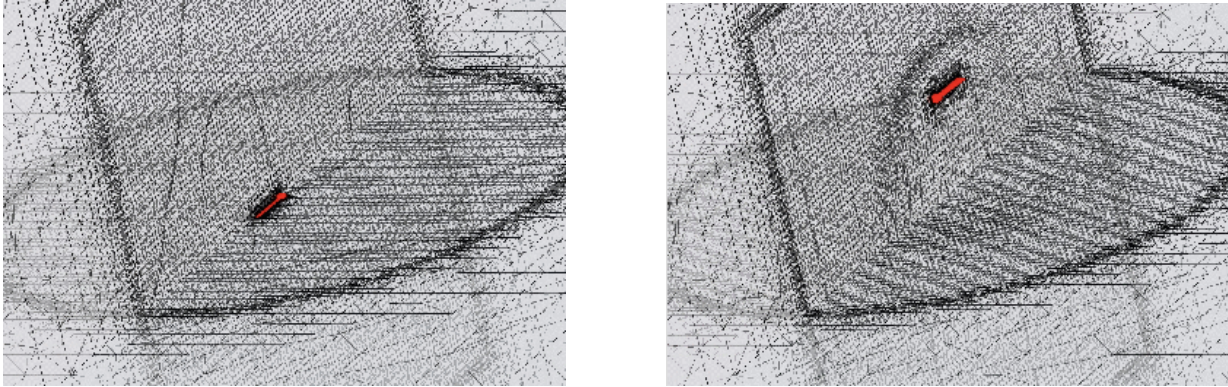
Figure 3.6: Single blade mesh deformation as it rotates and translates inside the moving mesh inner cylinder region

CHAPTER 4: VALIDATION STUDY OF COUPLED CFD

AND RIGID BODY DYNAMICS MODELS

4.1 Coupled CFD and Rigid Body Dynamics (RBD) - Autorotating Square Flat Plate

The CFD-RBD model of the autorotating square flat plate, presented in Section 3.1, is validated by comparing its simulation results with results from several LES models, the Auckland experiment data [47], and the RANS simulations performed by Hargreaves et al.[27]. In these existing works, the system of Fig. 3.1 is considered.

4.1.1 Details of Experimental Setup in [47]

The computational model presented in this work uses for validations purposes the experiments conducted by Martinez et al., [47], in the wind tunnel at the University of Auckland. The plate was mounted on a turntable in an open test section with a range of wind speeds of $U_w = 5$, 7.5 and 10 m/s for the autorotation experiments. The 2.7 kg square plate was made of polystyrene with 1 m length and 0.0254 m thickness, equipped with twenty-four pressure transducers arranged as seen in Fig. 4.1. The reader is referred to [47] for further details on the experimental setup. The data collected by the pressure transducers was used to compute the force coefficients given by $C_N = F_N/(0.5\rho U_w^2 A)$, where $A = 1m^2$. From this data set, drag, lift and moment coefficients were inferred as defined by $C_D = F_{N_x}/(0.5\rho U_w^2 A)$, $C_L = F_{N_y}/(0.5\rho U_w^2 A)$ and $C_M = T/(0.5\rho U_w^2 l^3)$, respectively, where D is the drag force, L is the lift force, T is the torque and l is the characteristic length which in this case is 1 m. In this dissertation, the results for a wind speed of 5 m/s are used for the model validation, as the experimental results of the pressure coefficients for the 7.5 and 10 m/s cases are not readily available in [47].
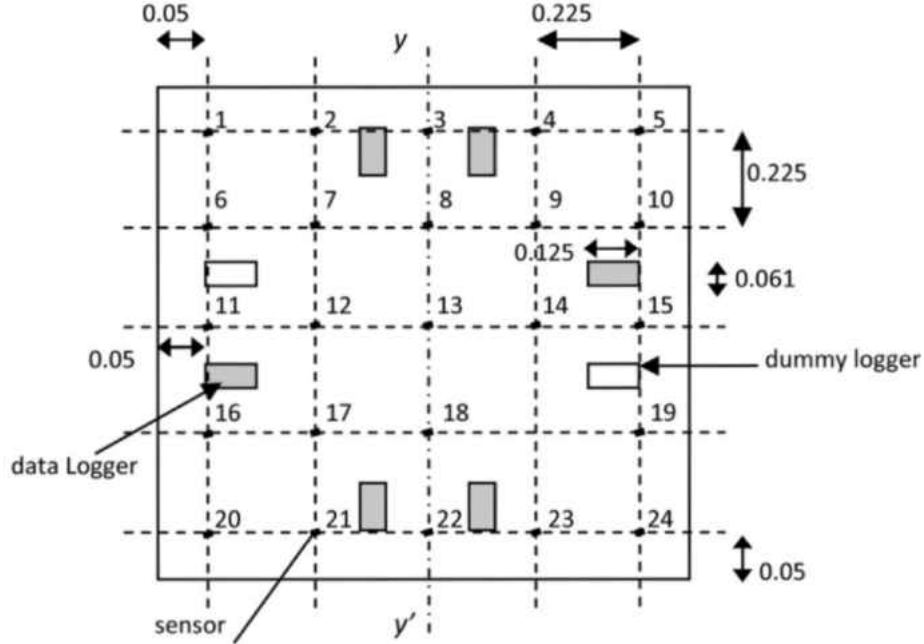
Figure 4.1: Sensor distribution on plate surface for Auckland experimental setup [47]

It is important to note that the experimental results show an increase in the dynamic pressure in the vicinity of the plate compared to the entrance of the tunnel and this is taken into consideration when calculating the aerodynamic force coefficients. The measured increase and employed in the CFD simulation is of 22% for a $U_w = 5\ m/s$. The 22% increased in dynamic pressure measured by [47] has been employed in the CFD simulations, changing the free stream velocity in the vicinity of the plate from $5\ m/s$ to $6.1\ m/s$.

4.1.2   CFD Model Description

Several LES models are used to study the autorotation of a square flat plate. The mesh is completely structured and consists of 4.6 million hexahedral cells, with y^+ values between 10 and 100. Based on the ranges of y^+, wall functions are employed for the turbulence viscosity (ν_t) to model the shear and sub-layer profiles of the boundary layer. The computational domain is made up of two zones, a cylinder containing the plate and the rectangular outer domain, connected by an

Arbitrary Mesh Interface or AMI, [19], as seen in Fig. 4.2 and Fig. 4.3. The outer rectangular test section has dimensions of $15c \times 7c \times 3.5c$ where $c = 1m$. The plate's center is located $1.2c$ from the bottom wall and $5c$ from the inlet.

The moments of inertia from Equation 3.6 can be further simplified for a thin flat plate. The plate, weighting 2.7 kg, has dimensions of 1 m in the x direction, 1 m in the z direction, and 0.0254 m in the y direction. The y dimension is considerably smaller than the x and z dimensions, therefore the plate can be considered thin and this quantity be neglected. The moment of inertia vector is then calculated to be $(0.225 \quad 0.45 \quad 0.225) \ kg \cdot m^2$. At the beginning of the simulation, the initial orientation matrix for the plate, given that the global axes coordinate system is the same as the local fixed frame coordinate system, is:

$$\text{plate} : \mathbf{Q} = \begin{pmatrix} 1 & 0 & 0 \\ 0 & 1 & 0 \\ 0 & 0 & 1 \end{pmatrix} \tag{4.1}$$

As indicated by Spalart et al., [64], DDES is mesh independent (grid density) and therefore y^+ values between 10 and 100 is not of concern. However, LES simulations such as the Smagorinsky-Lilly model need a better defined boundary layer. Therefore $y^+ < 1$ is preferred without the use of a wall function to model the boundary layer. Figs. 4.3(a) and 4.3(b) show the cross-section of the mesh around the flat plate for the two different y^+ values. The mesh with the lower y^+ consists of around 100,000 more cells.

Figure 4.4 shows the comparison of the lift and drag coefficients for the Smagorinsky simulations with the low and high y^+ values. The plots show there is very little difference in the results and grid independence. Therefore, to reduce computational time, the mesh with the larger y^+ will be used for the rest of the simulations and results presented in this dissertation.
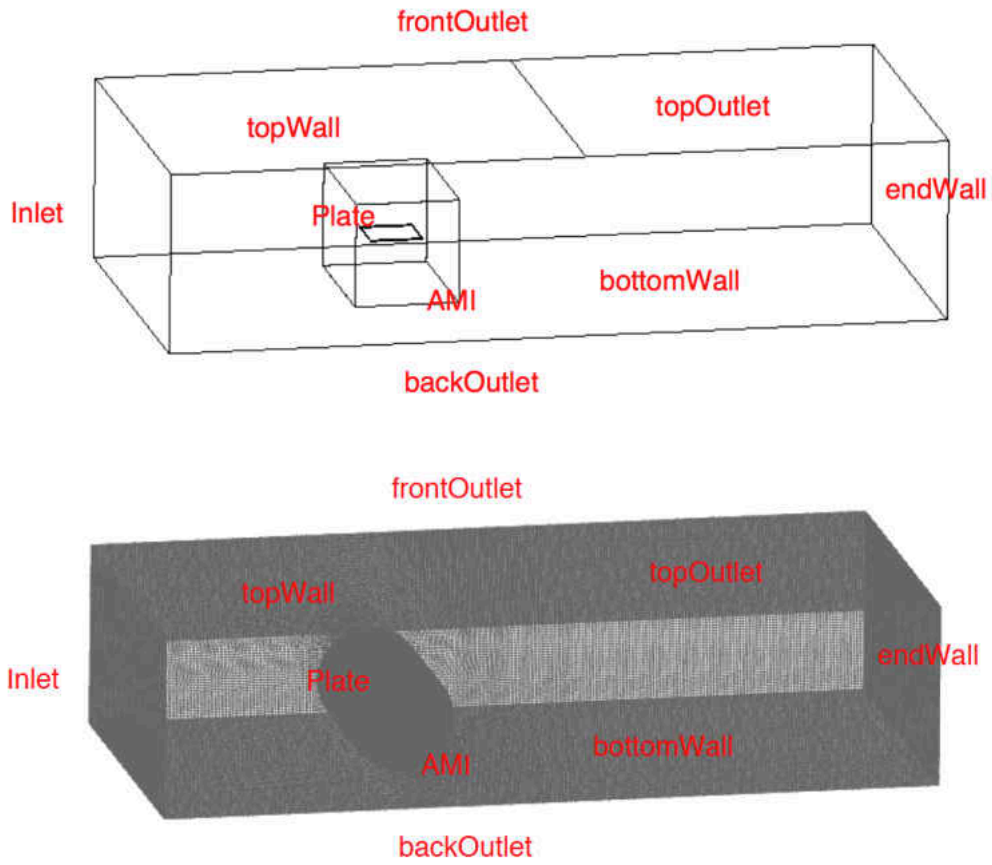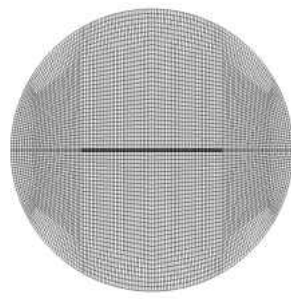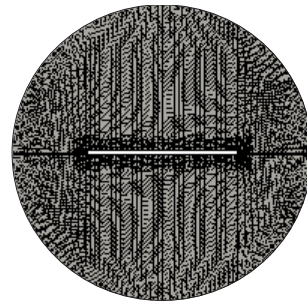
Figure 4.2: Computational domain and boundary conditions setup for autorotating plate CFD simulation

(a) $y+ > 10$

(b) $y+ < 1$

(c) Plate inside rotating cylinder

Figure 4.3: Fully structured computational domain cross-section of mesh around flat plate for (a) $y+ > 10$ and (b) $y+ < 1$ for inner rotating mesh (c) rotating cylinder domain
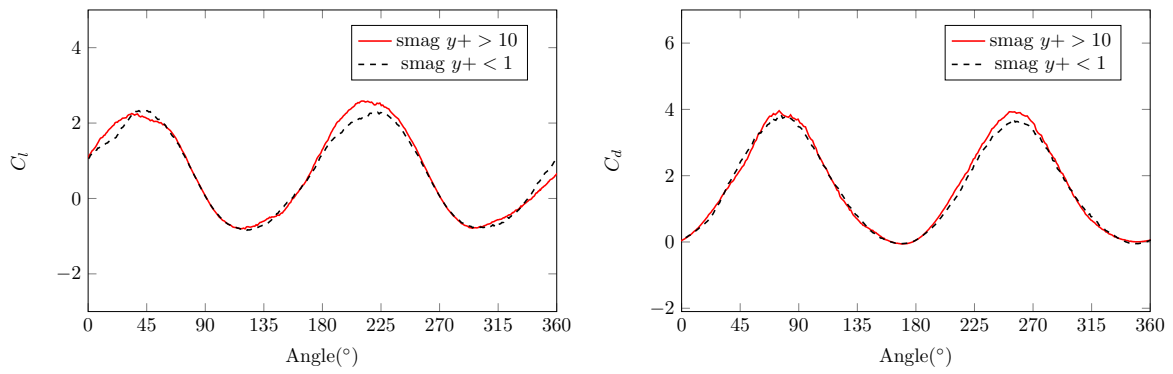
Figure 4.4: Comparison of lift and drag coefficients for a full rotation for different y^+ values for LES

For the computation, the inlet boundary condition was set uniform in the x-direction with an imposed turbulence of 5%. This value was chosen as it is typical for low turbulence wind tunnels. The turbulence is modeled as random fluctuations about a mean velocity (freestream) and it showed little effect on the end results given that the distance between the inlet and the plate was considerable ($d = 5m$). A Reynolds number of $Re = 3.34 \times 10^5$ for $U_w = 5m/s$ is used. As previously mentioned, note that the inlet velocity used in the experiment and simulation is different than the velocity used to calculate the dynamic pressure directly in front of the plate. In order to replicate the experiment as close as possible, the boundary conditions at the front, back and a single top section were set as fixed static pressure outlets under atmospheric conditions. All the walls have a no-slip boundary condition, except for the plate surfaces which are set as moving wall velocity. This is done to take into account the motion computed by the fluid structure interaction (FSI) of the rotating mesh so that there is no flux across the plate.

To provide a better match between the simulation and experimental conditions, a bearing friction sub-model was implemented as suggested by Hargreaves et al.[27]. This model adds a bearing friction torque, T_{fric}, to the aerodynamic torques already acting on the plate during the simulation. T_{fric} is defined as:

$$T_{fric} = (0.5\mu_r d)\sqrt{(mg - L)^2 + D^2} \tag{4.2}$$

where μ_r is the rolling friction coefficient of the bearings, and d is the bore diameter of the bearing block. These were assumed from typical roller bearing parameters to be 0.003 and 0.0254 m respectively, as these values where not given for the Auckland experiment. It was observed that the contribution to the total torque, T_{total}, from T_{fric} was less than 1%.

The coupled CFD-RBD model is carried out in OpenFOAM, [78], using incompressible DDES, iDDES, Smagorinsky with VanDriest damping and dynamic Smagorsinsky models to simulate the small scale turbulence. Given that the plate is only free to rotate on the z-axis, the RBD model is

reduced to a single degree of freedom. The Pressure Implicit with Splitting of Operators (PISO), [33], algorithm is used to solve the Navier-Stokes equation in time with the finite volume method. The 3-D incompressible version of OpenFOAM, [5], is employed to solve the coupled pressure-velocity equations from the discretized momentum equation. A second order time marching Euler scheme is used for the temporal derivatives, while a third order cubic scheme is used for the gradient, divergence and laplacian operations used in the finite volume calculations. No relaxation of the field variables or plate acceleration is used; instead, the Courant number is limited to 0.5, as suggested for LES with FSI problems to avoid any numerical instabilities, [7].

All plate simulations were run in parallel on 102 Intel Xeon 64-bit processors with a time step of 0.0005 s. When running for a total of 120 hours, DDES ran for 5.9 computational seconds, while Smagorinsky ran for 3.8 computational seconds. This shows the limitations of pure LES models compared to hybrid models as it takes approximately 50% more clock time to simulate the same computational time.

### 4.1.3   Comparison of Experimental Data with CFD Results

Figure 4.5 shows the pressure coefficients for half a rotation at various sensor locations. The specific locations chosen in this work correspond to the locations where experimental and RANS data are given in [27]. Hence, this allows for direct comparison between the simulations in this work and the literature. The plate rotates about its z-axis in a clockwise motion. The experimental data presented is the average over a large number of cycles for a 120 sec time frame, while all the simulation data is the instantaneous data from a single cycle. Instantaneous data is reported because of the large clock time needed to run CFD simulations. Running the full time-frame in CFD would require approximately 2880 hours of clock time.

Qualitatively, the computed results agree well with the experimental data. At sensors 6 and 11, located near the edge of the plate, the LES results are significantly better compared to the

RANS results. The maximum deviation from simulation to experiment is reduced by about 50% at sensor 6 and sensor 11, and about 10% at sensors 7 and 8. The RANS results predict a much larger pressure peak which is resolved by LES. This can be be attributed to the LES being able to correctly represent the vortex core pressures as it has the ability to resolve a large portion of the small flow structures that RANS is unable to compute.

Numerical results for the moment coefficient show close resemblance to experimental values as seen in Fig. 4.6. From Fig. 4.6 it can be seen, from the peaks at each rotation, that every other C_m is over-predicted compared to the experimental values. These plots show that C_m consists of several harmonics as seen in Fig. 4.7. The frequency-amplitude signal shown in Fig 4.7 was generated using a discrete Fourier Transform as outlined in [27]. LES results show adequate prediction of the frequencies response, but over-predicts the dominant frequency by approximately 0.1 Hz. This dominant frequency is the same as the vortex shedding frequency which occurs twice in every rotational cycle.

The discrepancy of the frequencies is attributed to the computational burden that prevents prolonged simulations where steady rotational conditions are achieved. The results presented in this work are given for the first 10 seconds of the simulation while the experimental results are collected for the last 10 seconds after the system already running for about 110 seconds.
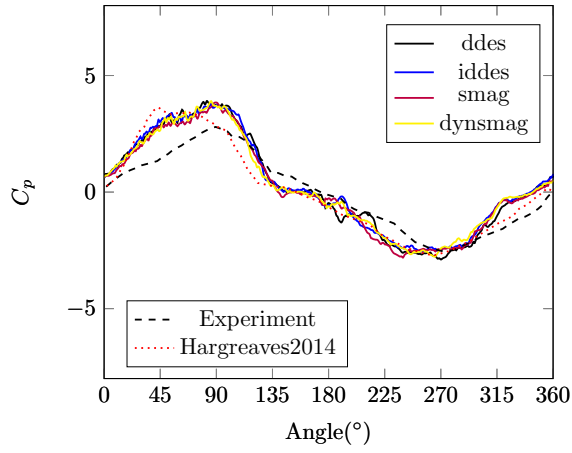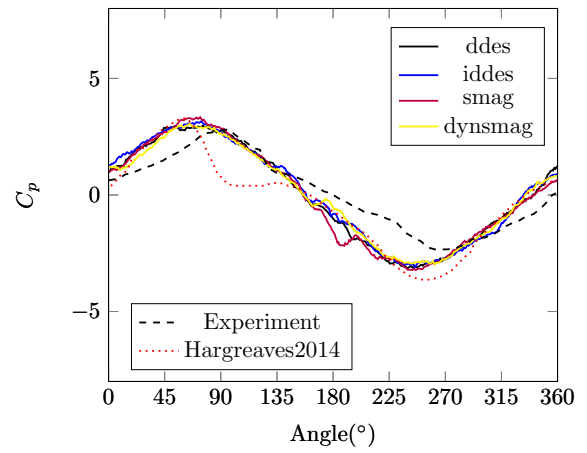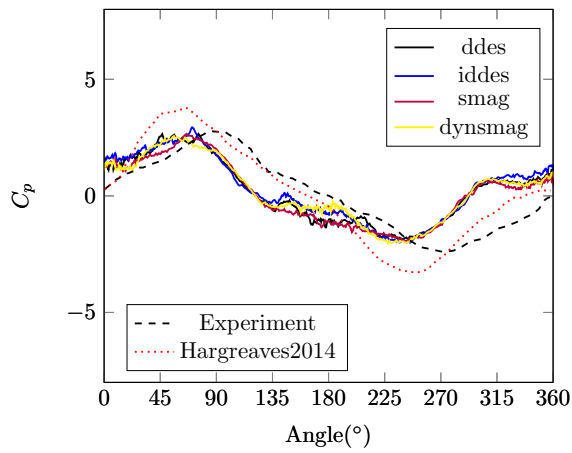
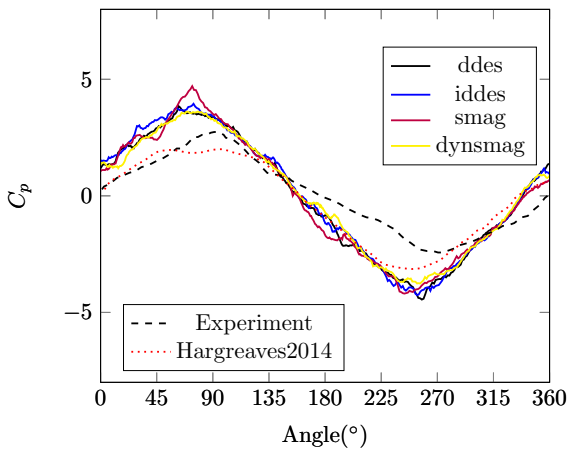(a) Sensor 1
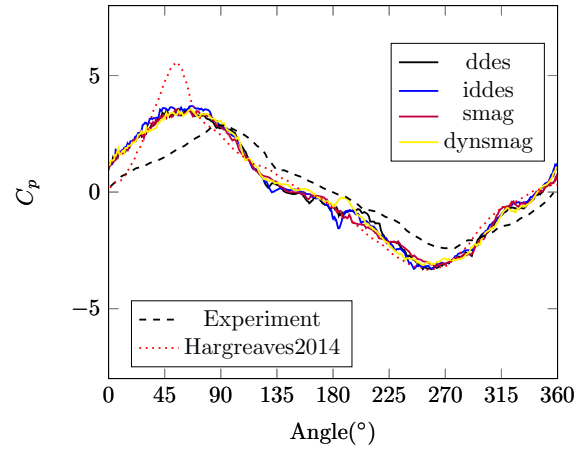
(b) Sensor 6
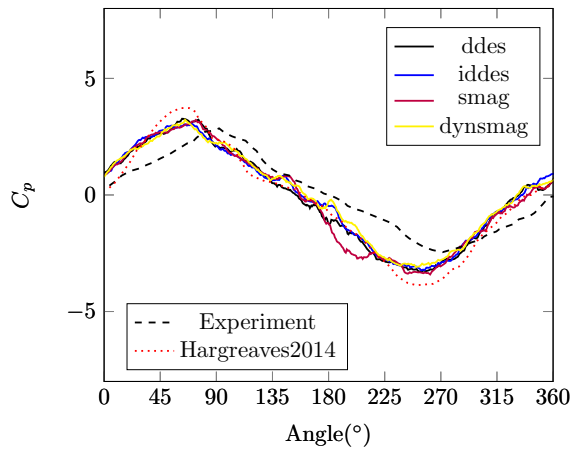
(c) Sensor 7

(d) Sensor 8

(e) Sensor 11

(f) Sensor 13

Figure 4.5: CFD and experimental pressure coefficients at various sensor locations
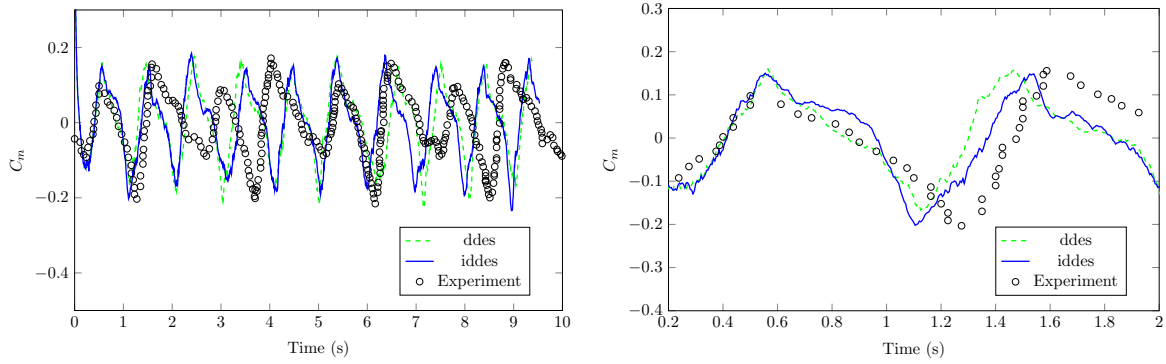
Figure 4.6: Moment coefficients against time for DDES, iDDES and experimental results
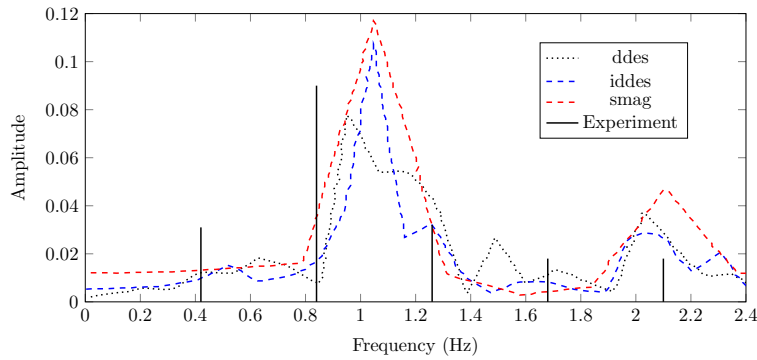

Figure 4.7: Frequency domain representation of computed moment coefficient

Comparisons for the lift and drag coefficients between the simulations and the experimental results can be seen in Fig. 4.8. The CFD results present an over-estimation for both aerodynamic coefficients. However, the same issue was reported in [35] where RANS simulations were performed. There are a number of possible reasons to explain this discrepancy. Mass eccentricity, a possible inadequate bearing friction model, and inaccuracies in the CFD-RBD simulation due to numerical limitation may all affect the prediction of the lift and drag forces. Also, it is important to note that this over-prediction can be attributed to the time averaging done for the experimental results, as it can be seen in Fig. 4.6 that every other peak obtained through experiments have lower values compared to the ones obtained from numerical simulations.
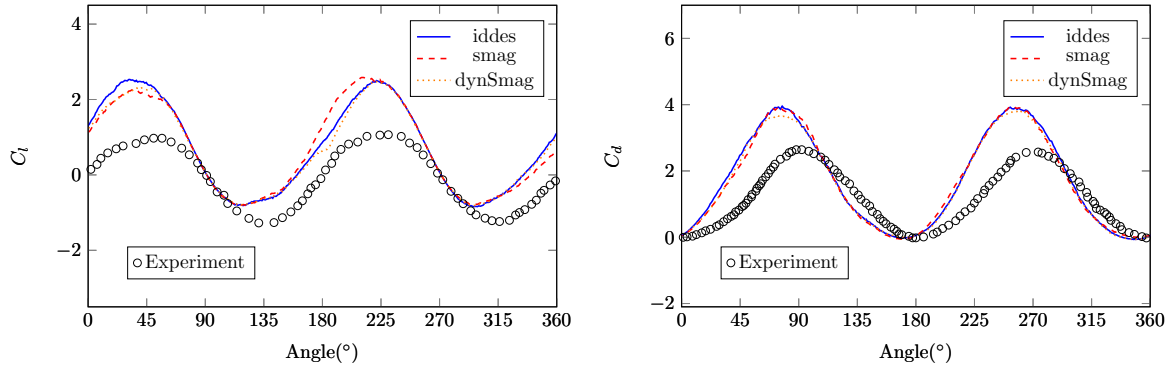
Figure 4.8: Lift and drag coefficients for a full rotation for DDES, iDDES and experimental data

Figure 4.8 shows that variations in the LES model predictions are greater for the lift coefficient, where as all three models predict almost identical behavior for the drag coefficient. This is expected as pressure forces are less dominant in the lift direction, when compared to drag. Consequently, the lift force is influenced more by the viscous forces and turbulent surface interactions which are highly dependent on the LES model in use.

In general, the results of the CFD-RBD model presented in this dissertation closely resemble those from the Auckland experiment. It is also seen that the four different turbulence models used in this work give relatively similar results. Therefore, it is concluded that hybrid methods such as DDES and iDDES can be used in FSI autorotation instead of pure LES methods, saving computational time. Overall, the model validation effort reveals the scope for further research where the discrepancies with experimental data can be further resolved and the model further improved.

4.2   Coupled CFD and Multi Body Dynamics (MBD) - Autorotating 3-Blade Rotor

This section discusses validation of the CFD-MBD model of the autorotating 3-blade rotor, presented in Section 3.2, with experimental results that will be discussed next. Specifically, a

comparison is shown between the results of the iDDES model and the angular velocity and torque data generated in the autorotation experiment.

4.2.1   Details of Experimental Setup

An experimental setup was developed and experiments were designed to measure the rotational speed and aerodynamic torque of a 3-blade rotor that is allowed to freely autorotate in an air flow field. The rotor assembly consists of 3 flapping blades attached to a hub through hinges as seen in Fig. 4.9. The rotor is 3-D printed out of thermoplastics, with a 0.2 m diameter and 23.2 g weight. Figure 4.10 shows the experimental setup of the flapping blade rotor and the fixture used to control the angle of incidence of the rotor with respect to the wind field. Wind is generated using a wind tunnel or through commercially available fans. Experiments are conducted at wind speeds of $5m/s$.

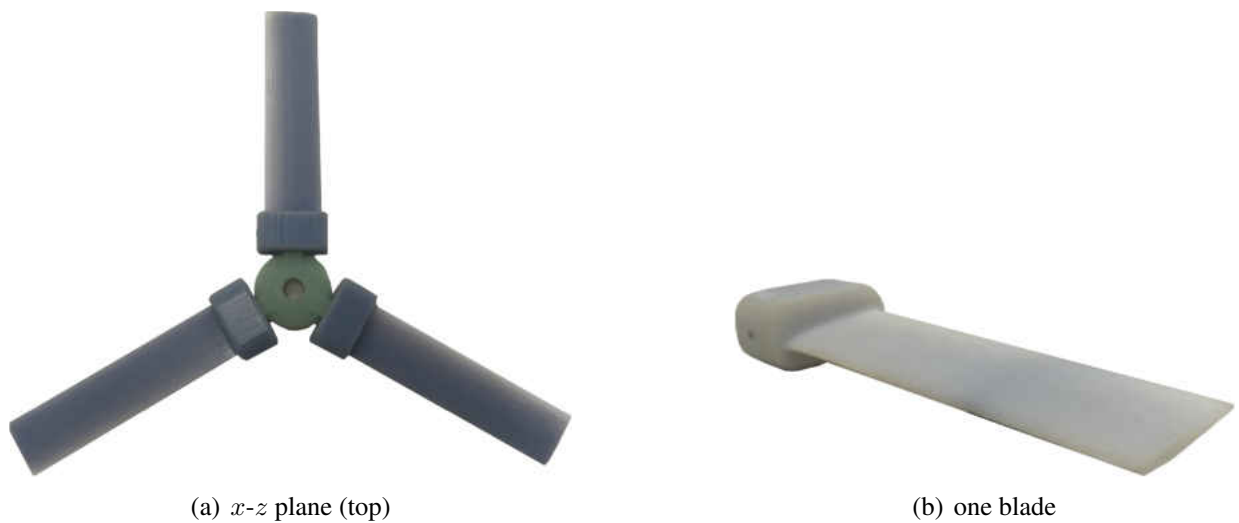(a) x-z plane (top)   (b) one blade
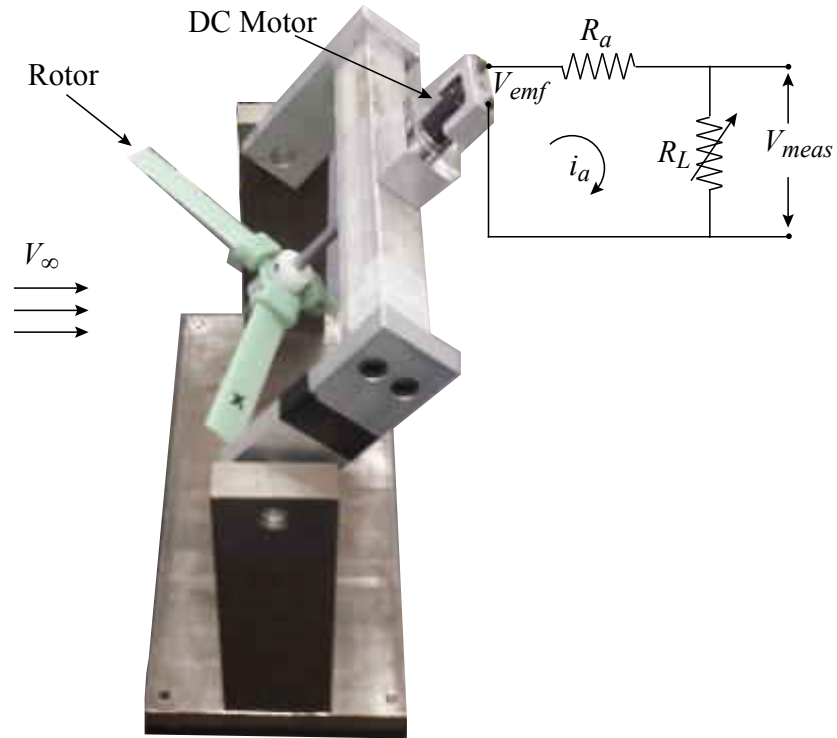
Figure 4.9: 3-D printed rotor

Figure 4.10: Experimental framework of flapping blade rotor to fixture

In order to measure the angular velocity and the aerodynamic torque, a DC motor is used. The motor, attached to the rotor via a rod fixed to the shaft, operates in generator mode. An electrical circuit, as shown in Fig. 4.10, is used to conduct these experiments. The speed, ω, is obtained by using the motor's back electromotive force, V_{emf}, which is induced by the turning of the shaft. The back-emf and the armature current are determined by applying a load resistance, R_L, across the terminals of the generator. From circuit analysis, the armature current, i_a, is determined by:

$$i_a = \frac{V_{meas}}{R_L} \tag{4.3}$$

where V_{meas} is the measured voltage. And the back-emf is computed from:

$$V_{emf} = i_a \left(R_a + R_L \right) = V_{meas} + i_a R_a \tag{4.4}$$

where V_{emf} is the back-emf and R_a is the armature resistance ($R_a \approx 16\Omega$). From the back-emf, the angular velocity, ω, is calculated using the following equation:

$$\omega = \frac{V_{emf}}{K_e} \tag{4.5}$$

where K_e is the speed constant of the motor ($K_e = 1.5 \ mV/rpm$). Finally, from the armature current, the aerodynamic torque, T, is calculated using the following equation:

$$T = K_t i_a \tag{4.6}$$

where K_t is the torque constant of the motor ($K_t = 14.3 \ mN \cdot m/A$). These measurements and calculations are done when the rotor reaches a steady rotating speed, for each experimental run. The experimental framework utilized to gather the data necessary for validation is described in greater detail in [55]. The above outlined experimental setup is useful not only for measuring measuring rotor speeds but also for calculating aerodynamic torques under different loading conditions, i_a. To validate the CFD model, however, the no-load condition is applied, i.e. $i_a = 0$. This implies that the $V_{emf} = V_{meas}$ and at steady state $T = 0$.

4.2.2   CFD Model Description

A hybrid LES model is used to study the autorotation of a 3-blade rotor. The mesh consists of 4 million points, with y^+ values between 3 and 15. The rotor structure weights 0.0232 kg and has

a radius of 0.1 m, the same specifications as the rotor used in the experimental setup described in Section 4.2.1. The 3-D surface mesh of the 3-blade rotor used in the model can be seen in Fig. 4.11.
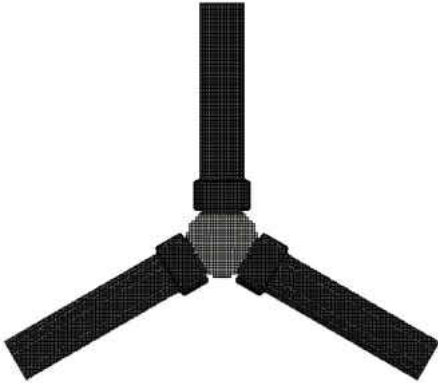
(a) x-z plane (top)

(b) y-x plane (side)

(c) one blade

Figure 4.11: 3-D surface mesh of 3-blade rotor

The computational domain is made up of two zones, a free to rotate cylinder containing the rotor blades and an outside stationary rectangular outer domain, connected by an AMI, as seen in Fig. 4.12. The outer stationary rectangular domain has dimensions of $16c \times 16c \times 16c$ where $c = 0.1m$ and the rotating cylinder has a height of $10c$ and a radius of $5c$. The blade-structure is located in the center of the rotating cylinder domain. Given that iDDES is mesh independent regarding the boundary layer near the surface of the wall, y^+ values between 3 and 15 is acceptable.
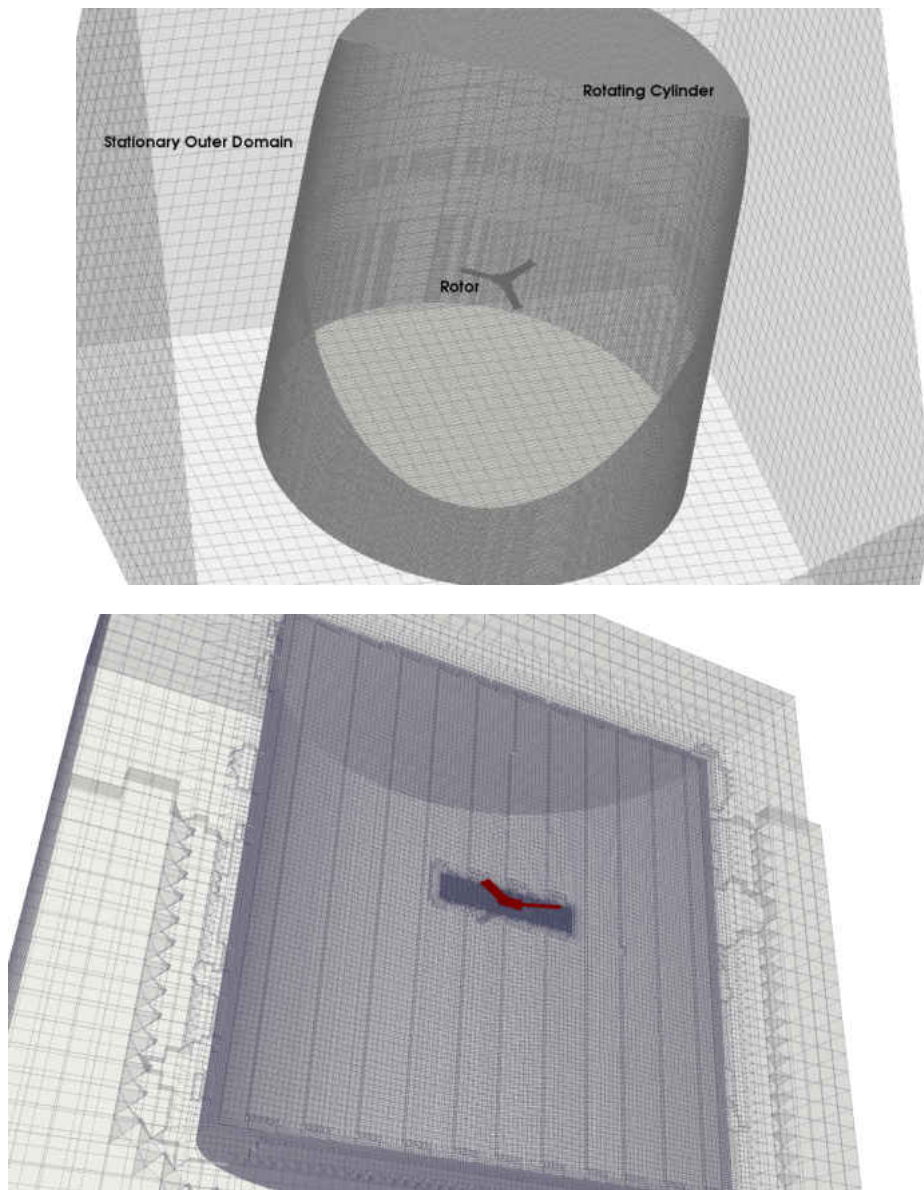

Figure 4.12: Computational domain for 3-blade rotor CFD analysis

At the beginning of the simulation, the initial orientation matrix for the whole blade structure is set as the same as the global axes coordinate system. Updating this orientation matrix will in turn rotate the mesh and calculate the angular velocity of the whole system. For the individual flapping of each blade, the model needs the input of three further orientation matrices, one for each of the blades. The blade are 120° apart from each other, therefore blade1 is rotated 0°, blade2 is rotated 120°, and blade3 is rotated 240° with respect to the global axes reference frame and their initial orientation matrices $\mathbf{Q}$ are given by:

$$
\text{blade1} : \mathbf{Q} = \begin{pmatrix} 1 & 0 & 0 \\ 0 & 1 & 0 \\ 0 & 0 & 1 \end{pmatrix}, \qquad \text{blade2} : \mathbf{Q} = \begin{pmatrix} -0.5 & 0 & -0.866 \\ 0 & 1 & 0 \\ 0.866 & 0 & -0.5 \end{pmatrix}
$$

$$
\text{blade3} : \mathbf{Q} = \begin{pmatrix} -0.5 & 0 & 0.866 \\ 0 & 1 & 0 \\ -0.866 & 0 & -0.5 \end{pmatrix} \tag{4.7}
$$

The inlet boundary condition is set to uniform velocity with an imposed turbulence of 5%. The inlet velocity is set at $5m/s$ for a flow direction of 40°, 45° and 50°, and $10m/s$ for a flow direction of 30°, 40°, 45° and 50°. The rest of the faces of the stationary outer domain are set as fixed static pressure outlets under atmospheric conditions. In order to take into consideration the resultant motion of the mesh computed by the FSI, the surface of the blades and hub are set equal to the moving wall velocity. For the multi body model, the bearing friction sub-model introduced in the CFD-RBD model in Section 4.1 is not implemented as the simulated speed correlated well with experimental data obtained from the setup described in Section 4.2.1.

The 3-D incompressible version of OpenFOAM, [5], with the iDDES turbulence model is used to solve the Navier-Stokes equations using the PISO, [33], algorithm. For the finite volume calculations, a third order cubic scheme is used for the gradient, divergence and laplacian operations,

while a second order time marching Euler scheme is used for the temporal derivatives. All rotor simulations were run in parallel on 80 Intel Xeon 64-bit processors with a variable time step of 1e-6 s. For iDDES simulations with a free stream velocity of 5 m/s ran an average of 0.8 computational seconds when running for a total of 200 real time hours. When running for a total of 300 hours, iDDES simulations with a free stream velocity of 10 m/s ran an average of 1.1 computational seconds.

4.2.3   Comparison of Experimental Data with CFD Results

For the 3-blade rotor, the two variables compared between experiments and simulations are the rotor angular speed and the aerodynamic torque. Figure 4.13 shows the angular velocity plotted against time at different angles of incidence for a free stream velocity of 5 m/s. For both simulations and experiments, the rotor autorotates in a clockwise direction about its main y-axis. The three plots on the left column present angular velocities when the system is closed to steady state rotation in both simulations and experiments. The three plots on the right column, on the other hand, depict a gradual acceleration of the rotor before it reaches steady rotation. Numerical results of the angular velocity show close resemblance to the experimental data as evident from Fig. 4.13. The raw experimental data in the figures is the data collected directly from the source without any data processing. When averaged, the data matches very closely with the CFD simulations.
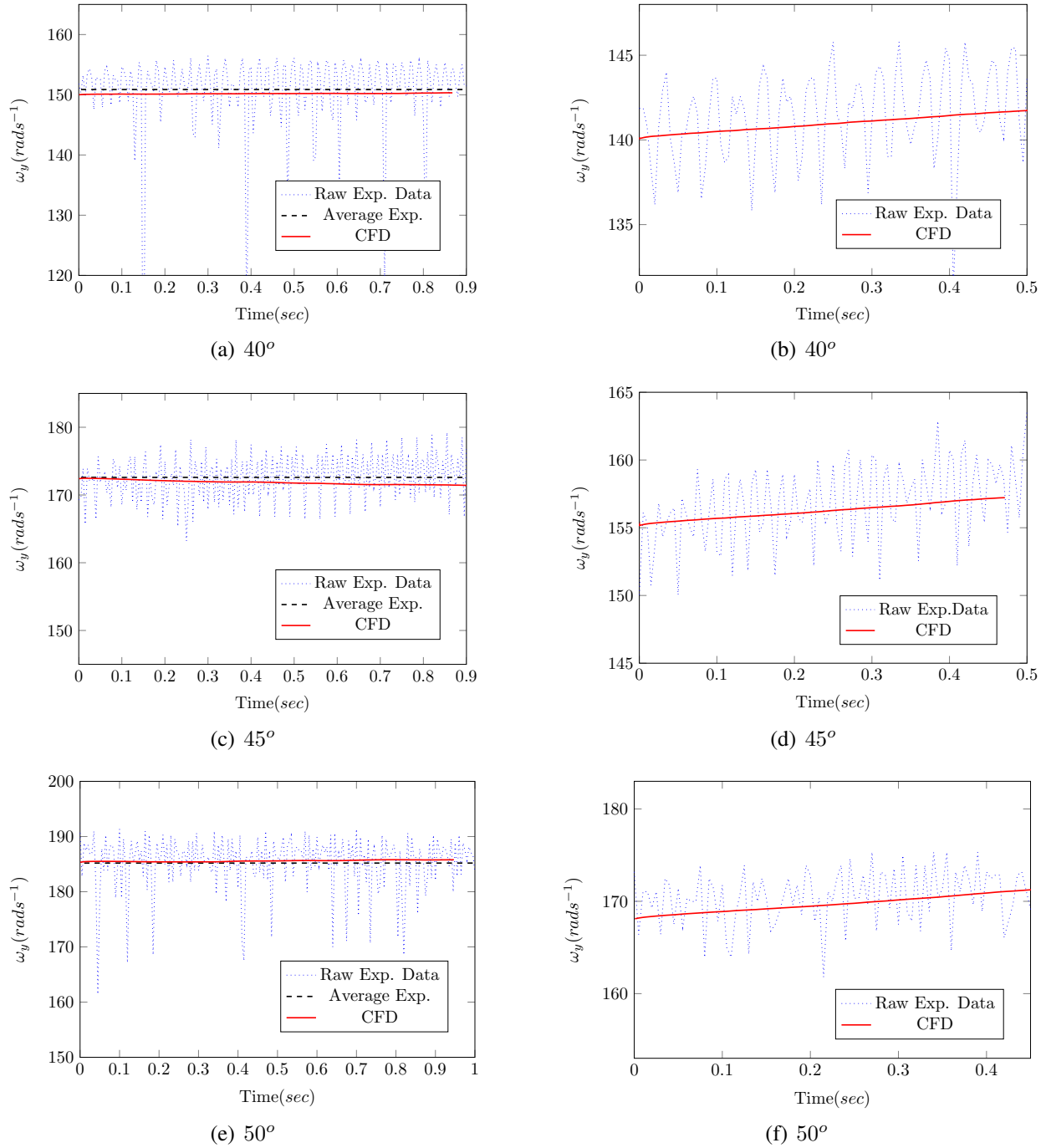
Figure 4.13: Angular velocity at different angles of incidence for a free stream velocity of $5m/s$

Comparison for the torque versus time at different angles of incidence between the simulations and experimental results can be seen in Fig. 4.14. Torque is used to determine when the rotor has

reached steady state rotation, as when torque reaches zero the angular velocity stops increasing or decreasing. From Fig. 4.14 it can be seen that both experimental data and CFD results show a constant torque very close to zero, demonstrating that the simulations and experiments reached a steady state rotation. However, even though the torque is very close to zero, the constant torque for the experimental data is larger than the CFD data, this could be attributed to the friction present in the rod fixed to the shaft, which is not being modelled in the CFD-MBD simulation.
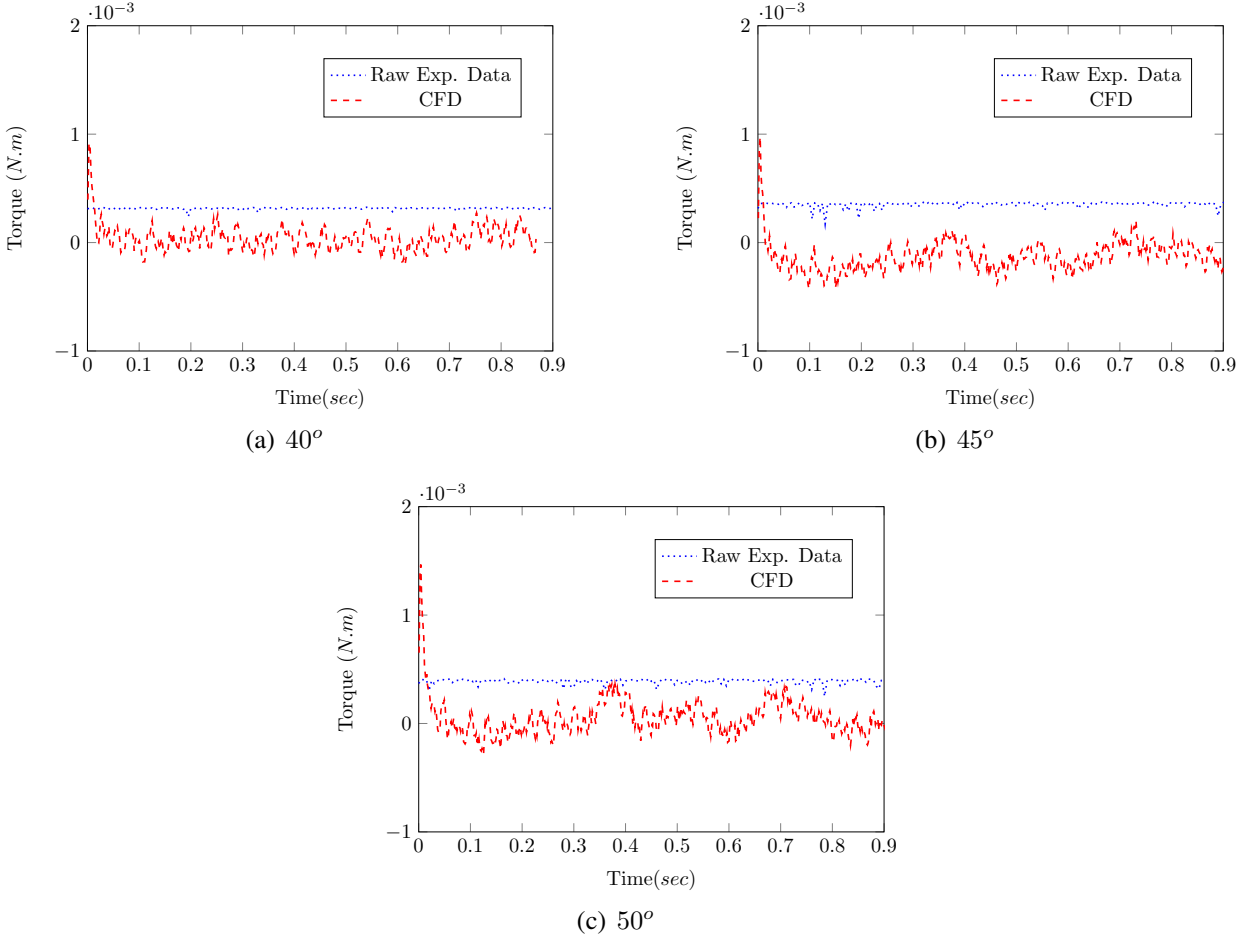

(a) 40°

(b) 45°

(c) 50°

Figure 4.14: Torque at different angles of incidence for a free stream velocity of $5m/s$

The coupled CFD-MBD using the iDDES turbulence model presented in this dissertation presents results that show agreement with the experimental data generated from the autorotating rotor experiment.

CHAPTER 5: RESULTS AND DISCUSSION

This chapter provides additional simulation data and flow visualizations to demonstrate the efficacy of the two CFD models, namely that of the autorotating square plate and the autorotating 3-blade rotor. Overall, the results provide further insight into the extensive fluid structure interactions that are present in both cases.

5.1   Autorotating Square Flat Plate

Continuing from Section 4.1, this section provides further simulation data of the aurotorating square flat plate. Figure 5.1 shows the instantaneous static pressure contours at the back surface of the plate at different angles of rotation. Figures 5.1(a), (b) and (c) correspond to Smagorinsky turbulence model, Figs. 5.1(d), (e), and (f) correspond to iDDES turbulence model, and Figs. 5.1(g), (h), and (i) correspond to RANS solutions from Hargreaves et al., [27]. The contour levels for the Smagorinsky (top three plots) and the iDDES (middle three plots) present the same contour levels as the RANS solutions (bottom three plots) presented by Hagreaves et al.,[27]. Qualitatively the contours for all three results presented are similar. However, both Smagorinsky and iDDES results seem to show a slightly better resolution of the vortices near the corners and side edges of the plate than the RANS solution, especially at an angle of incidence of 120°.
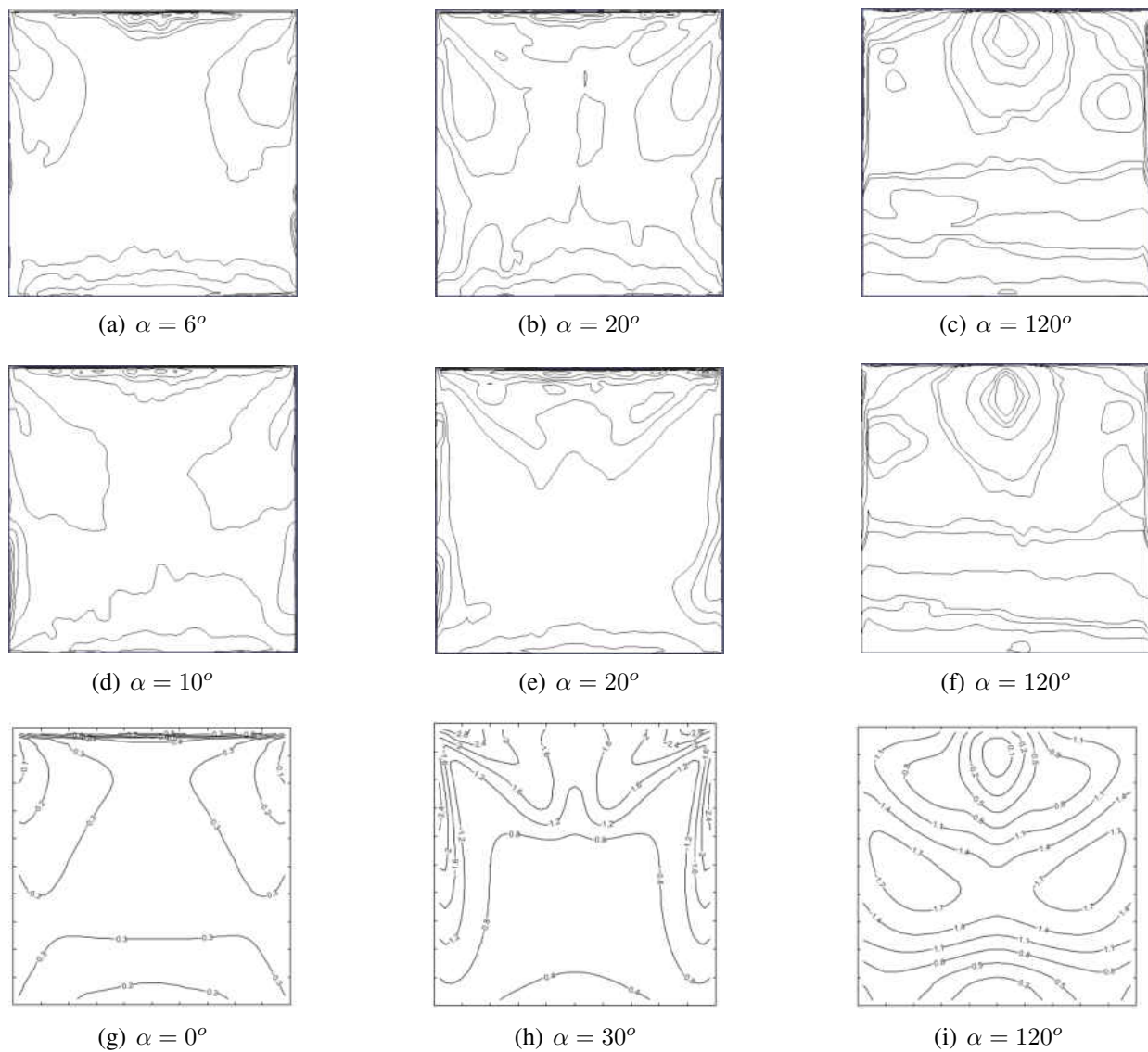
(a) $\alpha = 6^o$ (b) $\alpha = 20^o$ (c) $\alpha = 120^o$

(d) $\alpha = 10^o$ (e) $\alpha = 20^o$ (f) $\alpha = 120^o$

(g) $\alpha = 0^o$ (h) $\alpha = 30^o$ (i) $\alpha = 120^o$

Figure 5.1: Instantaneous pressure contours on the rear face of the plate at (a) $\alpha = 6^o$, (b) $\alpha = 20^o$, and (c) $\alpha = 120^o$ for Smagorinsky; at (d) $\alpha = 10^o$, (e) $\alpha = 20^o$, and (f) $\alpha = 120^o$ for iDDES; and at (g) $\alpha = 0^o$, (h) $\alpha = 30^o$, and (i) $\alpha = 120^o$ from Hargreaves et al. RANS solutions [27]

In Fig. 5.2 and Fig. 5.3 the formation of the leading and trailing edge vortices in the wake of the autorotating plate can be seen. At the initial time ($T = 0.5sec$) the plate is near vertical, Fig. 5.2(a), which creates strong tip vortices at both the leading and trailing edges, causing the plate to rotate. After 1 second the plate rotates an additional 90° allowing for vortex shedding

67

to occur and recirculate downstream, Fig. 5.2(b). At the same instant note that the tip vortex, that has shed from the bottom of the plate, collides with the bottom surface of the plate. As the vortex collides with the plate large pressure gradients are rapidly formed and then dissipated. These vortex-structure interactions are undoubtedly chaotic and are the root of instability and inconsistent behavior in autorotation. Notice that even at the last instance ($T = 3.5sec$), Fig. 5.2(g), the shed vortices have not travelled far downstream and still interact directly with the plates downstream pressure field. These vortex-blade interactions, [10], strongly couple turbulence closure models to the dynamic motion of the rigid body. This two-way interaction is the largest source of error in FSI, since the interacting turbulent eddies are never fully resolved. While Fig. 5.2 shows the results with the Smagorinsky turbulence model, Fig. 5.3 shows parallel flow visualization results using the iDDES turbulence model. Note that the faster run time of iDDES allows for greater simulation time compared to the Smagorinsky LES model.
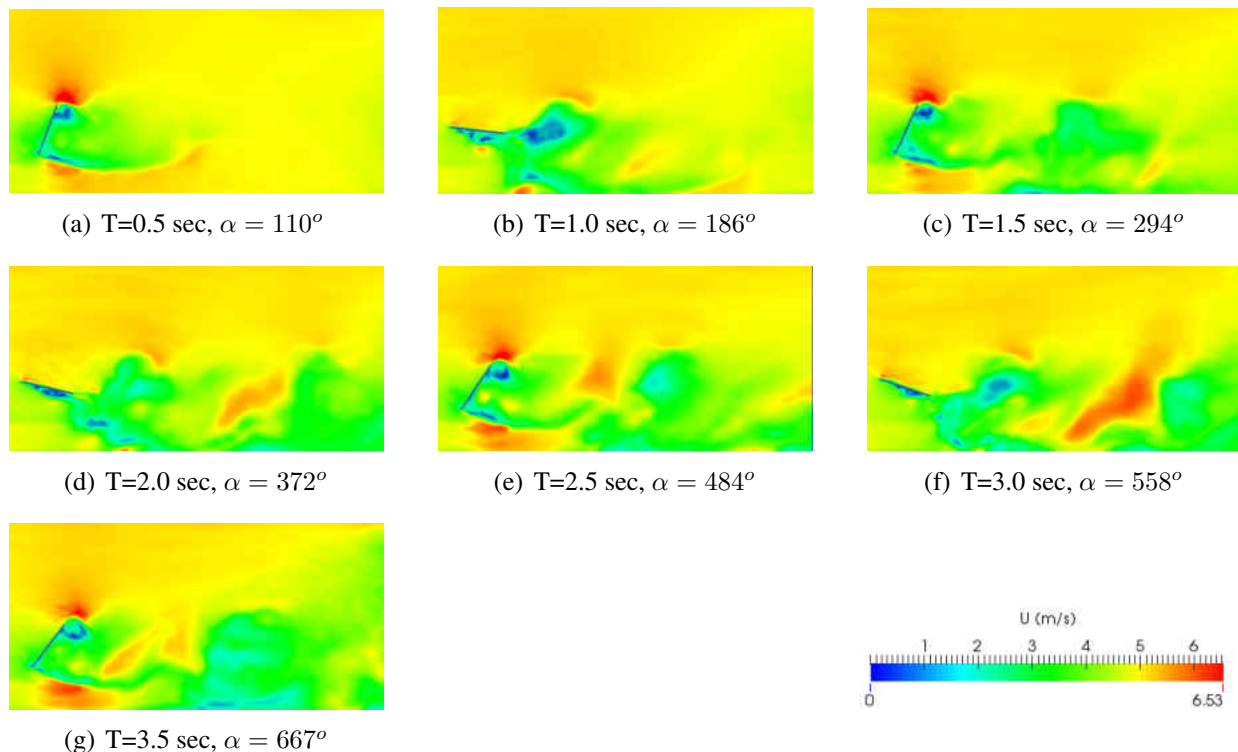

(a) T=0.5 sec, $\alpha = 110^o$ (b) T=1.0 sec, $\alpha = 186^o$ (c) T=1.5 sec, $\alpha = 294^o$

(d) T=2.0 sec, $\alpha = 372^o$ (e) T=2.5 sec, $\alpha = 484^o$ (f) T=3.0 sec, $\alpha = 558^o$

(g) T=3.5 sec, $\alpha = 667^o$

Figure 5.2: Instantaneous velocity contours on xy plane at different times and different angles of rotation for Smagorinsky

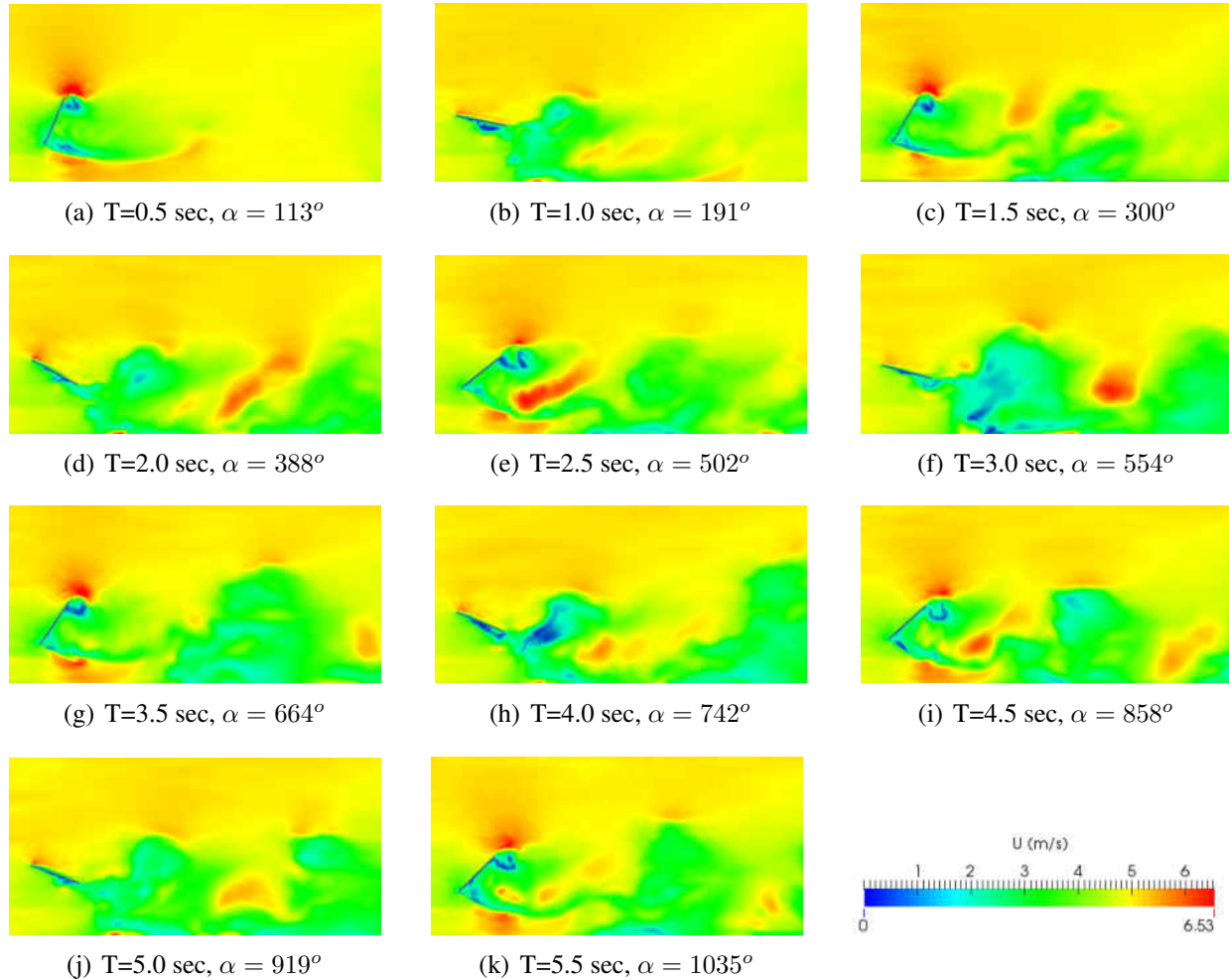(a) T=0.5 sec, $\alpha = 113^o$ (b) T=1.0 sec, $\alpha = 191^o$ (c) T=1.5 sec, $\alpha = 300^o$

(d) T=2.0 sec, $\alpha = 388^o$ (e) T=2.5 sec, $\alpha = 502^o$ (f) T=3.0 sec, $\alpha = 554^o$

(g) T=3.5 sec, $\alpha = 664^o$ (h) T=4.0 sec, $\alpha = 742^o$ (i) T=4.5 sec, $\alpha = 858^o$

(j) T=5.0 sec, $\alpha = 919^o$ (k) T=5.5 sec, $\alpha = 1035^o$

Figure 5.3: Instantaneous velocity contours on xy plane at different times and different angles of rotation for iDDES

5.2   Autorotating 3-Blade Rotor

Continuing from Section 4.2, this section presents further simulation results for the autorotating 3-blade rotor. Figure 5.4 shows the angular velocity versus time of the 3-blade rotor blade for angles of incidence of 40°, 45° and 50° with a free stream velocity of $5m/s$. These operating points correspond to conditions under which experimental data was collected. In all these simulations, the initial rotor speed was set to $198 rad/sec$ and all initial flapping angles where set to 0°. The initial rotor speed was chosen close to the steady rotational speed based on experimental data to

reduce the simulation time. Figure 5.4(a) shows the decelerating rotor as it approaches the steady rotational speeds of $150 rad/sec$ for 40°, $171.4 rad/sec$ for 45°, and $185.79 rad/sec$ for 50°. This is also evident in Fig. 5.4(b) which shows how the aerodynamic torque converges towards zero as the angular velocity tends to steady rotational conditions at each angle of incidence.
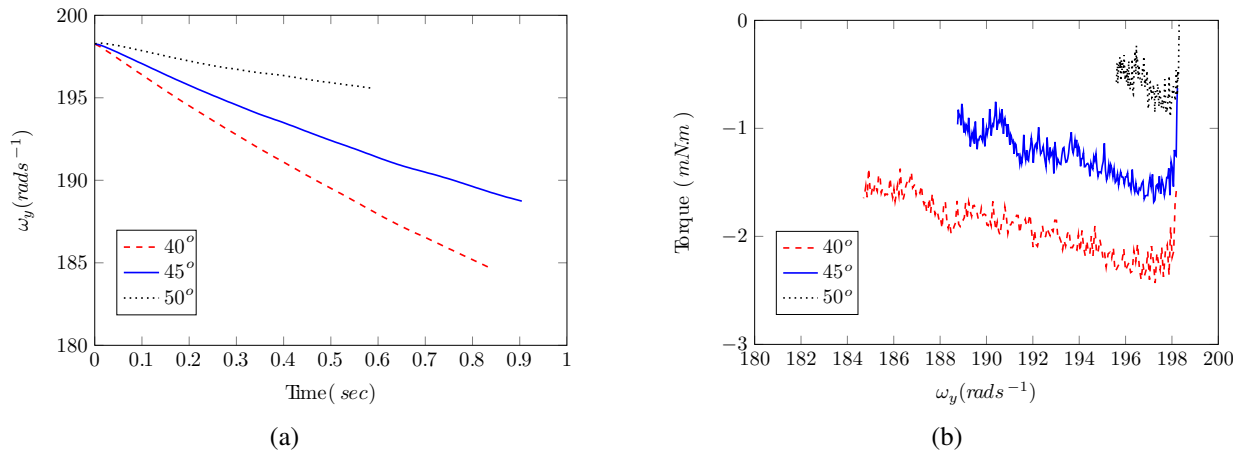

(a)   (b)

Figure 5.4: Angular velocity and torque at different angles of incidence for a free stream velocity of $5m/s$

Figure 5.5 shows the angular velocity versus time of the 3-blade rotor for angles of incidence of 30°, 40°, 45° and 50° under a free stream velocity of $10m/s$. The initial angular velocity was set to $301.7 rad/sec$ based on the approximation of the expected steady rotational speed in a free stream of $10m/s$. Figure 5.5(a) shows the acceleration of the rotor for incidence angles of 40°, 45°, and 50°, and deceleration of the rotor for 30°. Extensive simulations with different initial conditions give the following steady state rotational speeds for different angles of incidence: $238.3 rad/sec$ for 30°, $319.24 rad/sec$ for 40°, $357.76 rad/sec$ for 45°, and $388.06 rad/sec$ for 50°. Similar to Fig. 5.4(b), Fig. 5.5(b) demonstrates the rotor decelerating or accelerating as its torque converges towards zero signifying transition to steady state rotation.
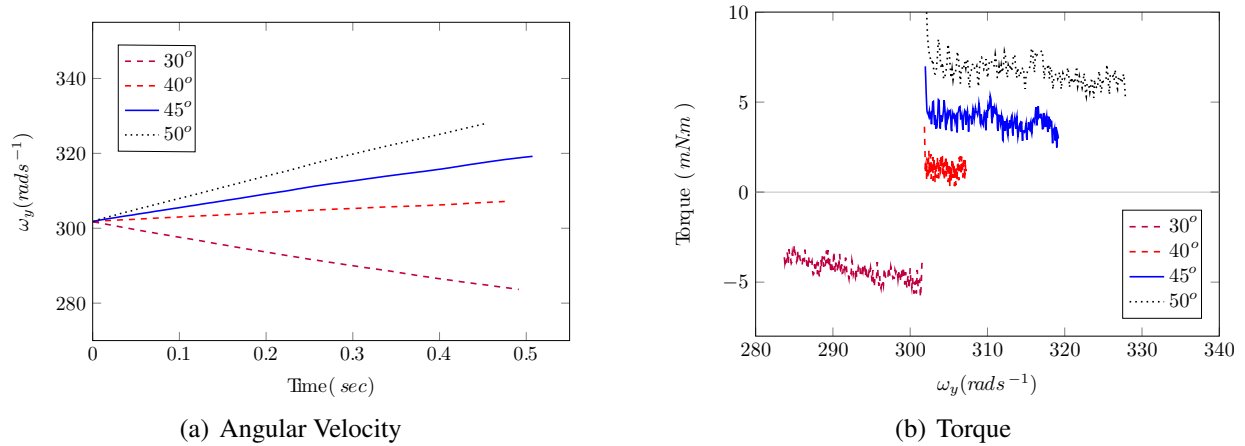
(a) Angular Velocity

(b) Torque

Figure 5.5: Angular velocity and torque at different angles of incidence for a free stream velocity of $10m/s$

Figure 5.6 and Fig. 5.7 present the instantaneous velocity contours in the xy plane for a rotor inclination of 40° with respect to the flow for a free stream of $5m/s$ and $10m/s$, respectively. The blades and hub are rotating clockwise about their common z-axis while being allowed to flap independently from each other about their local x-axis. Comparing the two figures it can be seen that speeding up the free stream incoming velocity in turn increases the disturbances in the flow past the rotor. In each of the visualization the phases of rotation are shown corresponding to each instant of time.

(a) T=0.1 sec, 139.3^o

(b) T=0.2 sec, 278.6^o

(c) T=0.3 sec, 57.96^o
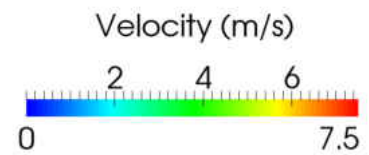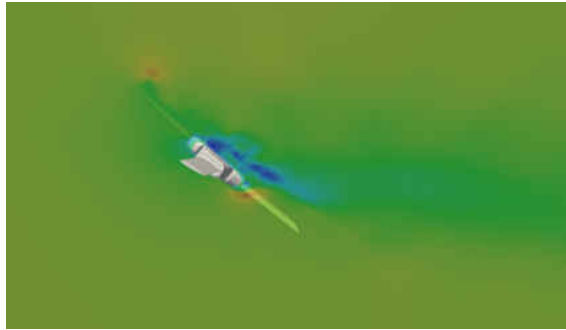

(d) T=0.4 sec, 197.3^o

(e) T=0.5 sec, 336.6^o
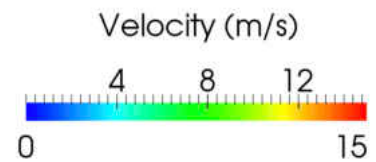
Figure 5.6: Instantaneous velocity contours at different times at a free stream velocity of $5m/s$ and at an angle of incidence of 40°

(a) T=0.1 sec, 29.12^o

(b) T=0.2 sec, 58.25^o

(c) T=0.3 sec, 97.0^o

(d) T=0.4 sec, 88.01^o

(e) T=0.5 sec, 190.0^o

Figure 5.7: Instantaneous velocity contours at different times at a free stream velocity of $10m/s$ and at an angle of incidence of 40°

In a similar fashion, Fig. 5.8 and Fig. 5.9 present the instantaneous velocity contours in the xy plane for a rotor inclination of 45° with respect to the flow for a free stream of $5m/s$ and $10m/s$, respectively. The increase in inclination of the rotor in turn increases the steady rotation velocity. Therefore, the rotor in Fig. 5.9 is rotating clockwise at a faster angular velocity than that in Fig. 5.7.
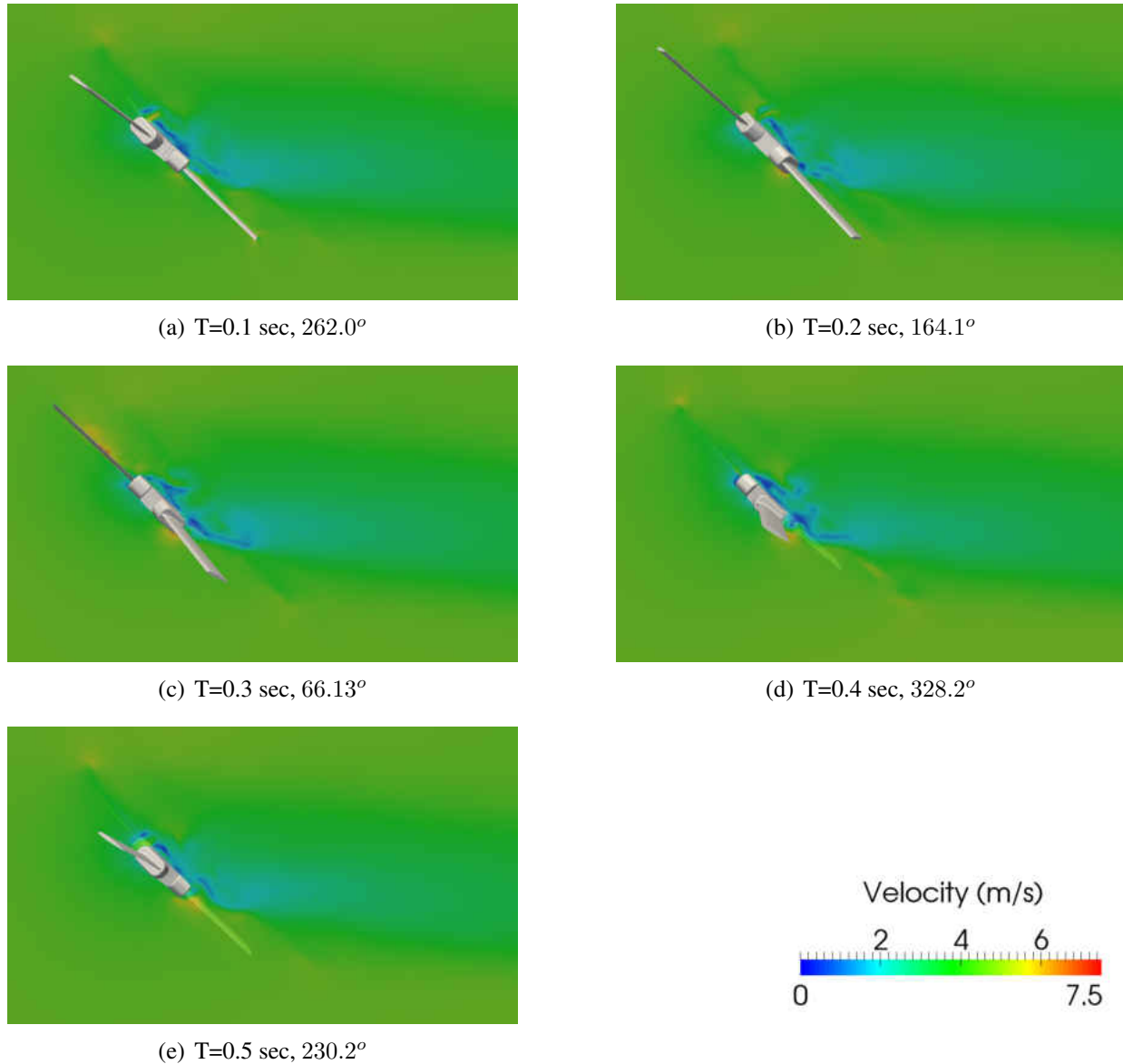

(a) T=0.1 sec, 262.0^o

(b) T=0.2 sec, 164.1^o

(c) T=0.3 sec, 66.13^o

(d) T=0.4 sec, 328.2^o

(e) T=0.5 sec, 230.2^o

Figure 5.8: Instantaneous velocity contours at different times at a free stream velocity of $5m/s$ and at an angle of incidence of 45°

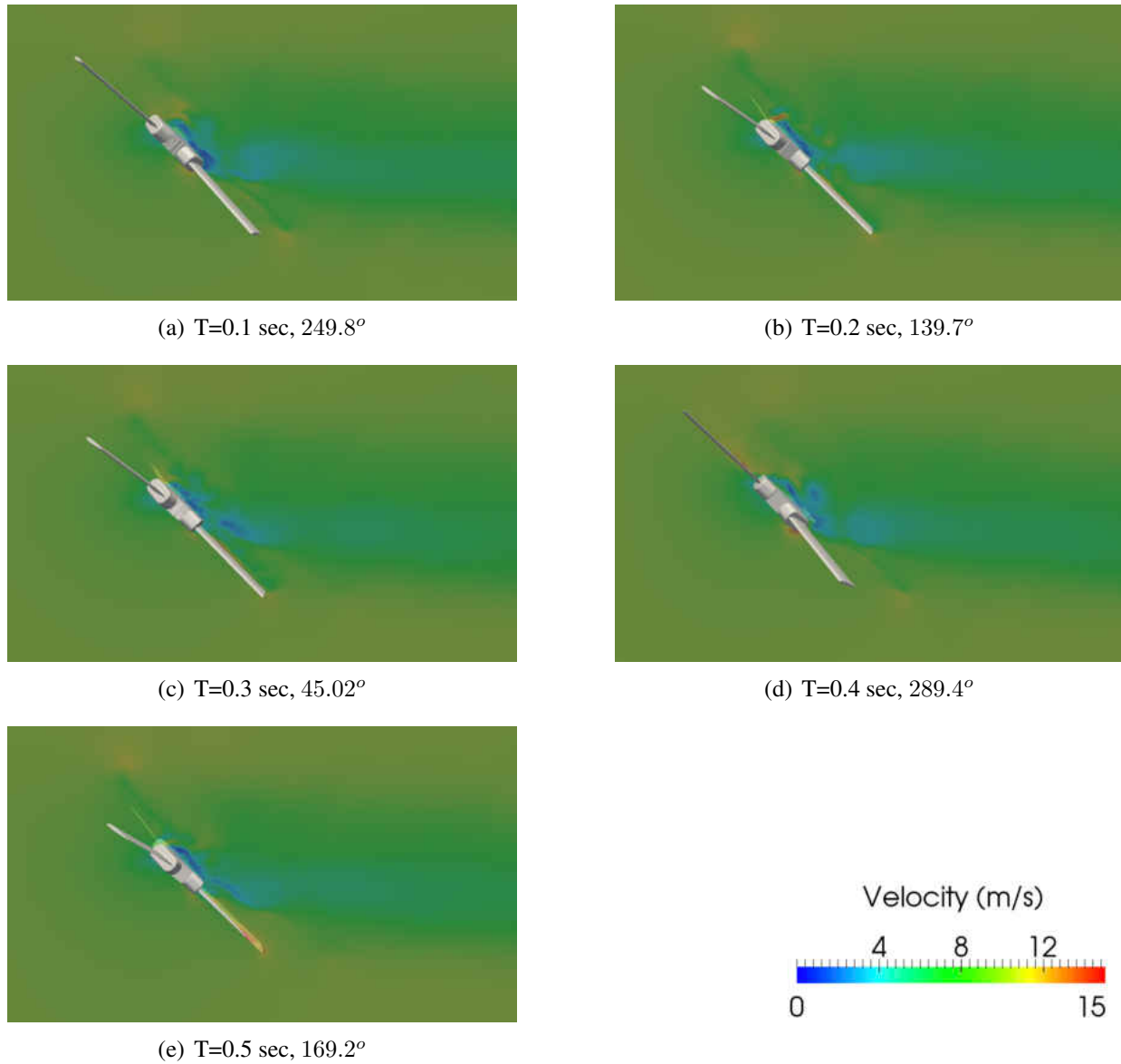(a) T=0.1 sec, 249.8^o

(b) T=0.2 sec, 139.7^o

(c) T=0.3 sec, 45.02^o

(d) T=0.4 sec, 289.4^o

(e) T=0.5 sec, 169.2^o
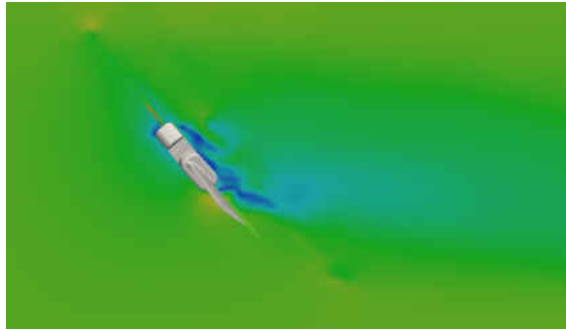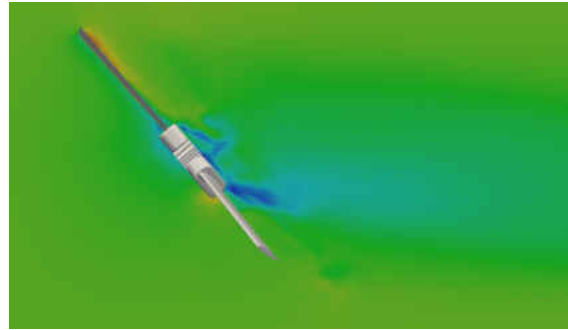
Figure 5.9: Instantaneous velocity contours at different times at a free stream velocity of $10m/s$ and at an angle of incidence of 45°

Similarly, Fig. 5.10 and Fig. 5.11 present the instantaneous velocity contours in the xy plane for a rotor inclination of 50° with respect to the flow for a free stream of $5m/s$ and $10m/s$, respectively. Once again the increase in inclination of the rotor increases the steady rotational speed.

(a) T=0.1 sec, 344.5^o
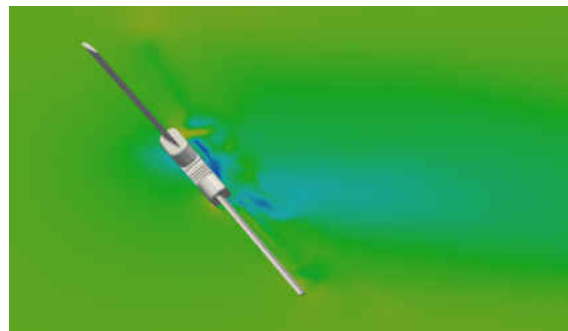
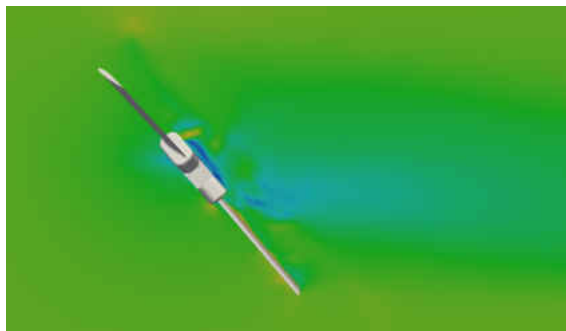(b) T=0.2 sec, 329.0^o

(c) T=0.3 sec, 313.6^o

(d) T=0.4 sec, 298.1^o

(e) T=0.5 sec, 282.6^o

Figure 5.10: Instantaneous velocity contours at different times at a free stream velocity of $5m/s$ and at an angle of incidence of 50°

(a) T=0.1 sec, 23.36^o

(b) T=0.2 sec, 126.7^o

(c) T=0.3 sec, 190.1^o

(d) T=0.4 sec, 253.4^o

(e) T=0.5 sec, 30.02^o

Figure 5.11: Instantaneous velocity contours at different times at a free stream velocity of $10 m/s$ and at an angle of incidence of 50°

In Fig 5.12, gives flow visualizations for direct comparison between different angles of incidence. Specifically, Fig 5.12(a) and (c), depict the downstream flow velocities for a 40° angle of incidence, while Fig 5.12(b) and (d), show the same for a 50° angle of incidence. As expected, the general observation is that for lower angles of incidence the flow deceleration is lesser in magnitude and area.

(a) $\theta = 40^o$, T=0.3 sec, 57.96^o

(b) $\theta = 50^o$, T=0.3 sec, 313.6^o

(c) $\theta = 40^o$, T=0.5 sec, 336.6^o

(d) $\theta = 50^o$, T=0.5 sec, 282.6^o
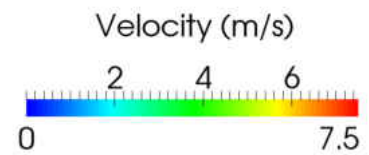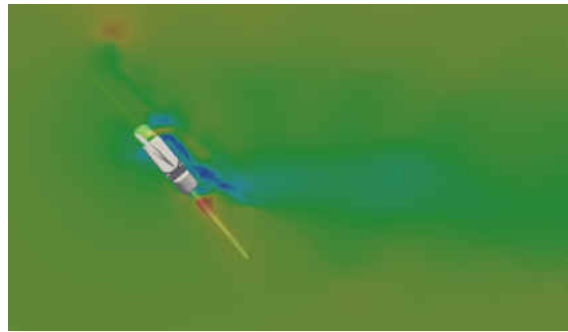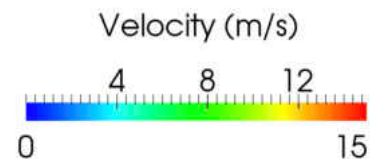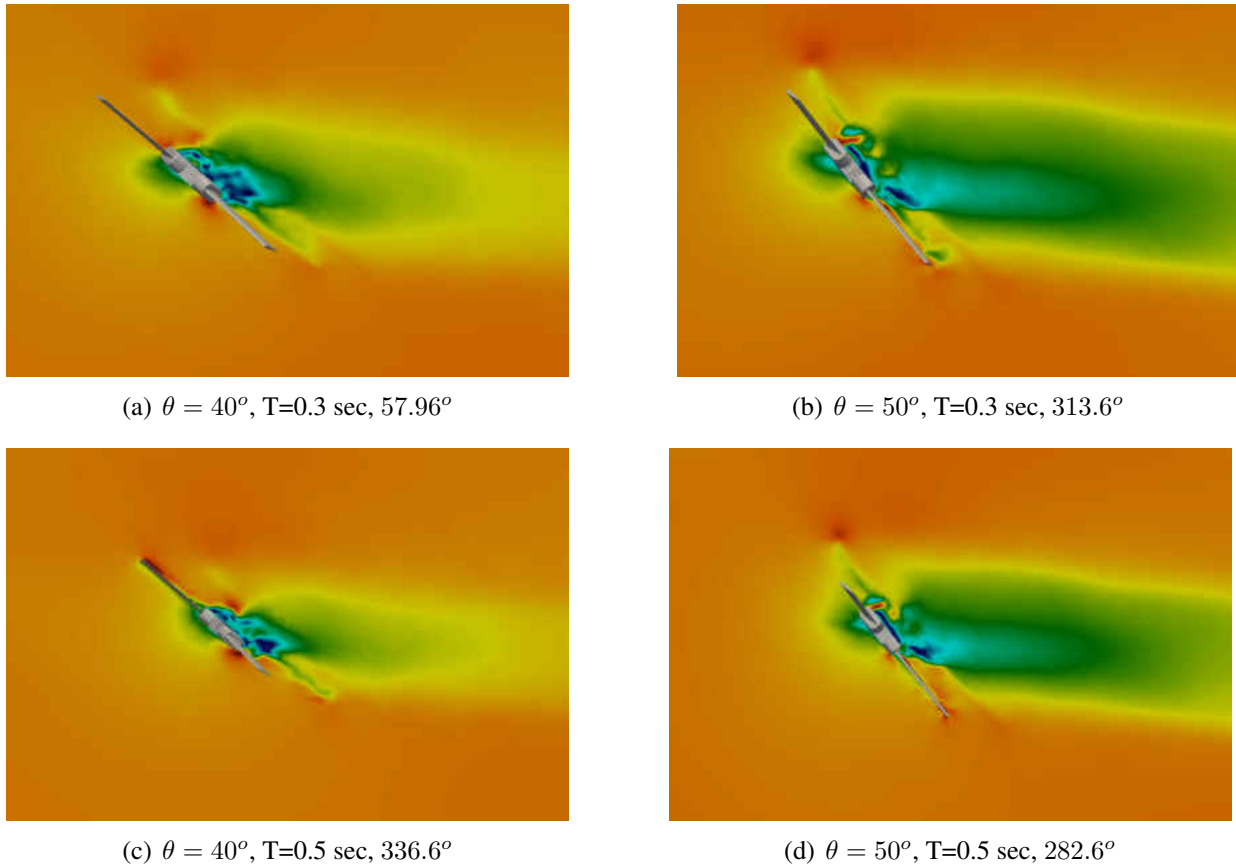
Figure 5.12: Instantaneous velocity contours at different times at a free stream velocity of $5m/s$ and at angle of incidence of 40° and 50°

Next simulation results showing the flapping of the individual blades are provided. Each blade is free to rotate about its local x-axis along a hinge attached to the hub of the rotor. Figure 5.13 shows the comparison of the flapping angles of the three blades at a free stream velocity of $5m/s$ at different angles of incidence with respect to the air flow. At the beginning of the simulation, the amplitude of flapping is the largest and with time, as the simulation reaches a steady rotational

state, the amplitude of flapping diminishes. Figures 5.13(a), (b), and (c) show the flapping angles at three different angels of incidence, 40°, 45°, and 50° . With the increase of the angle of incidence of the rotor, the magnitude of flapping also increases. This is clearer when comparing the maxima between Fig. 5.13(a) and (c). Between these two figures the rotor's inclination has a 10° difference and therefore the increase in flapping is more noticeable.

While in Fig. 5.13 the free stream velocity is kept constant to see the effect that the angle of incidence has on the blade flapping, in Fig. 5.14 the angle of incidence is kept constant at 40° while the velocity of the air flow is varied. From this figure, it is clear that the flapping frequency is directly influenced by the rotor's angular speed. This is a result of the increase of steady angular velocity from $150 rad/s$ to $319 rad/sec$ when increasing the free stream velocity increases from $5m/s$ to $10m/s$ at the inclination of 40°.

(a) 40°

(b) 45°

(c) 50°
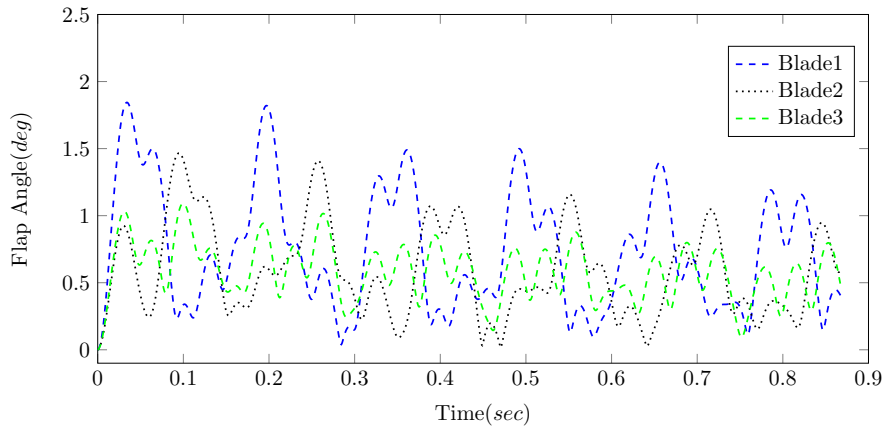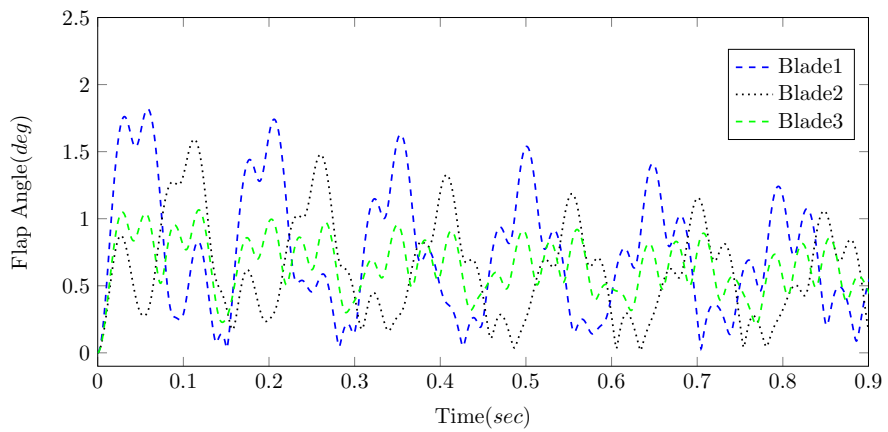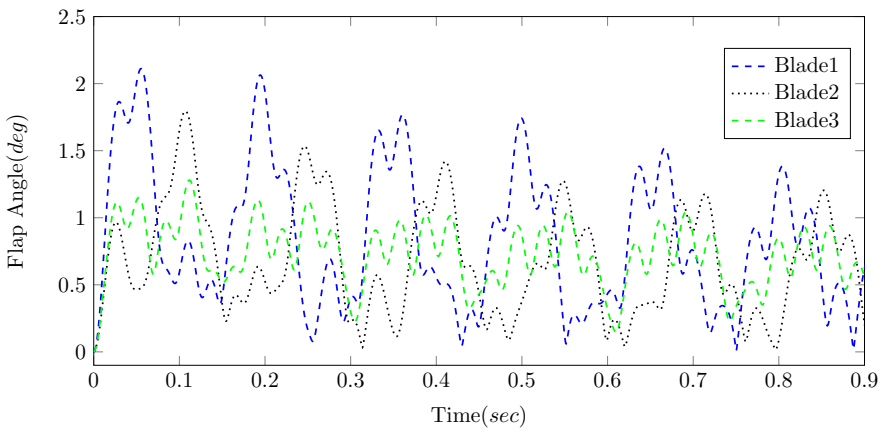
Figure 5.13: Comparison of blade flapping angle for a free stream velocity of $5m/s$ at different flow inclinations
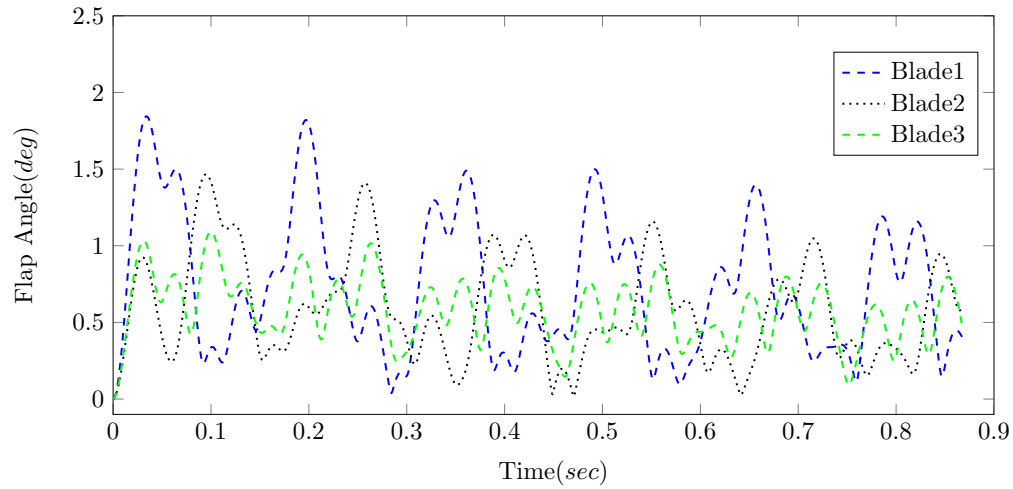
(a) $V_\infty = 5m/s$
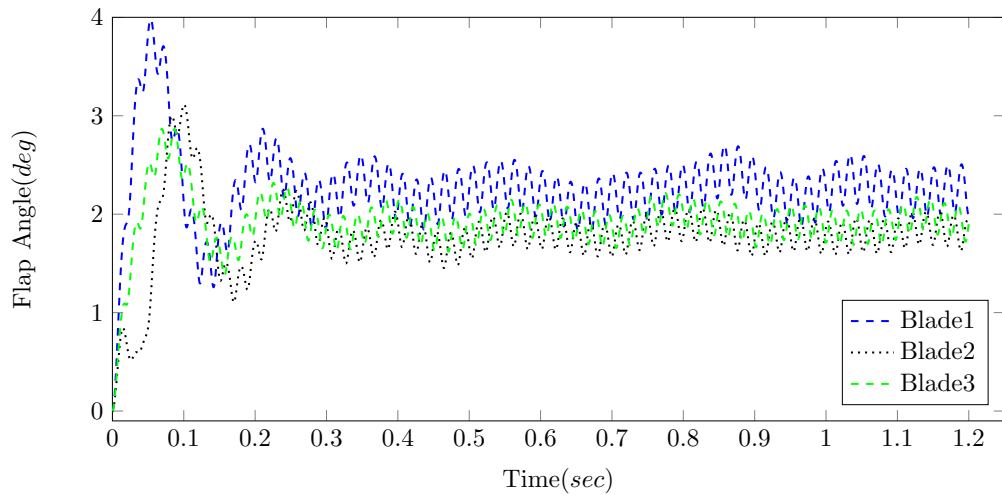
(b) $V_\infty = 10m/s$

Figure 5.14: Comparison of blade flapping angle for the rotor subject to a free stream velocity of $5m/s$ and $10m/s$ at an angle of 40°

To compare the characteristics of flapping of each blade, the simulated flapping angles at different free stream velocities are superimposed in Fig. 5.15. Figures 5.15(a), (b), and (c) superimpose the transient flapping angles of blades 1, 2 and 3, respectively. The comparison of of flapping angles are done at air stream velocities of $5m/s$ and $10m/s$ with a fixed angle of incidence of 40°. From this it can be seen that doubling the velocity of the air flow, while keeping the inclination of the rotor with respect to the flow unchanged, causes both the frequency and the average angles

of inclination to increase. However, even though the overall magnitude of the flapping angle is larger for larger flow speeds, the amplitude of oscillation reduces and the blade's flapping becomes smaller. Therefore it can be concluded that an increase in angular velocity results in an increase in flapping frequency and a decrease in amplitude. This reduction in amplitude at high air speeds is expected since higher rotational speeds cause the centrifugal force on each blade to become more dominant than the flapping torque.

Finally, Fig. 5.16 shows a zoomed in view of the flapping of the three blades at incidence angle of 40° and free stream velocity of $10m/s$. From the plot, the approximated rotational speed is obtained as 4 cycles per 0.08 seconds. This approximates to $50Hz = 314rad/sec$ which matches closely with the steady state rotational speed of $319.24rad/sec$ obtained from simulations in Section 4.2.3. For the $5m/s$ free stream velocity, similar approximation from Fig. 5.15(c) yields 9 cycles per 0.4 seconds. This approximates to $22.5Hz = 141rad/sec$ which matches closely with the steady state rotational speed of $150rad/sec$, as shown in Fig. 4.13(a).

Figure 5.17 and Fig. 5.18 show the instantaneous velocity contours at the xz plane at the surface of the rotor disk inclined at 40° with respect to the flow for a free stream velocity of $5m/s$ and $10m/s$, respectively. The visualization plots show the magnitude of the resultant flow field velocity over the are around the rotor. For the time interval of $T = 0.1sec$ between each of the figures, the rotor subject to the $5m/s$ free stream velocity completes about 2.4 revolutions in a clockwise direction, while when subject to a velocity of $10m/s$, with the same inclination angle, rotates clockwise about 5.1 times. In Fig. 5.18 the flapping of the blades is more clearly evident as not all the blade surfaces are fully visible seen in the current plane, signifying that the blades are flapping at different rates and independently from each other. Note that between Fig. 5.17 and Fig. 5.18 there is a significant difference in the scale of the flow velocities. This is due to the different free stream velocities, $5m/s$ in Fig. 5.17 and $10m/s$ in Fig. 5.18.

(a) Blade1

(b) Blade2
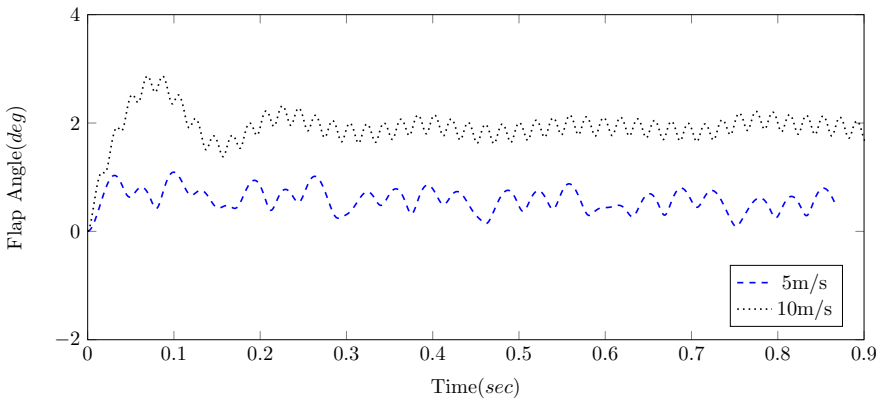
(c) Blade3

Figure 5.15: Comparison of blade flapping angle for each rotor blade subject to a free stream velocity of $5m/s$ and $10m/s$ at an angle of 40°
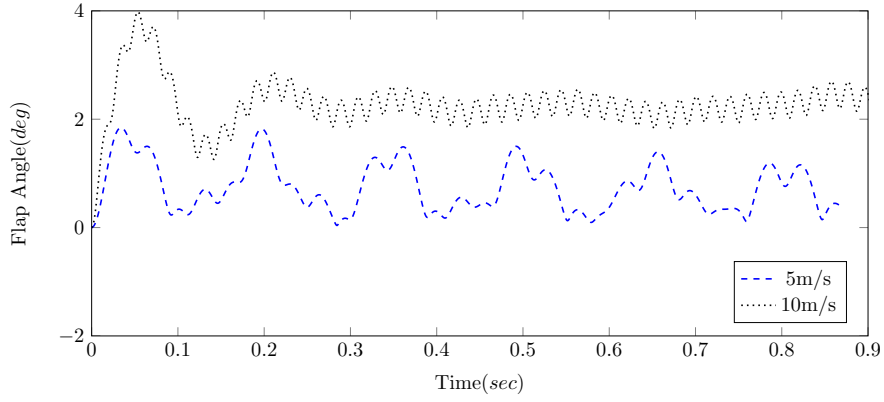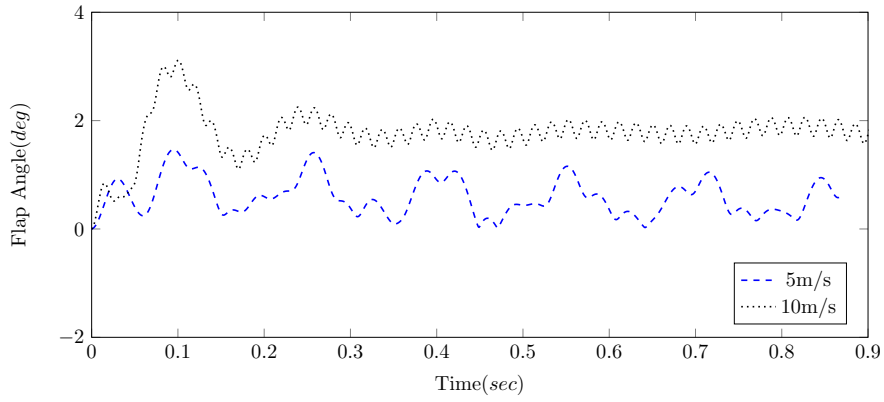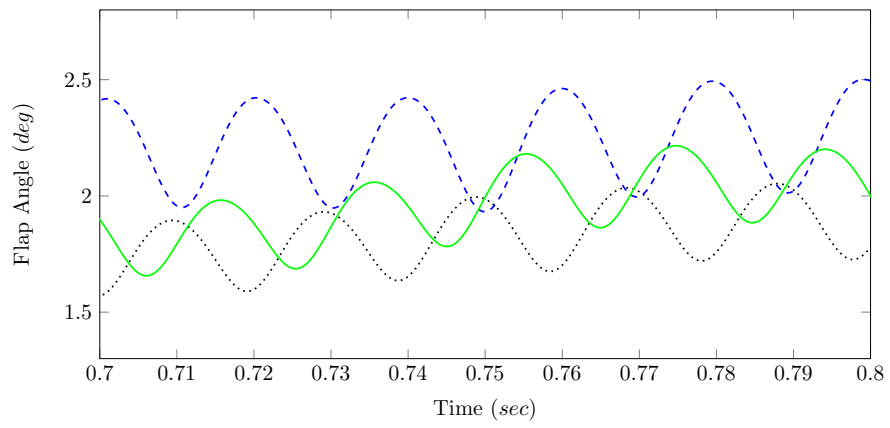
Figure 5.16: Comparison of blade flapping angle for each rotor blade subject to a free stream velocity of $10m/s$ at an angle of 40°

(a) T=0.4 sec

(b) T=0.5 sec

(c) T=0.6 sec

(d) T=0.7 sec

(e) T=0.8 sec
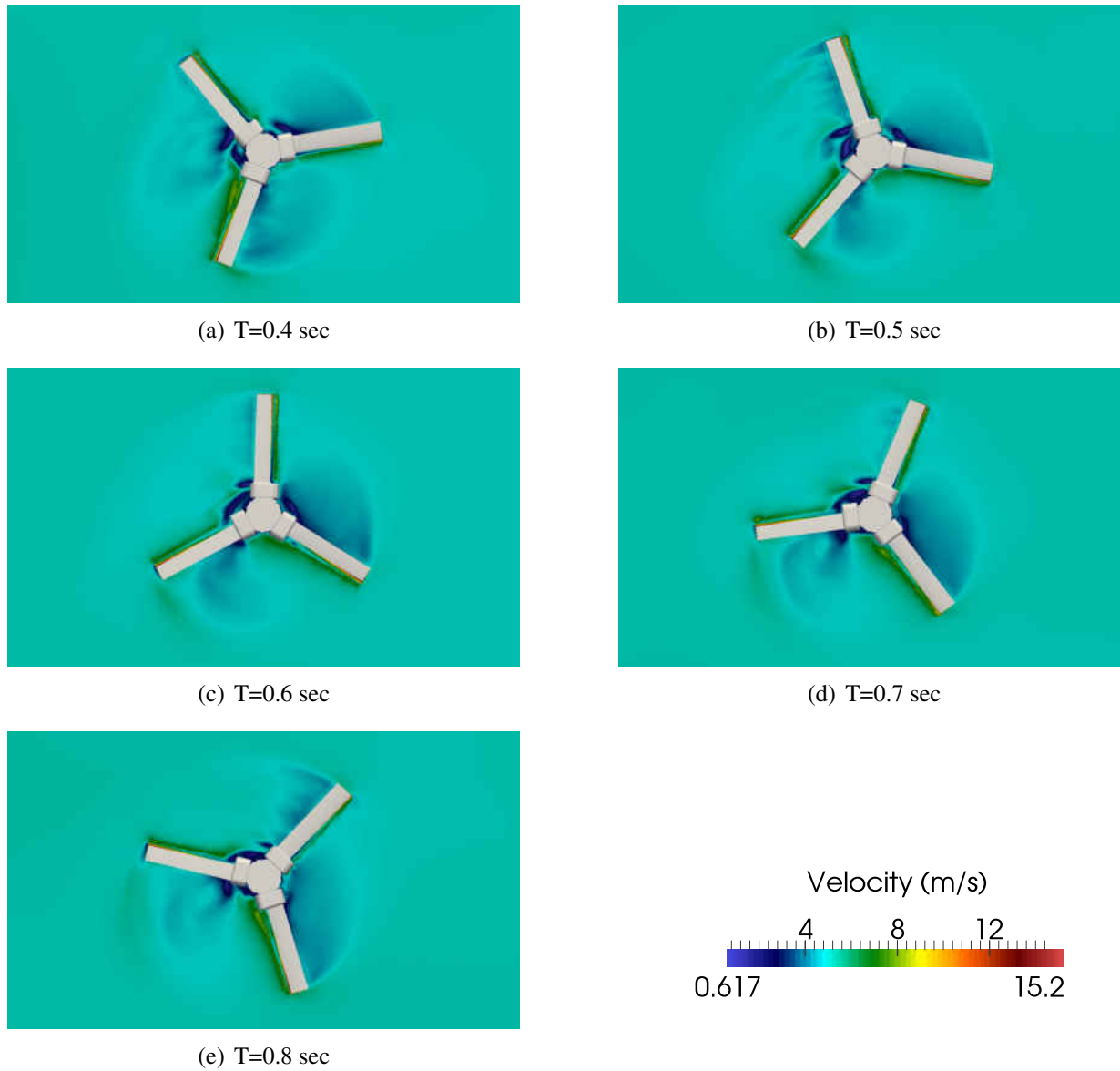
Figure 5.17: Instantaneous velocity contours at xz plane at different times at a free stream velocity of $5m/s$ and at an angle of 40°

(a) T=0.7 sec

(b) T=0.8 sec

(c) T=0.9 sec

(d) T=1.0 sec

(e) T=1.1 sec
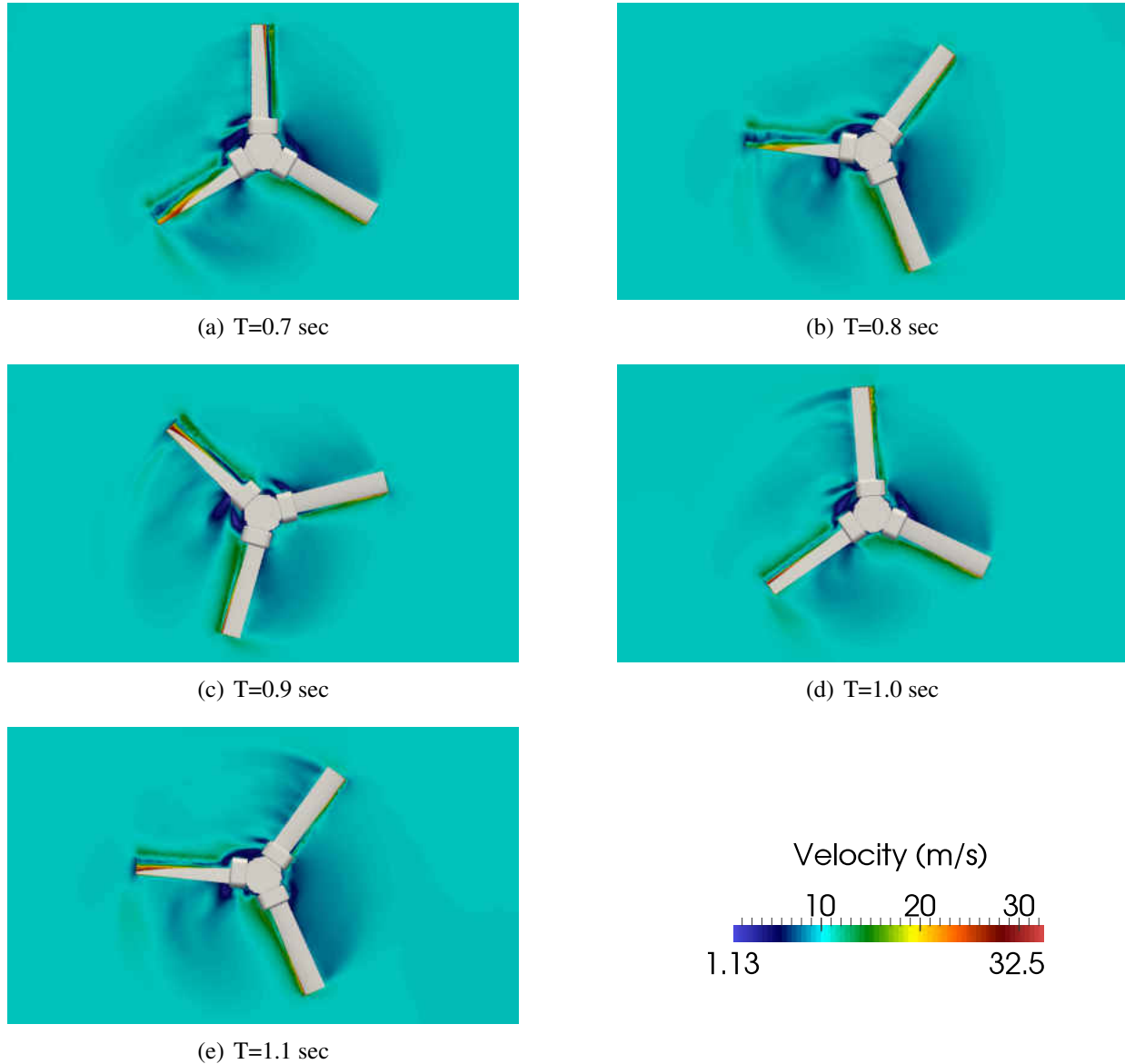
Figure 5.18: Instantaneous velocity contours at xz plane at different times at a free stream velocity of $10m/s$ and at an angle of 40°

Figures 5.19, 5.20, and 5.21, provide further visualization of the flow due to the interaction with the 3-blade rotor. In these figures, the emphasis is on visualizing the flow vorticity generated by the fluid structure interaction. Figure 5.19 shows the instantaneous streamlines at an angle of incidence of 40°. The streamlines show the turbulence generated by the interaction of the fluid with the solid blades. While Fig. 5.19 shows a collection of streamlines, Fig. 5.20 isolates one of the streamlines

to show the vortex shedding from the trailing edge of a blade as it rotates in a free stream velocity of $10m/s$ at 40° inclination. Figure 5.21 presents the instantaneous vorticity isosurfaces for the same case. In Fig. 5.21, the volume around the rotor shows higher vorticity strengths near the surface of the rotor, which diminishes further downstream. Similar observation can be made from the color code of the streamline in Fig. 5.20. In regions closer to the blade, the color code indicates higher vorticity.

Figure 5.19: Instantaneous streamlines at a free stream velocity of $10m/s$ and at an angle of 40°

Figure 5.20: Vortex shedding from trailing edge at a free stream velocity of $10m/s$ and at an angle of 40°
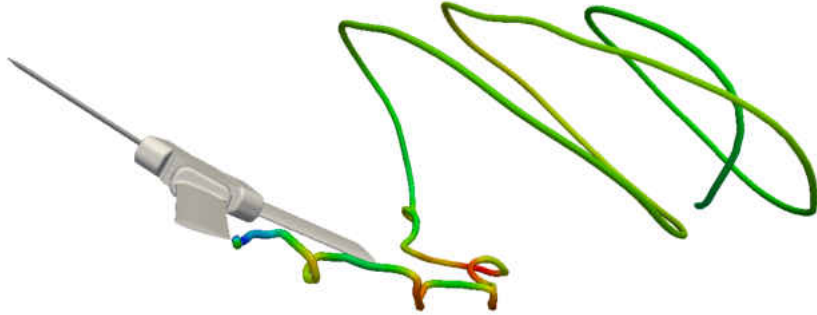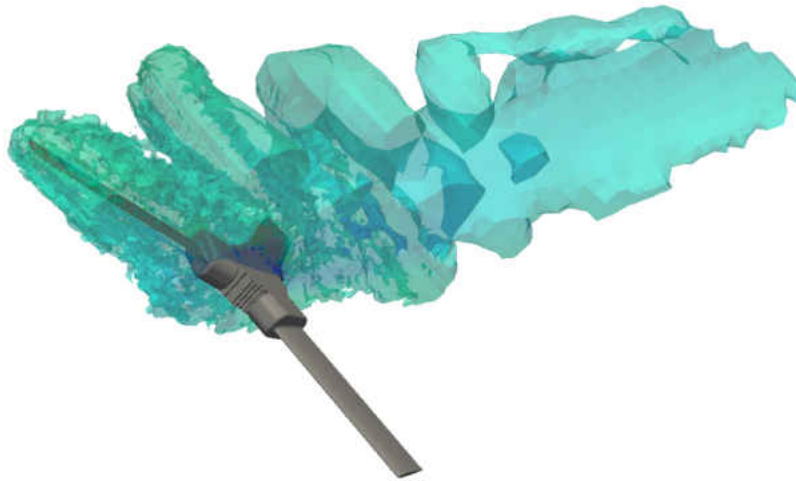

Figure 5.21: Instantaneous vorticity isosurfaces at a free stream velocity of $10m/s$ and at an angle of 40°

CHAPTER 6: CONCLUSION

The goal of this work is to develop a computational platform for simulating large-scale fluid structure interactions (FSI) by combining rigid body dynamics with CFD. The simulation environment was implemented in OpenFOAM, which is an open-source object-oriented CFD toolbox which allows customized augmentations and modifications. The models introduced in this work incorporate mesh morphing techniques to account for the large-scale fluid-induced motion while using a numerically stable computational scheme.

First a combined CFD and rigid body dynamics (RBD) model is developed to simulate an autorotating square flat plate, subject to a free-stream air velocity. Two Smagorinsky LES models are compared to two Hybrid LES models to predict the resulting autorotating motion. The computational results agree well with experimental data obtained from [47]. Specifically, the qualitative prediction of vortex structures, as well as the quantitative computation of pressure coefficients at the plate's surface agree well with experiments. The work also shows better agreement with experiments compared to RANS results previously found in literature [27]. The reason is attributed to LES being able to resolve the small flow structures that RANS is unable to compute. Hybrid models, such as DDES and iDDES, were shown to save computational time compared to pure LES and have been found to be an effective alternative in such CFD-RBD simulations. Despite the close correlation of simulation results with the experiments, there were over-estimation in the coefficients of lift and drag. While certain reasons for this discrepancy are apparent, further research is needed to resolve this issue.

Subsequently, a high resolution fully coupled CFD and multi-body dynamics (MBD) model is developed to study the complex FSI interactions of an autorotating 3-blade rotor subject to a flow field at various inclination angles. The hybrid LES turbulence model, iDDES, is employed since it demonstrated a reduction in computation time in the preliminary study with the rotating square flat plate. The computational results show agreement with experimental data gathered as part of

this research. The experimental setup consisted of a mechatronics system with appropriate data acquisition to generate motion data under various operating conditions. Computational results for the angular velocity and aerodynamic torque of the rotor subject at different wind speeds and varying angles of incidences agree well with the values gathered from the experiments. Additionally, the model is capable of capturing and visualizing the vortex shedding from the trailing edge of the rotating blades, as well as predict the flapping motion of each blade with reasonable accuracy. One challenge with the simulations is the rather long clock-time needed for small simulation times. This puts restrictions in simulating transients in their entirety.

The results of this work show promise in the ability of LES and hybrid LES models to predict the complex FSI found in autorotation or similar other applications involving large-scale FSI. The platform introduced in this dissertation can be used for the study of FSI problems involving various large fluid-flow induced motion. Some applications could be falling objects, oceanographic flow fields and rotating machines, amongst others.

List of Journal and Conference Papers Published/in Preparation

1. Large-Eddy Simulations of an Autorotating Square Flat Plate. Applied Mathematical Modelling. 2016. (In Press)

2. Multi-body CFD model development for the investigation of an autorotating 3-blade rotor: Large-Eddy Simulations. Journal of Fluids and Structures. 2016. (In preparation)

3. Numerical Study of Helicopter Blade-Vortex Interaction Using the Potential Flow Theory. Applied Mathematical Modelling, 36(7). (2012): 2841-2857.

4. Rotorcraft Blade-Vortex Street Interactions; Critical Aerodynamic Aspects. 51st AIAA Aerospace Sciences Meeting. AIAA-2013-0805

5. Reduction of Helicopter BVI Noise Using Active Flow Control; the Case of Vortex Street Interactions. 29th AIAA Applied Aerodynamics Conference. AIAA-2011-3356

6. Numerical Investigations of Vortex-Cylinder Mechanism of Interaction Using LES and URANS. 49th AIAA Aerospace Sciences Meeting. AIAA-2011-57

7. High Angle of Attack Helicopter Blade-Vortex Interaction; Numerical Studies Using LES. 49th AIAA Aerospace Sciences Meeting. AIAA-2011-55

LIST OF REFERENCES

[1] P.R. Andronov, D.A. Grigorenko, S.V. Guvernyuk, and G.Ya. Dynnikova. Numerical simulation of plate autorotation in a viscous fluid flow. *Fluid Dynamics*, 42(5):719–731, 2007.

[2] C.D. Argyropoulos and N.C. Markatos. Recent advances on the numerical modelling of turbulent flows. *Applied Mathematical Modelling*, 39(2):693–732, 2015.

[3] K.Y. Billah and R.H. Scanlan. Resonance, Tacoma Narrows bridge failure and undergraduate physics textbooks. *American Journal of Physics*, 59(2):118–124, February 1991.

[4] J. Boris. More for LES: A brief historical perspective of MILES. *Implicit Large Eddy Simulation*, Cambridge University Press:9–38, 2007.

[5] J. Boris, F. Grinstein, E. Oran, and R. Kolbe. New insights into large eddy simulation. *Fluid Dynamics Research*, 10(4-6):199–228, 1992.

[6] J. P. Boris. On large eddy simulation using subgrid turbulence models. In J.L. Lumley, editor, *Whither Turbulence? Turbulence at the Crossroads*, volume 357 of *Lecture Notes in Physics*, pages 344–353. Springer-Verlag, 1990.

[7] C.A. Brebbia and G.R. Rodriguez, editors. *Fluid Structure Interaction VII*. WIT Press, 2013.

[8] M. Breuer, G. De Nayer, M. Munsch, T. Gallinger, and R. Wuchner. Fluid-structure interaction using a partitioned semi-implicit predictor-corrector scheme for the application of large-eddy simulation. *Journal of Fluids and Structures*, 29:107–130, 2012.

[9] V. Carstens, R. Kemme, and S. Schmitt. Coupled simulation of flow-structure interaction in turbumachinery. *Aerospace Science and Technology*, 7:298–306, 2003.

[10] P. Coronado, C. Velez, and M. Ilie. Rotorcraft blade-vortex street interactions; critical aerodynamic aspects. In *51st AIAA Aerospace Sciences Meeting*, 2013.

[11] P. X. Coronado Domenge, C.A. Velez, and T. Das. Large-eddy simulations of an autorotating square flat plate. *Applied Mathematical Modelling*, 2016.

[12] P. X. Coronado Domenge, B. Wang, and G.-C. Zha. Delayed-detached-eddy simulation of shock wave/turbulent boundary layer interaction. In *48th AIAA Aerospace Sciences Meeting*, number AIAA 2010-109, January 2010.

[13] J. Deardorff. A numerical study of three dimensional turbulent channel flow at large Reynolds numbers. *Journal of Fluid Mechanics*, 41:453–480, 1970.

[14] G. Duan and B. Chen. Large eddy simulation by particle method coupled with sub-particle-scale model and application to mixing layer flow. *Applied Mathematical Modelling*, DOI: 10.1016/j.apm.2014.10.058, 2014.

[15] A. Dullweber, B. Leimkuhler, and R. McLachlan. Symplectic splitting methods for rigid body molecular dynamics. *Journal of Chemical Physics*, 107(15):5840–5851, 1997.

[16] S. Eisenback and R. Friedrich. Large-eddy simulation of flow separation on an airfoil at a high angle of attack and Re=10^5 using cartersian grids. *Theoretical and Computational Fluid Dynamics*, 22:213–225, May 2008.

[17] G. Erlebacker, M.Y. Hussaini, C.G. Speziale, and T.A. Zang. Toward the large eddy simulation of compressible turbulent flows. *Journal of Fluid Mechanics*, 238:155–185, 1992.

[18] A. Fabre. Equations des gaz turbulents compressibles. *Journal de Mecanique*, 4:361–390, 1954.

[19] P.E. Farrell and J.R. Maddison. Conservative interpolation between volume meshes by local galerkin projection. *Computer Methods in Applied Mechanics and Engineering*, 200(1-4):89–100, January 2011.

[20] A. Feymark. *A large eddy simulation based fluid-structure interaction methodology with application in hydroelasticity*. PhD thesis, Chalmers University of Technology, 2013.

[21] M. Germano, U. Piomelli, P. Moin, and W. H. Cabot. A dynamic subgrid-scale eddy viscosity model. *Physics of Fluids A*, 3:1760–1765, 1991.

[22] A. Gessow and A.D. Crim. An extension of lifting rotor theory to cover operations at large angles of attach and high inflow conditions. *National Advisory Committee for Aeronautics*, Technical Note No. 2665, 1952.

[23] H. Glauert. A general theory of the autogyro. *Presented by the Director of Scientific Research Air Ministry, Reports and Memoranda No. 1111*, (Ae. 285), 1926.

[24] V. Gnesin and R. Rzadkowski. A coupled fluid-structure analysis for 3-D inviscid flutter of IV standard configuration. *Journal of Sound and Vibration*, 251:315–327, 2002.

[25] F.F. Grinstein and C.R. DeVore. Dynamics of coherent structures and transition to turbulence in free square jets. *Physics of Fluids*, 8(5):1237–1251, 1996.

[26] R. P. Hansen and J.R. Forsythe. Large and detached eddy simulation of a circular cylinder using unstructured grids. In *41st Aerospace Sciences Meeting and Exhibit*, 2003.

[27] D.M. Hargreaves, B. Kakimpa, and J.S. Owen. The computationl fluid dynamics modelling of the autorotation of square, flat plates. *Journal of Fluids and Structures*, 46:111–133, 2014.

[28] Zongjun Hu. Parallel Computation of Fluid-Structure Interaction Using High Resolution Upwind Schemes. Ph.D. Thesis, University of Miami, May 2005.

[29] H-S. Im and G-C Zha. Investigation of flow instability mechanism causing compressor rotor-blade nonsynchronous vibration. *AIAA Journal*, 52(9):2019–2031, 2014.

[30] H-S Im, G-C Zha, and B.P.E. Dano. Large eddy simulation of coflow jet airfoil at high angle of attack. *Journal of Fluids Engineering*, 136(2):1–10, February 2014.

[31] R.I. Issa. Solution of the implicitly discretised fluid flow equations by operator-splitting. *Journal of Computational Physics*, 62(1):40–65, 1986.

[32] J. Janicka and A. Sadiki. Large eddy simulation of turbulent combustion systems. *Proceeding of the Combustion Institute*, 30(1):537–547, 2005.

[33] H. Jasak, A. Jemcov, and A. Tukovic. OpenFOAM: A C++ library for complex physics simulations. In *International Workshop on Coupled Methods in Numerical Dynamics IUC, Dubrovnik, Croatia*, 2007.

[34] B. Kakimpa, D.M. Hargreaves, and J.S. Owen. An investigation of plate-type windborne debris flight using coupled CFD-RBD models. Part I: model development and validation. *Journal of Wind Engineering and Industrial Aerodynamics*, 111:95–103, 2012.

[35] B. Kakimpa, D.M. Hargreaves, J.S. Owen, P. Martinez-Vazquez, C.J. Baker, M. Sterling, and A.D. Quinn. CFD modelling of free-flight and auto-rotation of plate type debris. *Wind and Structures*, 13(2):169–189, 2010.

[36] R. Kamakoti and W. Shyy. Fluid-structure interaction of aeroelastic applications. *Progress in Aerospace Sciences*, 40:535–558, 2004.

[37] T. Kawamura, H. Takami, and K. Kuwahara. Computation of high Reynolds number flow around a circular cylinder with surface roughness. *Fluid Dynamics Research*, 1(2):145–162, 1986.

[38] S. J. Lee, E. J. Lee, and M. H. Sohn. Mechanism of autorotation flight of maple samaras. *Experiments in Fluids*, 55(1718), 2014.

[39] J. G. Leishman. Development of the autogyro: A technical perspective. *Journal of Aircraft*, 41(4):765–781, 2004.

[40] D. Lentink, W.B. Dickson, J.L. Leeuwen, and M.H. Dickinson. Leading-edge vortices elevate lift of autorotating plant seeds. *Science*, 324:1438–1440, 2009.

[41] E. Lévêque, F. Toschi, L. Shao, and J.-P. Bertoglio. Shear-improved Smagorinsky model for large-eddy simulation of wall-bounded turbulent flows. *Journal of Fluid Mechanics*, 570:491–502, 2007.

[42] C. Li, S. Zhu, Y-L Xu, and Y. Xiao. 2.5D large eddy simulation of vertical axis wind turbine in consideration of high angle of attack flow. *Renewable Energy*, 51:317–330, 2013.

[43] K. Li, L.X. Zhou, C.K. Chan, and H.G. Wang. Large-eddy simulation of ethanol spray combustion using SOM combustion model and its experimental validation. *Applied Mathematical Modelling*, 39(1):36–49, 2015.

[44] D.K. Lilly. The presentation of small-scale turbulent in numerical simulation experiments. *IBM Scientific Computing Symp. on Environmental Sciences*, page 195, 1967.

[45] C.N.H. Lock. Further development of autogyro theory - Part I and II. *Presented by the Director of Scientific Research Air Ministry, Reports and Memoranda No. 1127*, (Ae. 299), 1928.

[46] D. A. Lysenko, I. S. Ertesvåg, and Rian K. E. Large-eddy simulation of the flow over a circular cylinder at Reynolds number 3900 using the OpenFOAM toolbox. *Flow, Turbulence and Combustion*, 89(4):491–518, 2012.

[47] P. Martinez-Vazquez, C.J. Baker, M. Sterling, A.D. Quinn, and P.J. Richards. The flight of wind borne debris: An experimental, analytical and numerical investigation. Part II (experimental work). In *The Seventh Asia-Pacific Conference on Wind Engineering*, November 2009.

[48] R. I. McLachlan. Explicit lie-poisson integration and the euler equations. *Phys. Rev. Lett.*, 71:3043–3046, 1993.

[49] F.R. Menter and M. Kuntz. *The Aerodynamics of Heavy Vehicles: Trucks, Buses and Trains*, chapter Adaptation of eddy-viscosity turbulence models to unsteady separated flow behind

vehicles, pages 339–352. Lecture notes in applied and computational mechanics. Springer-Verlag, December 2004.

[50] R. Mittal, V. Seshadri, and H.S. Udaykumar. Flutter, tumble and vortex induced autorotation. *Theoretical and Computational Fluid Dynamics*, 17(3):165–170, 2004.

[51] S.A. Orszag. Analytical theories of turbulence. *Journal of Fluid Mechanics*, 41:363–386, 1970.

[52] U. Piomeli, W. Cabot, P. Moin, and S. Lee. Subgrid scale backscatter in turbulent and transitional flows. *Physics of Fluids A*, 3:1766–1771, July 1991.

[53] S. Reich. Momentum conserving symplectic integrators. *Physica D Nonlinear Phenomena*, 76(4):375–383, 1994.

[54] D. P. Riabouchinsky. Thirty years of theoretical and experimental research in fluid mechanics. *Journal of the Royal Aeronautical Society*, 39:282–348, 1935.

[55] S. Rimkus. A lab-scale experimental framework for studying the phenomenon of autorotation. Master's thesis, University of Central Florida, 2014.

[56] A. Scotti, C. Meneveau, and M Fatica. Dynamic Smagorinsky model on anisotropic grids. *Physics of Fluids*, 9(6):1856–1858, 1997.

[57] Y.-Q. Shen and G.-C. Zha. Comparison of high order schemes for large eddy simulation of circular cylinder flow. In *47th AIAA Aerospace Sciences Meeting and Exhibit*, January 2009.

[58] V. Shinde, T. Marcel, Y. Hoarau, T. Deloze, G. Harrah, F. Baj, J. Cardolaccia, J.P. Magnaud, E. Longatte, and M. Braza. Numerical simulation of the fluid-structure interaction in a tube array under cross flow at moderate and high Reynolds number. *Journal of Fluids and Structures*, 47:99–113, May 2014.

[59] M. Shur, P.R. Spalart, M. Strelets, and A. Travin. Detached-Eddy Simulation of an Airfoil at High Angle of Attack", 4th Int. Symp. Eng. Turb. Modelling and Measurements, Corsica. May 24-26, 1999.

[60] J. S. Smagorinsky. General circulation experiments with the primitive equation. *Monthly Weather Rev.*, 91:99–164, 1963.

[61] E. H. Smith. Autorotating wings: an experimental investigation. *Journal of Fluid Mechanics*, 50(3):513–534, 1971.

[62] P. R. Spalart and Langley Research Center. Young-person's guide to detached-eddy simulation grids. Technical report, National Aeronautics and Space Administration, Langley Research Center, NASA Center for Aerospace Information Hampton, Va.: Hanover, MD, 2001.

[63] P.R. Spalart and S.R. Allmaras. A one-equation turbulence model for aerodynamic flows. In *30th Aerospace Sciences Meeting and Exhibit*, 1992.

[64] P.R. Spalart, S. Deck, M.L. Shur, and K.D. Squires. A new version of detached-eddy simulation, resistant to ambiguous grid densities. *Theoretical and Computational Fluid Dynamics*, 20:181–195, 2006.

[65] P.R. Spalart, W.-H. Jou, M. Strelets, and S.R. Allmaras. Comments on the feasibility of LES for wings, and on a hybrid RANS/LES approach. Advances in DNS/LES, 1st AFOSR Int. Conf. on DNS/LES, Greyden Press, Columbus, H., Aug. 1997.

[66] P. Subbareddy and G. V. Candler. Numerical investigations of supersonic base flows using DES. In *43rd AIAA Aerospace Sciences Meeting and Exhibit*, pages 14497–14510, 2005.

[67] A.E. Tejada-Martinez and K.E. Jansen. A dynamic smagorinsky model with dynamic determination of the filter width ratio. Technical report, Rensselaer Polytechnic Institute, 2004.

[68] A. Travin, M. Shur, P. Spalart, and M. Strelets. Improvement of delayed detached-eddy simulation for LES with wall modelling. In *European Conference on Computational Fluid Dynamics*, 2006.

[69] A. Travin, M. Shur, M. Strelets, and P. Spalart. Detached-eddy simulations past a circular cylinder. *Flow Turbulence and Combustion*, 63:293–313, 1999.

[70] J. Tyacke, P. Tucker, R. Jefferson-Loveday, N. R. Vadlamani, R. Watson, I. Naqavi, and X. Yang. Large eddy simulation for turbines: Methodologies, cost and future outlooks. *Journal of Turbomachinery*, 136(6):061009, 2013.

[71] K. Varshney, S. Chang, and Z. J. Wang. The kinematics of falling maple seeds and the initial transition to a helical motion. *Nonlinearity*, 25:C1–C8, 2012.

[72] C.A. Velez, S. Martin, A. Jemcov, and S.S. Vasu. LES simulation of an enclosed turbulent reacting methane jet with the tabulated premixed CMC method. *Journal of Engineering for Gas Turbines and Power*, pages GTP–15–1357, 2016.

[73] A.K. Viswanathan, K.R. Klismith, J.R. Forsythe, and K. D. Squires. Detached-eddy simulation around a forebody at high angle of attack. In *41st Aerospace Sciences Meeting and Exhibit*, 2003.

[74] B.-Y. Wang and G.-C. Zha. Detached eddy simulations of a circular cylinder using a low diffusion E-CUSP and high-order WENO scheme. In *AIAA 38th Fluid Dynamics Conference*, June 2008.

[75] B.-Y. Wang and G.-C. Zha. Dettached eddy simulation of transonic airfoil limited cycle oscillation with high order WENO scheme. In *47th AIAA Aerospace Sciences Meeting and Exhibit*, January 2009.

[76] Baoyuan Wang. *Detached-eddy simulation of flow non-linearity of fluid-structural interactions using high order schemes and parallel computation*. PhD thesis, University of Miami, November 2008.

[77] R.A. Watson, P.G. Tucker, Z.N. Wang, and X. Yuan. Towards robust unstructured turbomachinery large eddy simulation. *Computers and Fluids*, 118:245–254, 2015.

[78] H. G. Weller, G. Tabor, H. Jasak, and C. Fureby. A tensorial approach to computational continuum mechanics using object-oriented techniques. *Computers in Physics*, 12(6):620–631, 1998.

[79] J.B. Wheatley. An aerodynamic analysis of the autogiro rotor with a comparison between calculated and experimental results. *National Advisory Committee for Aeronautics*, Report No. 487:235–249, 1934.